Universitat Politècnica de Catalunya

Ph.D. Programme

Automatic Control, Robotics and Computer Vision

Doctoral Thesis

Advanced Digital Resonant Control Techniques for Grid-Connected Voltage Source Converters

Marcos Orellana

Thesis advisor: Dr. Robert Griñó

December 2018

Advanced Digital Resonant Control Techniques for Grid-Connected Voltage Source Converters

Abstract

It is a fact that the presence of power distributed generation sources in the electrical sector is growing exponentially worldwide. This can mainly be explained by the increase of renewable energy production, which involves principally grid-connected single- and three-phase Voltage Source Converters (VSCs).

Regarding the regulations for medium and high power inverters, it is not enough to generate currents with low harmonic content and a unity-power-factor operation: grid-connected VSCs also have to work properly when the electrical grid presents non-ideal characteristics such as frequency variations, sags, swells or a high impedances, among other disturbances.

In line with the above and to improve the grid currents quality, LCL filters are widely used at the input of VSCs for their attenuation capabilities at high frequencies. However, they present a big resonance that may produce robustness issues. In order to study this problem and to stablish a basis for the controllers design, the grid-connected VSC mathematical models have been obtained, analysed and discretised, including passive and active LCL resonance damping techniques.

Adaptive Feedforward Cancellation (AFC) is the control technique addressed in this research work, leading to robust designs which are able to face all the grid disturbances aforementioned. AFC controllers, formed by resonators, have been considered in continuous- and discrete-time forms, and presenting infinite and finite gain, along with an anti-windup system for limitation purposes.

The development of an AFC control design method (directly in discrete time), and the use of automatic code generation tools, have allowed a fast implementation of the resonant controllers into a Digital Signal Processor (DSP). The experimental results obtained from the VSC prototypes (also developed during this thesis), prove the robustness of this control technique.

Técnicas avanzadas de control digital resonante para convertidores estáticos de potencia conectados a la red eléctrica

Resumen

Es un hecho que la presencia de fuentes de generación de energía distribuida en el sector eléctrico está creciendo exponencialmente a nivel mundial. Esto se debe esencialmente al incremento de la producción de energías renovables, que están estrechamente relacionadas con convertidores estáticos de potencia monofásicos y trifásicos (VSC) conectados a la red eléctrica.

Con respecto a la normativa en el ámbito de los inversores de media y alta potencia, ya no es solamente necesario que éstos generen unas corrientes con un bajo contenido en armónicos y un factor de potencia unitario: el funcionamiento de dichos equipos debe ser correcto frente a situaciones no ideales de la red como variaciones de frecuencia, huecos de tensión o redes débiles, entre otros.

En consonancia con lo anterior y para mejorar la calidad de las corrientes de red, los filtros LCL son ampliamente utilizados a la entrada de los VSC por su gran atenuación a altas frecuencias. Sin embargo, la gran resonancia que presentan puede generar problemas de robustez. Para estudiar este fenómeno y crear una base para el diseño de los controladores, se han obtenido, analizado y discretizado los modelos matemáticos de los VSC conectados a la red, incluyendo técnicas de amortiguación pasivas y activas para el filtro LCL.

La técnica de control abordada en este trabajo de investigación se denomina *Adaptive Feedforward Cancellation* (AFC), con la que se han conseguido diseños robustos y capaces de hacer frente a las perturbaciones en la red detalladas anteriormente. Los controladores AFC, formados por resonadores, han sido considerados en tiempo continuo y discreto, y con ganancias infinita y finita, junto con un sistema de limitación *anti-windup*.

El desarrollo de un método de diseño de control AFC (directamente en tiempo discreto) y el uso de herramientas de generación automática de código, han permitido una rápida implementación de los controladores resonantes en un procesador digital de señales (DSP). Los resultados experimentales obtenidos con los prototipos de convertidores monofásico y trifásico (también desarrollados durante esta tesis), confirman la robustez de esta técnica de control.

Techniques avancées de commande numérique résonante pour des convertisseurs de puissance connectés au réseau électrique

Résumé

C'est un fait que la présence de sources de génération d'énergie distribuée dans le secteur électrique est en train de croître exponentiellement à niveau mondiale. Ceci est principalement à cause de l'augmentation de la production d'énergies renouvelables, qui est étroitement liée à des convertisseurs statiques de puissance monophasés et triphasés (VSC) connectés au réseau électrique.

Par rapport aux régulations dans le domaine des onduleurs de moyenne et forte puissance, il n'est pas seulement nécessaire qu'ils génèrent des courants à bas contenu harmonique avec un facteur de puissance unitaire: le fonctionnement de ces systèmes doit être correct face à des situations non idéales du réseau comme variations de fréquence, creux de tension ou réseaux faibles, parmi d'autres.

Dans cet esprit et pour améliorer la qualité des courants du réseau, les filtres LCL sont vastement utilisés à l'entrée des VSC pour leur capacité d'atténuation aux hautes fréquences. Néanmoins, la grande résonance qu'ils présentent peut générer des problèmes de robustesse. Pour l'étude de ce phénomène et créer une base pour la conception des contrôlleurs, les modèles mathématiques des VSC ont été obtenus, analysés et discretisés, y compris techniques d'amortissement passives et actives pour le filtre LCL.

La technique de commande abordée dans ce travail de recherche s'appelle *Adaptive Feedforward Cancellation* (AFC), avec laquel il a été possible d'obtenir des contrôlleurs robustes et capables de faire face aux perturbations du réseau nommées précédemment. Les contrôlleurs AFC, constitués de résonateurs, ont été considerés en temps continu et discret, et avec des gains infinis et finis, ainsi qu'un système de limitation *anti-windup*.

Le développement d'une méthode de conception de commande AFC (directement en temps discret) et l'utilisation d'outils de génération de code automatique, ont permis une implementation rapide des contrôlleurs résonantes dans un processeur de signal numérique (DSP). Les résultats expérimentaux obtenus avec les prototypes des convertisseurs monophasé et triphasé (aussi développés pendant cette thèse), réaffirment la robustesse de cette technique de commande.

Tècniques avançades de control digital ressonant per a convertidors estàtics de potència connectats a la xarxa elèctrica

Resum

És un fet que la presència de fonts de generació d'energia distribuida al sector elèctric està creixent exponencialment a nivell mundial. Això es deu principalment a l'increment de la producció d'energíes renovables, directament vinculades a convertidors estàtics de potència monofàsics i trifàsics (VSC) connectats a la xarxa elèctrica.

Pel que fa a la normativa en l'àmbit dels inversors de mitjanes i altes potències, ja no és solament necessari que els convertidors generin corrents amb baix contingut harmònic amb un factor de potència unitari, sino que el funcionament d'aquests equips deu ser correcte enfront de situacions no ideals de la xarxa com ara variacions de freqüència, forats de tensió o xarxes febles, entre altres.

D'acord amb l'anterior, i per millorar la qualitat dels corrents de xarxa, els filtres LCL són àmpliament utilitzats a l'entrada dels VSC per la seva capacitat d'atenuació a altes freqüències. No obstant això, la gran resonància que presenten pot generar problemes de robustesa. Per estudiar aquest fenòmen i crear una base per al disseny dels controladors, s'han obtingut, analitzat i discretitzat els models matemàtics dels VSC connectats a la xarxa, incloent tècniques d'esmorteïment passives i actives per al filtre LCL.

La tècnica de control abordada en aquest treball de recerca es denomina *Adaptive Feedforward Cancellation* (AFC), amb la qual s'han aconseguit dissenys robustos i capaços de fer front a les pertorbacions de la xarxa detallades anteriorment. Els controladors AFC, formats per ressonadors, han sigut considerats en temps continu i discret, i amb ganàncies infinita i finita, juntament amb un sistema de limitació *anti-windup*.

El desenvolupament d'un mètode de disseny de control AFC (directament en temps discret) i l'ús d'eines de generació automàtica de codi, han permès una ràpida implementació dels controladors ressonants en un processador digital de senyals (DSP). Els resultats experimentals obtinguts amb els prototips de convertidors monofàsic it trifàsic (també desenvolupats durant aquesta tesi), confirmen la robustesa d'aquesta tècnica de control.

To my parents
À mes parents
A mis padres
Als meus pares

María Soledad Barceló Rodríguez,
Desiderio Orellana Martín.

Acknowledgement
Agradecimientos
Remerciements
Agraïments

This research work, which I am really proud of, would not have been possible without the valuable guidance and all the help received from my Ph.D advisor, Dr. Robert Griñó, and the Automatic Control Laboratory members from the Institute of Industrial and Control Engineering (IOC): Rafel Cardoner, Víctor Repecho and Enric Miró. Their patience with me has been infinite, exactly the same amount I am grateful to them. They own this PhD as much as I do. Also, my warmest thanks go to my family and friends who supported me in every decision I made. The list would be extremely long if I had to name them all.

Este trabajo de investigación, del que me siento muy orgulloso, no habría sido posible sin los valiosos consejos y toda la ayuda recibida por parte de mi director de tesis, el Dr. Robert Griñó y los miembros del Laboratorio de Control del Instituto de Organización y Control Insdutrial (IOC): Rafel Cardoner, Víctor Repecho y Enric Miró. Su paciencia conmigo ha sido infinita, exactamente la misma cantidad que les estoy agradecido. Este doctorado les pertenece tanto a ellos como a mí. También les doy las gracias de todo corazón a mi familia y amigos, que me han apoyado en todas las decisiones que he tomado. La lista sería extremadamente larga si tuviera

que nombrarlos a todos.

Ce travail de recherche, dont je me sens très fier, n'aurait pas été possible sans les précieux conseils et toute l'aide reçue de la part de mon directeur de thèse, le Dr. Robert Griñó et les membres du Laboratoire de Commande appartenant a l'Institut d'Ingénierie de Commande Insdutrielle (IOC): Rafel Cardoner, Víctor Repecho et Enric Miró. Sa patience avec moi a été infinie, exactement la même quantité dont je leur suis reconnaissant. Ce doctorat leur apparient tout autant que moi. Je remercie également de tout cœur ma famille et amis, qui m'ont soutenu dans toutes les decisions que j'ai prises. La liste serait extrêmement longue si je devais les nommer tous.

Aquest treball de recerca, del qual em sento molt orgullós, no hauria estat possible sense els valuosos consells i tota l'ajuda rebuda per part del meu director de tesi, el Dr. Robert Griñó i els membres del Laboratori de Control de l'Institut d'Organització i Control Insdutrial (IOC): Rafel Cardoner, Víctor Repecho i Enric Miró. La seva paciència amb mi ha estat infinita, exactament la mateixa quantitat que els estic agraït. Aquest doctorat els pertany a ells tant com a mi. També els dono les gràcies de tot cor a la meva família i amics, que m'han recolçat en totes les decisions que he pres. La llista seria extremadament llarga si els hagués de nomenar a tots.

Contents

List of Figures

List of Tables

"If we knew what it was we were doing, it would not be called research, would it?"

-Albert Einstein

1

Introduction and State of the Art

1.1 Introduction

Distributed power sources are becoming increasingly prevalent in the electrical sector. This is mostly due to the production growth of renewable energy based in wind turbines, photovoltaic systems, gas micro-turbines, small hydroelectric units, biomass processing units, etc. And these systems are usually connected to the electrical grid by means of static converters (Enslin, 2004, Blaabjerg et al., 2004). Also increasing in number, there are grid-connected systems for power rectification, like uninterrupted power supplies (UPS), battery chargers for industrial or electric vehicles, asynchronous motor drives or DC power supplies, which exactly as before, have a static converter at the input stage to keep the power factor (PF) as close as possible to the unity (Liserre et al., 2005).

The usual static converter topologies for these AC/DC applications are the single-phase Voltage Source Converter[1] (VSC) for low power levels and the three-phase three- or four-wire VSC for higher powers. Following the current power quality requirements when injecting power into the grid, it is desirable to control the active and reactive power for contributing to the electrical system regulation (E.ON, 2008, Ministerio de Industria de España, 2006, Ward, 2001). Also, line currents must have a reduced total harmonic distortion (THD). On the other hand, when the converters work as rectifiers, a unity-power-operation is desirable at the connection point to ensure the best utilisation of the electrical system. Regarding the converters input stage, it is remarkable how input filters studied in recent scientific works and used in commercial products are becoming increasingly more complex to improve the currents quality at high frequencies. For instance, filters like LCL are widely used as the link with the electrical grid instead of single L filters (Liserre et al., 2005, Teodorescu et al., 2011).

These converters have to face certain operation problems when they are connected to weak grids (Liserre et al., 2006, Enslin and Heskes, 2004, Bollen, 2000). Basically, these are: grid frequency variations, voltage harmonics, large grid impedance and/or value variation, unbalanced three-phase voltage signals, temporary transitory variation of the grid voltage levels (sags and swells) and random or repetitive variations of the voltage levels (ringings or flicker). All these non-ideal situations in the grid produce operation problems to the converters and to the grid itself, for example, instabilities or undesired resonances causing sub-synchronous oscillations. This is the reason why it is necessary to investigate more sophisticated control techniques able to operate the converters properly when there is an anomaly in the grid. It is important to highlight that from the control theory point of view, all these non-ideal situations can be expressed as parametric uncertainties and disturbances (usually periodic) in the model.

[1] These operate by converting the DC voltage (usually called bus) into an AC signal.

The use of Digital Signal Processors (DSP) in control systems of all kinds has been increasing due to their flexibility and continuously improving capabilities. Thus, discrete-time controllers for sampled-data control systems are usually conceived in continuous-time and then discretised to be implemented into a DSP; this procedure is widely used because it is straightforward and easy to perform (e.g. by applying the bilinear transform). Nevertheless, even if the plant is continuous-time, the controller can only handle discrete-time signals, so the design of a discrete-time controller for a continuous-time plant is not a continuous-time problem. Roughly speaking, the points which make the difference are:

- The controller sees a discrete-time version of the real plant, which has sampling zeroes, and some of them are usually non-minimum phase (Åström et al., 1984).
- The Nyquist rate states that the sampling period must be properly chosen to not miss the fastest dynamics to be controlled.
- In order to update the control signal, the controller needs time to sample the input signals, compute the algorithm and load the modulators. The total delay is usually one sampling period and its effect may be significant (Orellana and Griñó, 2012).
- Computations are not infinitely accurate (there may be quantisation), so controllers with poles over the unit circle (like resonators), must be properly implemented to avoid instability problems.
- A digital controller can perform operations that would be very difficult (or even impossible) to implement with a continuous-time (e.g. analogue) controller such as delays, matrix inversions or trigonometrical operations.

Thus, some controllers will not work if they are conceived in continuous time and then discretised to be implemented (Yepes et al., 2010). Nevertheless, the existence of more techniques to design continuous-time controllers makes this procedure widely used, and these may work well if the sampling period has been chosen properly and the controller is robust enough.

1.2 Background

There exist several suitable control techniques for the VSC control application. The most relevant are Repetitive Control, Adaptive Feed-forward Cancellation (AFC), Synchronous-Frame Controllers and Proportional-Resonant Control. All these techniques are based on the same principle, the Internal Model Principle (IMP) (Francis and Wonham, 1976), which states that the open-loop system must contain a model

of the references to be tracked and the disturbances to be rejected. The meaning of this affirmation will be explained more into detail in Chapter 3, but the main idea consists in giving infinite gain to the frequencies to be tracked or rejected.

Repetitive Controllers are able to track periodic signals and reject periodic disturbances (Costa-Castelló et al., 2005, Hillerström and Walgama, 1996, Kempf et al., 1993, Escobar et al., 2007, Wu et al., 2010). They are designed supposing that the frequency of the periodic signals present in the system is constant and that the sampling time for the controller algorithm is also chosen to be a constant value. Repetitive controllers in the power electronics domain have been used for inverters (Zhou and Wang, 2001), active filters (Costa et al., 2004, Griñó et al., 2007, Costa-Castelló et al., 2009), rectifiers (Zhou and Wang, 2003) and UPS systems (Escobar and Valdez, 2007, Rech et al., 2000). The main drawbacks of this technique are the difficulty to track frequency variations, and that high frequencies have to be treated carefully since they are naturally amplified by the controller, causing robustness or stability problems (Griñó et al., 2007).

The other control techniques: Adaptive Feed-forward Cancellation, Synchronous-Frame Controllers (Zmood, 2003, Yepes et al., 2014) and Proportional-Resonant Control (Teodorescu et al., 2006, Twining and Holmes, 2003) have different names, but they are very similar from a mathematical point of view: they are all particular cases of a second-order generalized integrator. Because of the controller structure, AFC will be the technique which will be emphasised in this thesis.

AFC was born as a linear time-varying (LTI) adaptive control technique. However, under certain conditions, it becomes a linear time-invariant (LTI) system. With AFC it is possible to selectively reject periodic disturbances in frequency (Bodson et al., 1992) and the resulting controller is equivalent to the use of the IMP for periodic disturbance rejection. The equivalences between the IMP and the AFC control are analysed in detail in (Messner and Bodson, 2007).

Many authors have contributed to analyse and improve the AFC control technique. For example, the importance of properly tuning the resonators parameters to guarantee the system stability in continuous time (Bodson et al., 1994), different considerations about the possible basic controller structure variations (Bayard, 2000) and also some applications for the AFC scheme have been analysed for mechanical systems where a specific frequency components are to be rejected (Bodson, 2005).

A systematic procedure to tune the resonators parameters from a loop-shaping perspective is given in (Byl et al., 2005) and the use of AFC controllers in systems where the disturbances frequencies are unknown has also been studied in (Bodson, 2005). This control technique has been applied mainly in mechanical applications,

but its use in power electronic systems (in the discrete-time domain) has also been carried out in (Malo and Griñó, 2007, Malo and Griñó, 2008).

1.3 Objectives

This research project seeks to contribute in the control systems theory area and also, in a particular power electronics application with a clear practical interest. Thus, the aim of this thesis is twofold.

The first main objective is to obtain theoretical results in the field of the digital resonant control techniques. These results are envisaged in two main areas:

- to obtain robust control algorithms in front of model uncertainty, and also in front of the fundamental frequency variations of the signals to be tracked or rejected,
- and to state a straightforward controller design methodology, clear enough to allow its industrial use.

The second objective is the implementation of these control techniques, with the obtained theoretical enhancements, to the particular problem of AC/DC and DC/AC power conversion with a non-ideal grid. Ideally, the designed controllers have to be relevant, again, by their complexity and their hardware implementation cost, to the industrial sector.

The experimental plants will be a power bidirectional single-phase and three-phase three-wire VSCs, with a voltage DC bus, in their two operational modes: active rectifier and inverter connected to the grid. A particular emphasis will be given to the validation of the controller operation facing several grid issues: fundamental frequency variations, non-sinusoidal voltages (with higher-order harmonics), unbalanced three-phase systems and unknown and time-variant network impedances (weak grids).

It is important to note that the dynamics of these plants are very fast, their measurement noise levels are high and the sensors have a limited bandwidth (by cost reasons). Furthermore, the sampling period is bounded by the maximum frequency to be controlled and the computation time of the control algorithm, defining the maximum theoretic controller bandwidth.

1.4 Outline of the Thesis

The layout of this thesis is as follows:

- This is Chapter 1, where the state of the art in control techniques applied to VSCs and the research work objectives are presented.

- Chapter 2 is devoted to the mathematical models of the single- and three-phase VSCs in continuous and discrete time. The perfect control and zero dynamics are found and the control limitations are analysed. Also, a study of the techniques dealing with the LCL input filter damping are addressed.
- In Chapter 3, the AFC control technique is presented. The structure of resonators are analysed in continuous and discrete time. A systematic procedure to design these controllers in discrete time is found and it is also applied to finite-gain resonators. Finally, a limitation system (with anti-windup) for the resonators output amplitude is presented.
- Chapter 4 describes the complete controller structure and how the design is carried out. Some simulations results are shown to validate the controller before the implementation in the real plants.
- Chapter 5 presents the built hardware and all the experimental results for both converters, the single-phase full bridge and the three-phase three-wire voltage source converter.
- In the Conclusions Chapter, all the contributions are summed up and a also, suggestions of some possible future lines of research are given based in the obtained results and experience.

"If your experiment needs statistics, you ought to have done a better experiment."

-Ernest Rutherford

2

Mathematical Models of the Power Converters

2.1 Introduction

Mathematical models are more or less accurate representations of our reality in the world of mathematics. It is an abstraction which allows to make predictions, calculate interactions or obtain measurable states. In control theory, finding a suitable model of a system is the necessary first step to know it better and, eventually, to design a controller.

Since the start of power electronics based on semiconductors (thanks to the invention of the transistor in the middle of the 20th century), it has become a discipline that has been growing in importance, to such an extent that power supplies are everywhere. Also, many people have been making efforts to find new power converter topologies, modelling them or designing suitable controllers, and abundant literature can be found on this particular domain.

Even if the mathematics behind the modelling of power converters are complicated, there exist powerful results which lead to models that can be used easily, even if they present some limitations. In the appendixes, the method used to find the mathematical models of the topologies addressed in this work is presented. These are well known techniques, which can be successfully applied to many other power converters as well.

As introduced earlier, it is important to remark that an LCL low-pass filter is used at the input of the VSCs as the link with the electrical grid. The reason that this filter is so widely used, is because it can attenuate the harmonics produced by the converter switching better than other simpler filters, improving the grid currents quality at higher frequencies.

2.2 Single-Phase Full-Bridge VSC

The electrical diagram of a full-bridge single-phase power converter is shown in Fig. 2.1, and the differential equation system describing its dynamics can be written as

$$\begin{aligned} L_2\frac{\mathrm{d}i_2(t)}{\mathrm{d}t} &= -v_C(t) - r_2 i_2(t) + v_g(t) \\ L_1\frac{\mathrm{d}i_1(t)}{\mathrm{d}t} &= v_C(t) - r_1 i_1(t) - v_{C_0}(t)u(t) \\ C\frac{\mathrm{d}v_C(t)}{\mathrm{d}t} &= i_2(t) - i_1(t) \\ C_0\frac{\mathrm{d}v_{C_0}(t)}{\mathrm{d}t} &= -\frac{v_{C_0}}{R_0} + i_1(t)u(t), \end{aligned} \tag{2.1}$$

where $i_2(t)$ denotes the grid current (filter input current), $v_C(t)$ is the filter capacitor voltage, $i_1(t)$ is the filter right-sided current, $u(t) \in [-1, 1]$ is the control signal[1] and $v_{C_0}(t)$ is the DC bus voltage (rectifier output voltage).

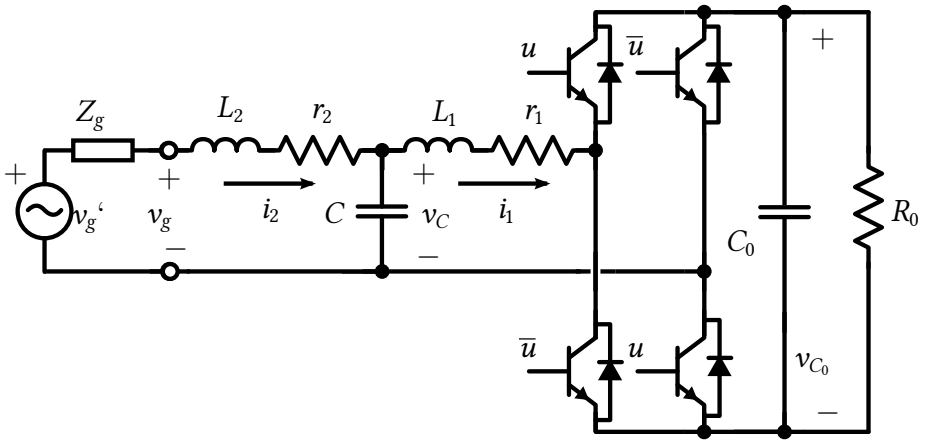

Figure 2.1: Electrical diagram of a full-bridge single-phase power rectifier with an LCL input filter.

Note that the measured grid voltage v_g depends on the grid impedance Z_g (that can be assumed as an inductance L_g in series with a resistor r_g), and the grid current $i_2(t)$ according to the equation

$$v_g(t) = v_g'(t) - Z_g i_2(t) = v_g'(t) - L_g \frac{\mathrm{d}}{\mathrm{dt}} i_2(t) - r_g i_2(t), \tag{2.2}$$

where $v_g'(t)$ denotes the generator voltage. This means that the measured grid voltage $v_g(t)$ will vary its phase and amplitude with respect to $v_g'(t)$ depending on the consumed current $i_2(t)$, introducing an uncontrolled loop into the system. The generator voltage $v_g'(t)$ is known but not accessible; it is the measured voltage $v_g(t)$, the one that will be used to carry out the control and all the power calculations.

2.2.1 Control Objectives

The controller is intended to attain these two control objectives:

- The first one is to keep the average value of the DC bus voltage $\overline{v_{C_0}}$ constant and equal to a reference value V_{C_0}.
- The second one is to generate a low THD sinusoidal line current, with the same frequency and phase as the grid voltage (for unity-power-factor operation), and with the necessary amplitude to fulfil the first objective.

[1]The control signal is discrete, $u(t) \in \{-1, 1\}$, but, when the system is averaged at the switching frequency, $u(t) \in [-1, 1]$.

In other words, the controller will determine the grid current amplitude that is necessary to keep the DC bus voltage average value constant. As it will be justified later, the first control objective refers to the average value since a constant DC bus voltage is not compatible with the second control objective.

Both control objectives should be carried out by using the minimum number of sensors (input voltages, input currents and DC bus voltage). Also, the controller must be robust enough to face usual grid disturbances like: unbalanced voltages, load or grid frequency variations, high grid impedances, harmonics, sags or swells, and ringings, among others.

2.2.2 Perfect Control and Zero Dynamics

The perfect control of a system is the one that lets perfectly reach the control objectives, and the remaining dynamics of the system is usually called the zero dynamics (or the exact dynamics). It is also necessary that in steady-state, the control signals are bounded, remaining inside its physical limits and that the zero dynamics is stable. In the case of the single-phase power converter, the input current must be sinusoidal (of amplitude I and frequency ω_g) and, for unity-power-factor operation, it must be in phase with respect to the input voltage (of amplitude V and frequency ω_g)

$$i_2(t) = I\sin(\omega_g t),\ v_g(t) = V\sin(\omega_g t). \tag{2.3}$$

Therefore, replacing the current $i_2(t)$ and the voltage $v_g(t)$ in the equation system (2.1) by the expressions in (2.3), the ideal control $u_p(t)$ and the zero dynamics can be computed[2] as a function of the system parameters. So, the ideal control is

$$u_p(t) = \frac{1}{v_{C_0}(t)}\left[V\left(1 - CL_1\omega_g^2\right)\sin(\omega_g t) + I\omega_g CL_1L_2\left(\omega_g^2 - \omega_n^2\right)\cos(\omega_g t)\right],$$

where $\omega_n = \sqrt{\frac{L_1+L_2}{CL_1L_2}}$ is the filter resonance frequency and the DC bus voltage $v_{C_0}(t)$ in steady state is

$$v_{C_0}^2(t) = \frac{1}{2}R_0IV + \sqrt{\frac{a^2+b^2}{\frac{1}{R^2}+\omega_g^2C^2}}\sin\left(2\omega_g t + \arctan\left[\frac{b-\omega_g CR_0 a}{a+\omega_g CR_0 b}\right]\right), \tag{2.4}$$

where[3] $a = IV(2C^2L_1L_2\omega_g^2(\omega_n^2 - \omega_g^2) - 1)$ and $b = \frac{1}{2}CL_1L_2\omega_g\left[(I^2\omega_g^2L_2 - \frac{V^2}{L_2})(\frac{1}{L_1} - C\omega_g^2) + I^2(2\omega_g^2 - \omega_n^2)\right]$.

[2]For the sake of simplicity, $r1$ and $r2$ have been neglected and the load has been supposed a resistance of value R.

[3]The zero dynamics is stable and, then, the exponential decaying terms are neglected on the steady-state equations.

From this expression, one can conclude that v_{C_0} is a function of the grid voltage V and current I amplitudes, and the load R_0 (the rest of parameters only have an effect on the oscillations amplitude). Therefore, in steady-state and under perfect control, $v_{C_0}(t)$ is a periodic signal of fundamental frequency $2\omega_g$ oscillating around the value

$$V_{C_0} = \sqrt{\frac{1}{2} R_0 I V}. \tag{2.5}$$

The same result is obtained when performing an input-output power balance by neglecting the DC bus oscillations. Note that the V_{C_0} is the RMS value of $v_{C_0}(t)$, and that the average value will always be smaller because of the square root, but this difference is negligible if the oscillations are small.

It is important to highlight that considering the DC bus voltage as a constant value V_{C_0}, the differential equation system (2.1) becomes linear. And as it will be seen in the present chapter, this fact makes easier the analysis and the controller design.

2.3 Three-Phase Three-Wire VSC

Fig. 2.2 shows the electrical schematic of a three-phase three-wire PWM rectifier with an LCL input filter.

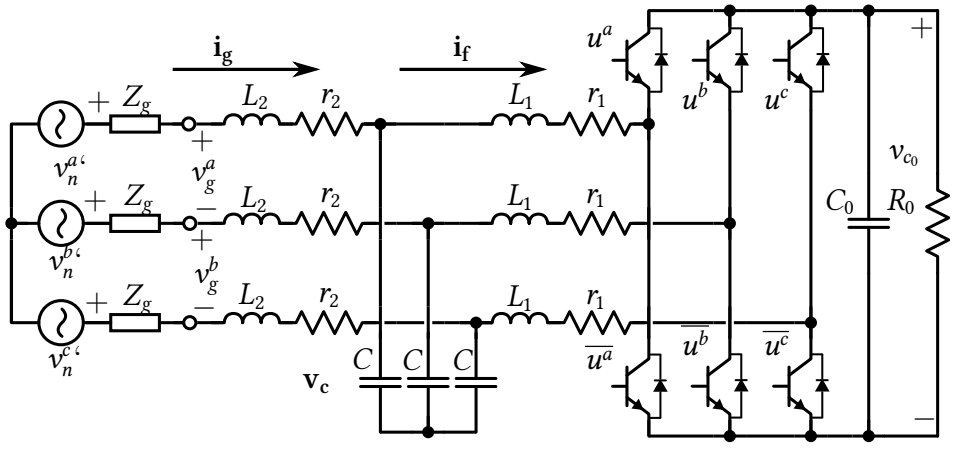

Figure 2.2: Electrical schematic of a three-phase three-wire power rectifier with an LCL input filter.

The non-linear differential equation system describing the converter dynamical

behaviour is

$$\begin{aligned} L_2\frac{d}{dt}\mathbf{i_g}(t) &= \mathbf{M}\mathbf{v_c}(t) - r_2\mathbf{i_g}(t) + \mathbf{N}\mathbf{v_g}(t) \\ L_1\frac{d}{dt}\mathbf{i_f}(t) &= -\mathbf{M}\mathbf{v_c}(t) - r_1\mathbf{i_f}(t) + \frac{1}{2}v_{c_0}(t)\mathbf{u_c}(t) \\ C\frac{d}{dt}\mathbf{v_c}(t) &= \mathbf{i_g}(t) - \mathbf{i_f}(t) \\ C_0\frac{d}{dt}v_{c_0}(t) &= -i_0 + \mathbf{i_f}(t)^{\mathrm{T}}\mathbf{u_c}(t), \end{aligned} \tag{2.6}$$

where[4] $\mathbf{i_g} = [i_g^a, i_g^b, i_g^c]^{\mathrm{T}}$ is the line-to-neutral currents vector (filter input currents), $\mathbf{v_c} = [v_c^a, v_c^b, v_c^c]^{\mathrm{T}}$ is the filter capacitors voltages vector, $\mathbf{v_g} = [v_g^a, v_g^b]$ is the measured line-to-line voltages vector, $\mathbf{i_f}[i_f^a, i_f^b, i_f^c]^{\mathrm{T}}$ is the filter right-sided currents vector[5], $\mathbf{u_c} = [u^a, u^b, u^c]^{\mathrm{T}}$ is the control signals vector (where each element must be in the interval[6] $[-1, 1]$), v_{c_0} is the DC bus voltage (rectifier output voltage), i_0 is the rectifier output current ($\frac{v_{c_0}}{R}$ from Fig. 2.2), $\mathbf{M} \in M_3(\mathbb{R})$ is a rank 2 matrix and $\mathbf{N} \in M_{3,2}(\mathbb{R})$ is the matrix that transforms the measured phase-to-phase voltages $\mathbf{v_g}$ to the phase-to-neutral voltages $\mathbf{v_n}$

$$\mathbf{M} = \frac{1}{3}\begin{bmatrix} -2 & 1 & 1 \\ 1 & -2 & 1 \\ 1 & 1 & -2 \end{bmatrix}, \quad \mathbf{N} = \frac{1}{3}\begin{bmatrix} 2 & 1 \\ -1 & 1 \\ -1 & -2 \end{bmatrix}. \tag{2.7}$$

The same appreciation with the grid impedance than in the single-phase converter takes place in this case. The only difference is that the expression which relates the generator phase-to-neutral voltages $\mathbf{v_n}'$ to the measured voltages $\mathbf{v_n} = \mathbf{N}\,\mathbf{v_g}$ is now

$$\mathbf{v_n} = \mathbf{v_n}' - Z_g\mathbf{i_g} = \mathbf{v_n}' + L_g\frac{d}{dt}\mathbf{i_g} + r_g\mathbf{i_g}, \tag{2.8}$$

where again, Z_g is the grid impedance (i.e. the addition of a resistance r_g and an inductance L_g in series per phase).

It can be shown that the differential equation system (2.6) is not linearly independent. The physical constraint that the sum of the grid currents must sum zero $\sum \mathbf{i_g} = 0$ is reflected in the rank 2 $\mathbf{M}$ matrix (2.7). This fact is more noticeable if a

[4] Time dependencies have been dropped for easier reading.

[5] $\mathbf{x}^{\mathrm{T}}$ means the transpose of $\mathbf{x}$.

[6] Even if control signals are discrete, they commute at high frequencies, so the use of the averaged model is justified for the controller design.

$0\alpha\beta$ transformation[7] is performed

$$\mathbf{T} = \sqrt{\frac{2}{3}} \begin{bmatrix} \frac{\sqrt{2}}{2} & \frac{\sqrt{2}}{2} & \frac{\sqrt{2}}{2} \\ 1 & -\frac{1}{2} & -\frac{1}{2} \\ 0 & \frac{\sqrt{3}}{2} & -\frac{\sqrt{3}}{2} \end{bmatrix}, \tag{2.9}$$

so that $\mathbf{i}_g^{0\alpha\beta} = \mathbf{T}\,\mathbf{i}_g$, $\mathbf{i}_f^{0\alpha\beta} = \mathbf{T}\,\mathbf{i}_f$, $\mathbf{v}_c^{0\alpha\beta} = \mathbf{T}\,\mathbf{v}_c$, $\mathbf{u}^{0\alpha\beta} = \mathbf{T}\,\mathbf{u}_c$ and $\mathbf{v}_g^{0\alpha\beta} = \mathbf{T}\,\mathbf{N}\,\mathbf{v}_g$.

After some matrix operations, the 0 component of each variable becomes null and the differential equation system can be written only in terms of the α and β components, reducing the system from 10 equations in (2.6) to only 7

$$\begin{aligned} L_2 \frac{d}{dt}\mathbf{i}_g^{\alpha\beta} &= -\mathbf{v}_c^{\alpha\beta} - r_2 \mathbf{i}_g^{\alpha\beta} + \mathbf{v}_g^{\alpha\beta} \\ L_1 \frac{d}{dt}\mathbf{i}_f^{\alpha\beta} &= \mathbf{v}_c^{\alpha\beta} - r_1 \mathbf{i}_f^{\alpha\beta} - \frac{1}{2} v_{c_0} \mathbf{u}^{\alpha\beta} \\ C \frac{d}{dt}\mathbf{v}_c^{\alpha\beta} &= \mathbf{i}_g^{\alpha\beta} - \mathbf{i}_f^{\alpha\beta} \\ C_0 \frac{d}{dt} v_{c_0} &= -i_0 + \mathbf{i}_f^{\alpha\beta\,\mathrm{T}} \mathbf{u}^{\alpha\beta}. \end{aligned} \tag{2.10}$$

This transformation is also interesting since it decouples currents and voltages ($\mathbf{i}_g^{\alpha\beta}$, $\mathbf{i}_f^{\alpha\beta}$, $\mathbf{v}_c^{\alpha\beta}$) with respect to the control signals $\mathbf{u}^{\alpha\beta}$, that is, α and β components are independent.

2.3.1 Control Objectives

Analogously to the single-phase case, the digital controller is intended to attain these control objectives:

- Grid currents must be sinusoidal as much as possible (low harmonic content) and with an arbitrary phase φ with respect to the phase-to-neutral voltages. Mathematically, if the voltages are $V\sin(\omega_g t + \theta)$, currents should be of the form $I\sin(\omega_g t + \theta + \varphi)$, where V and I are the phase-to-neutral voltages and line currents amplitudes, ω_g is the grid frequency, θ is the angle of the corresponding phase (0, $-\frac{2\pi}{3}$ or $\frac{2\pi}{3}$) and φ is the angle which will determine the power factor ($\varphi = 0$ for unity-power-factor operation).

- The average value of the DC bus voltage must be equal to a fixed reference value $\overline{v_{c_0}} = V_{c_0}$. As it will be justified later, and contrary to what happens in the single-phase VSC, this value is constant for a balanced grid.

[7] The applied transformation is the linear map defined by the $\mathbf{T}$ matrix (White and Woodson, 1959).

Like before, the controller will determine the necessary grid currents amplitude I to keep the desired constant DC bus voltage v_{c0} value, and the same remarks about using the minimum number of sensors and controller robustness apply.

2.3.2 Perfect Control and Zero Dynamics

In (2.6), considering a balanced three-phase voltages and forcing the control objectives presented in the previous section, one can obtain the zero dynamics for the DC bus voltage, yielding

$$v_{C_0} = V_{C_0} = \sqrt{\frac{3}{2} R_0 V I \cos\varphi}. \tag{2.11}$$

The DC bus voltage depends on the load R_0, the grid voltages and currents amplitudes V, I and the power factor value defined by φ. It can be concluded that the zero dynamics is stable and that the DC bus voltage will be constant in steady-state, if the grid voltages are balanced. Otherwise, the DC bus voltage will present oscillations as in the single-phase rectifier case.

Another important fact about this three-phase three-wire topology is that there are not any harmonics multiples of 3 since the currents must sum zero. The proof to this statement can be found hereafter.

Proof. It is a physical constraint that the three line currents i_a, i_b and i_c must sum 0. Supposing that they are three periodic signals, with the same harmonic content and with their phases at 0, $-\frac{2\pi}{3}$ and $\frac{2\pi}{3}$ respectively, this constraint can be written as a Fourier series like

$$\sum_{n=-\infty}^{\infty} C_n e^{in\omega t} + \sum_{n=-\infty}^{\infty} C_n e^{in\left(\omega t - \frac{2\pi}{3}\right)} + \sum_{n=-\infty}^{\infty} C_n e^{in\left(\omega t + \frac{2\pi}{3}\right)} = 0.$$

As it can be observed, the three sums limits are the same and, since the Fourier series decomposition is unique, one can write that

$$C_n e^{in\omega t}\left(1 + e^{-i\frac{2\pi}{3}n} + e^{i\frac{2\pi}{3}n}\right) = 0.$$

The roots of this equation for n are all the integers except the multiples of 3. This is easy to show since $1 + e^{-i\frac{2\pi}{3}n} + e^{i\frac{2\pi}{3}n}$ is zero for all the $n \in \mathbb{Z} \sim \mathrm{mod}(n,3) = 0$. Therefore, $\forall n \in \mathbb{Z} \mid \mathrm{mod}(n,3) = 0$, C_n must be null since $e^{in\omega t}$ is not null for $\forall t$. □

Examining again (2.6), it can be seen that under the assumption from (2.11) that $v_{C_0} = V_{C_0}$ in steady-state, the differential equation system becomes linear. Thus, it is

possible to obtain the continuous-time transfer functions, the perfect control or to compute the discrete-time system (which will be used to design the discrete-time controller).

Defining $G(s)$ as the transfer function between the control signals $u^{\alpha\beta}(s)$ and the line currents $i_g^{\alpha\beta}(s)$, and $Y(s)$ as the input admittance of the LCL filter, the perfect control $u_p^{\alpha\beta}$ can be written as

$$\mathbf{u_p^{\alpha\beta}} = G^{-1}(s)\left[\mathbf{i_g^{\alpha\beta}}(s) - Y(s)\mathbf{v_g^{\alpha\beta}}\right]. \tag{2.12}$$

2.4 VSC Control Limitations

Control signals in power converters are physically limited, they can be 0 or 1 (or any value in between if the average model is considered). As it will be shown, besides the control signal, the elements that limit the amount of active and reactive power in VSCs, are the LCL filter components and the DC bus voltage values. Moreover, the grid impedance plays an important role as well. In literature, it can be found some authors dealing with this subject as in (Chinchilla et al., 2006), but indirectly.

The single-phase full-bridge power converter is going to be considered to illustrate the analysis leading to the power limitations analytical expressions. However, this analysis can be analogously used with the three-phase power converter since, after some transformations, one arrives to the same linear expressions[8].

As mentioned earlier, the differential equation system in (2.1) becomes linear under the hypothesis that v_{C_0} is a constant value V_{C_0}. In fact, the new differential equation system corresponds to the circuit shown in Fig. 2.3.

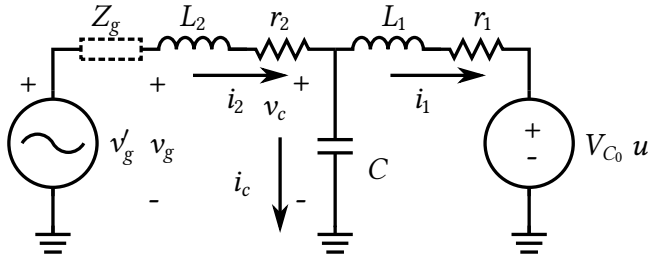

Figure 2.3: General circuit for a LCL filter with parasitic resistive elements, where v'_g is the grid voltage, V_{C_0} is the bus voltage and $u \in \{1, -1\}$ is the control signal coming from the VSC.

[8]The only differences are some constants due to the $\alpha\beta$ transformation

The LTI system corresponding to this electrical circuit can be written as

$$\begin{bmatrix} \frac{\mathrm{d}i_2(t)}{\mathrm{d}t} \\ \frac{\mathrm{d}i_1(t)}{\mathrm{d}t} \\ \frac{\mathrm{d}v_C(t)}{\mathrm{d}t} \end{bmatrix} = \begin{bmatrix} \frac{-r_2}{L_2} & 0 & \frac{-1}{L_2} \\ 0 & \frac{-r_1}{L_1} & \frac{1}{L_1} \\ \frac{1}{C} & \frac{-1}{C} & 0 \end{bmatrix} \cdot \begin{bmatrix} i_2(t) \\ i_1(t) \\ v_C(t) \end{bmatrix} + \begin{bmatrix} \frac{v_g(t)}{L_2} \\ \frac{V_{C_0}u(t)}{L_1} \\ 0 \end{bmatrix}, \tag{2.13}$$

so it is possible to compute the transfer function of $i_2(s)$ with respect to $u(s)$ and $v_g(s)$

$$i_2(s) = G(s)u(s) + Y(s)v_g(s) = \frac{1}{CL_1L_2}\frac{1}{d(s)}V_{C_0}u(s) + \frac{1}{CL_1L_2}\frac{CL_1s^2 + Cr_1s + 1}{d(s)}v_g(s), \tag{2.14}$$

where $d(s) = s^3 + \left(\frac{r_1}{L_1} + \frac{r_2}{L_2}\right)s^2 + \left(\omega_n^2 + \frac{r_1r_2}{L_1L_2}\right)s + \frac{r_1+r_2}{CL_1L_2}$ with $\omega_n = \sqrt{\frac{L_1+L_2}{CL_1L_2}}$. $G(s)$ is the transfer function between the control signal $u(s)$ and the line current $i_2(s)$ and $Y(s)$ is the transfer function between the grid voltage $v_g(s)$ and also $i_2(s)$, which can be seen as the input admittance of the LCL filter.

In order to study the system in the frequency domain, it is possible to perform the Fourier transform to the linear model. From the expression (2.14), the Laplace variable s can be replaced by $j\omega$, such that $i_2(j\omega) = G(j\omega)u(j\omega) + Y(j\omega)v_g(j\omega)$. Since the system only works at one frequency, ω can be replaced by ω_1 (the mains frequency), yielding to this complex expression

$$\mathbf{I}_2 = G'\mathbf{U} + Y'\mathbf{V_g}, \tag{2.15}$$

where G' and Y' are the transfer functions $G(s)$ and $Y(s)$ evaluated at $j\omega_1$: $G(j\omega_1)$ and $Y(j\omega_1)$ respectively. The variables $\mathbf{I}_2$, $\mathbf{U}$ and $\mathbf{V_g}$ can be seen as phasors, for instance, $\mathbf{U} = |\mathbf{U}|\,e^{j\angle\mathbf{U}} = |\mathbf{U}|\,\angle\mathbf{U}$.

2.4.1 Limitations without grid impedance

In this case, the grid impedance is null $Z_g = 0$, so $\mathbf{V'_g} = \mathbf{V_g}$. Therefore, fixing the angle of the grid voltage $\mathbf{V_g}$ to 0, it becomes simply the real value[9] V.

In order to establish the limitations in power, the conjugate of (2.15) may be multiplied by V, giving the apparent power $\mathbf{S} = \mathbf{V_g}\mathbf{I_2}^* = Pj + Q$ where P is the active power and Q is the reactive power. In this case $\mathbf{S} = V(G'\mathbf{U} + Y'V)^*$, that is

$$\mathbf{S} = V\mathbf{U}^*G'^* + V^2Y'^*. \tag{2.16}$$

Examining this expression closer, one can conclude that the power $\mathbf{S}$ will be the

[9] Working with RMS values.

image of the control signal $\mathbf{U}$ scaled by the constant VG'^* plus the offset $V^2Y'^*$. Since the magnitude of the control signal $\mathbf{U}$ can take any value between[9] 0 and $\frac{1}{\sqrt{2}}$ with any possible angle, the apparent power $\mathbf{S}$ is a circle of radius $\frac{|VG'^*|}{\sqrt{2}}$ centred at $V^2Y'^*$ as shown in Fig. 2.4.

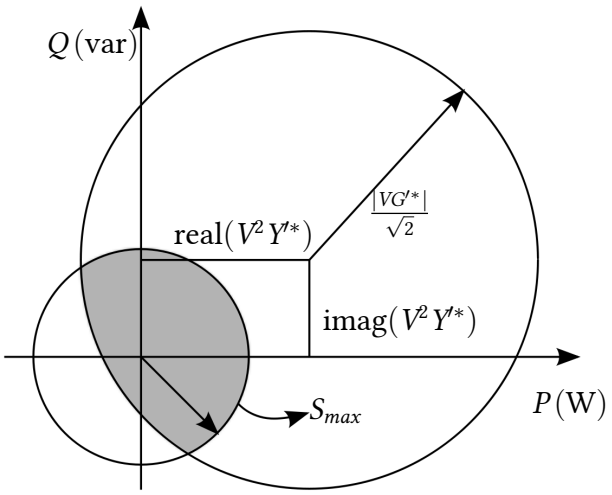

Figure 2.4: Diagram of the attainable powers in function of the signal control (the big circle represents $|\mathbf{U}| = \frac{1}{\sqrt{2}}$), grid voltage and the passive elements of the LCL input filter without grid impedance. The small circle represents the acceptable powers by the converter. The grey region represents the intersection between the both regions.

It is important to remark that the centre of this circle depends on the amplitude of the grid voltage V and the conjugate of the admittance of the input LCL filter Y'^*. Observe also that both the radius and the centre of this circle are proportional to V and V^2, respectively, so they will change if V varies.

On the other hand, fixing a maximum apparent power acceptable by the power converter $|\mathbf{S}| = S_{max}$ one obtains a circle centred at the origin of radius S_{max}. The intersection of both regions will determine the set of the possible converter operating points (Fig. 2.4 also shows this region).

2.4.2 Limitations with grid impedance

In this case, the generator voltage $v'_g(t)$ does not match any more the measured voltage $v_g(t)$; they are related by the equation (2.2), which, particularised again to the case of a only one working frequency by performing the Fourier Transform, one obtains

$$\begin{aligned} \mathbf{V_g} = \mathbf{V'_g} - Z_g\mathbf{I}_2 = \\ \mathbf{V'_g} - \left(j\omega_1 L_g + r_g\right)\mathbf{I}_2, \end{aligned} \tag{2.17}$$

where $\mathbf{V_g}$ and $\mathbf{V'_g}$ are the respective phasors of $v_g(s)$ and $v'_g(s)$ at the frequency $s = j\omega_1$. Now, combining this expression with (2.15), the new equation for the line current $\mathbf{I}_2$ can be written as

$$\mathbf{I}_2 = \frac{G'}{1 + Y'Z_g}\mathbf{U} + \frac{Y'}{1 + Y'Z_g}\mathbf{V'_g},$$

where G' and Y' are the same as in (2.15) and $\mathbf{V'_g}$ is now the real value V, since it is taken as the phase origin. Observe that this equation would be also valid in an operational sense (in the Laplace domain). In this case, the new transfer functions include a feedback (Y' is an admittance and Z_g is an impedance, so they are positive-real transfer functions and there will not be stability problems). Nevertheless, depending on the internal controllers, Y' could not be an admittance any more, and then it would not be a positive-real transfer function, so the stability could not be guaranteed.

In order to compute the apparent power $\mathbf{S}$, the conjugate of the former expression must be multiplied by the measured voltage, that is, $\mathbf{V_g}$, which is given in function of $\mathbf{V'_g}$ by the equation (2.17), so, the new apparent power S expression is

$$\mathbf{S} = \left(\mathbf{V'_g} - Z_g\mathbf{I}_2\right)\mathbf{I}_2{}^* = V\mathbf{I}_2{}^* - Z_g\left|\mathbf{I}_2\right|^2, \tag{2.18}$$

since $\mathbf{V'_g} = V$ and $\mathbf{I}_2\mathbf{I}_2{}^* = \left|\mathbf{I}_2\right|^2$.

Finally, replacing $\mathbf{I}_2$ and Z_g, one arrives to the expression

$$\begin{aligned}\mathbf{S} = {} & V\mathbf{U}^*G'^* + V^2Y'^* - \\ & \left(j\omega_1 L_g + r_g\right)\left|G'\mathbf{U} + Y'V\right|,\end{aligned} \tag{2.19}$$

where $G' = \frac{G'}{1+Y'Z_g}$ and $Y' = \frac{Y'}{1+Y'Z_g}$. Analysing this result, it can be deduced that the new expression is similar to the one obtained in (2.16) and they match each other when Z_g tends to 0. The centre of this new region corresponds to a control signal $|\mathbf{U}| = 0$ and it is placed at $V^2Y'^* - Z_g\left|Y'V\right|$.

On the other hand, the shape of the region when $|\mathbf{U}| > 0$ is not evident to obtain analytically: it becomes a circle if Z_g tends to zero and it seems an ellipse otherwise, but it is not an ellipse (the general equation of the curve for fixed $|\mathbf{U}| > 0$ is a four-degree polynomial). In Fig. 2.5, an example of the new working region is depicted (the maximum apparent power bearable by the power converter $|\mathbf{S}| = S_{max}$ is also depicted). Note that the point corresponding to $|\mathbf{U}| = 0$ is not placed at the geometrical centre of the closed curve.

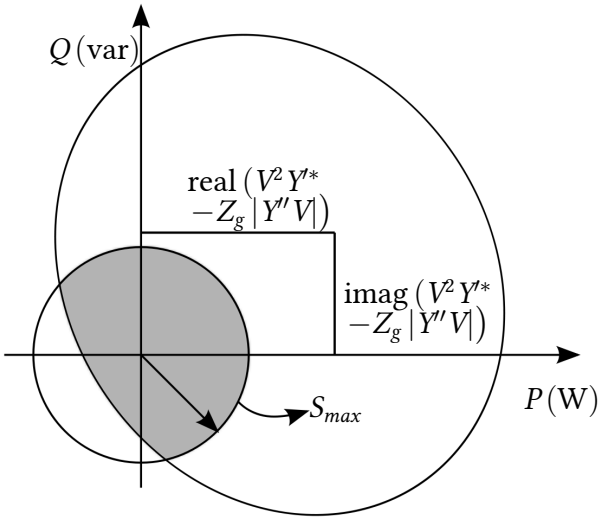

Figure 2.5: Diagram of the attainable powers in function of the signal control (the big closed curve represents $|\mathrm{U}| = \frac{1}{\sqrt{2}}$), grid voltage and the passive elements of the LCL input filter with grid impedance. The small circle represents the acceptable powers by the converter. The grey region depicts the intersection between the both regions.

2.4.3 Numerical Examples

For the sake of clarity, some numerical examples are going to be considered. Using the component values shown in Table 2.1, it is possible to compute $i_2(s)$ from (2.14)

$$i_2(s) = G(s)u(s) + Y(s)v_g(s) = \frac{-4.026 \cdot 10^{14}}{s^3 + 879.4s^2 + 7.287 \cdot 10^8 s + 4.482 \cdot 10^{11}}u(s) + \frac{5435s^2 + 4.328 \cdot 10^6 s + 1.006 \cdot 10^{12}}{s^3 + 879.4s^2 + 7.287 \cdot 10^8 s + 4.482 \cdot 10^{11}}v_g(s),$$

being G' and Y' the value of $G(s)$ and $Y(s)$ at $s = j\omega_1$, that is, $-433.207 + 672.661j$ and $-0.552 - 1.922j$, respectively.

Table 2.1: Example of Power Converter Parameter Values.

L_1	540 µH	r_1	0.43 Ω
L_2	184 µH	r_2	0.15 Ω
L_g	100 µH	r_g	0.1 Ω
C	10 µF	ω_1	50 Hz
V	230 V	V_{C_0}	400 V

The radius and the centre of the circle that limits the working region are computed from the expressions $\frac{|VG'^*|}{\sqrt{2}}$ and $V^2Y'^*$, that is, 130.12 kVA and $942.43 + 479.84j$ kVA

respectively. Fig. 2.6 depicts the working power region if the maximum power tolerated by the power converter is supposed to be $S_{max} = 20\,\text{kVA}$.

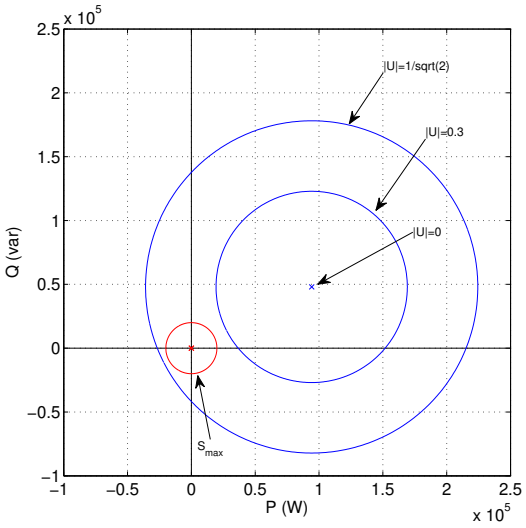

Figure 2.6: Working region when the DC bus voltage V_{C_0} is 400 V without grid impedance (intersection between the large blue circle and the red circle).

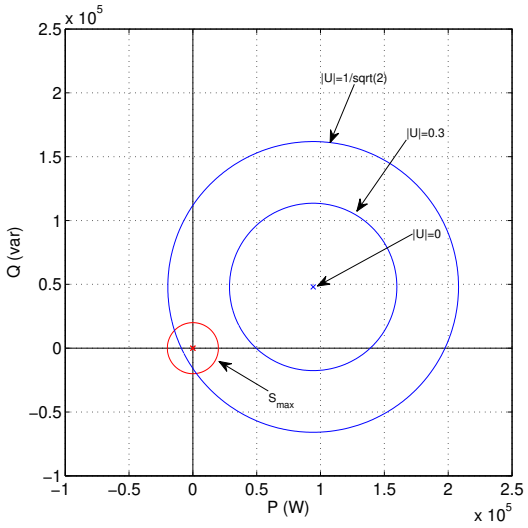

Figure 2.7: New working region when $V_{C_0} = 350\,\text{V}$ without grid impedance (intersection between the large blue circle and the red circle).

In this case, the magnitude of the control signal $|\mathbf{U}|$ does not limit the power through the converter, but the maximum acceptable power S_{max}.

Fig. 2.7 shows the new region if the DC bus voltage V_{C_0} value decreases in 50 V. Now, the blue circle does not contain any more the red one completely. The centre of the circle is the same as before, but the new radius is smaller. The intersection of both circles forms the set of attainable powers by the converter. Since the centre of the blue circle is placed in the first quadrant, the control signal will saturate before reaching some of the converter power limits.

The region with a DC bus voltage $V_{C_0} = 400\,\text{V}$ and a grid impedance is different from 0, $Z_g \neq 0$ is depicted in Fig. 2.8. The area defined by the blue curve is smaller than the equivalent without taking into account the grid impedance. This means that the total power able to flow through the converter is reduced. Observe also that these curves are not circles any more and that the power does not change linearly in function of the control signal magnitude $|\mathbf{U}|$.

Finally, Fig. 2.9 shows the new region if the DC bus voltage V_{C_0} value decreases in 50 V. As before, this affects the size of the working region, but the shape is the same. Also, observe that in this case, exactly as before, it would be impossible to reach some of the converter power limits.

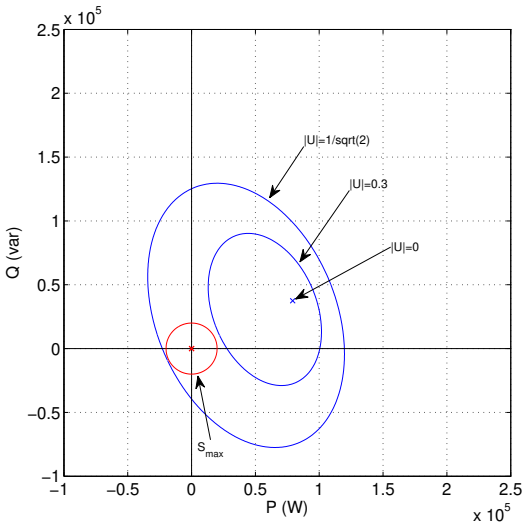

Figure 2.8: Working region when the DC bus voltage $V_{C_0} = 400,\mathrm{V}$ with grid impedance (intersection between the large blue curve and the red circle).

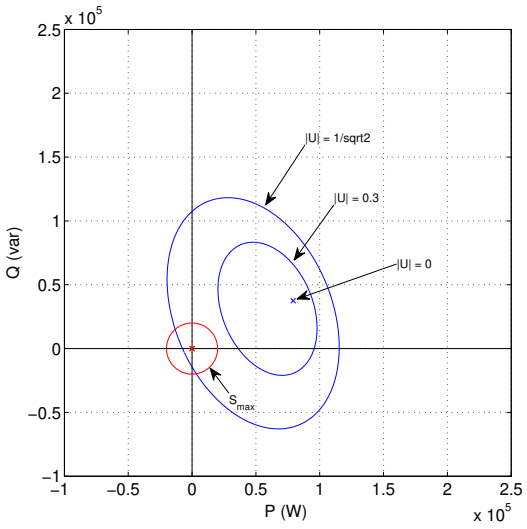

Figure 2.9: New working region when $V_{C_0} = 350,\mathrm{V}$ with grid impedance (intersection between the large blue curve and the red circle).

It is important to note that these results can be taken into account as a constraint when designing the LCL filter, or fixing the DC bus voltage value in steady-state.

2.5 Plants Discretisation in Time

Thus far, it has been shown that the control objectives can be fulfilled and that the zero dynamics is stable in both the single- and the three-phase VSCs. Moreover, the control limitations have also been analysed. All this information gives a good understanding of the converter, what is achievable and what is not.

Now, in order to design a digital controller able to fulfil the control objectives, instead of using the continuous-time plants to find a continuous-time controller (and discretise it for the implementation), the plants are going to be discretised first, and the controller will be designed directly in discrete-time.

This makes sense since the digital controller will see the discretized version of the plant. Moreover, as it will be shown, it is easier to take into account sampling effects in the discrete-time domain, saving one step since the controller will be directly digital. Hence, the exact discrete-time transfer functions can be obtained by performing

$$G(z) = \frac{1}{G_{zoh}(z)} \mathcal{Z}\left\{G_{zoh}(s)G(s)\right\}, \tag{2.20}$$

where $G(z)$ is the corresponding discrete-time version of the continuous-time trans-

fer function $G(s)$ and

$$\mathcal{Z}\{G(s)\} = \mathfrak{Z}\left\{\mathcal{L}^{-1}\{G(s)\}(t)\big|_{t=nT}\right\},$$

where $\mathcal{L}^{-1}\{.\}$ is the inverse Laplace transform, $\mathfrak{Z}\{.\}$ is the z-transform and T is the sampling period.

Observe that in the real system, the feedback signals pass through a zero-order hold (ZOH) representing the analogue-to-digital converters (ADCs). And the unit delay of one period representing the modulators loading, can directly be introduced as a pole at $z = 0$ into the plant, thus, giving $G_d(z) = \frac{1}{z}G(z)$, which is the transfer function that will be used for the controller design.

2.6 LCL Grid Interface Filter Damping

In order to reduce the high frequency harmonics produced by the converters switching nature, an LCL low-pass filter is connected between the mains and the converters. This kind of filters are able to attenuate high frequency spectral content in the input current (Freijedo et al., 2011). Nevertheless, the high amplification and the sudden phase loss produced at the filter resonance frequency ω_n constitutes its main downside and it is source of numerous stability issues (Teodorescu et al., 2011).

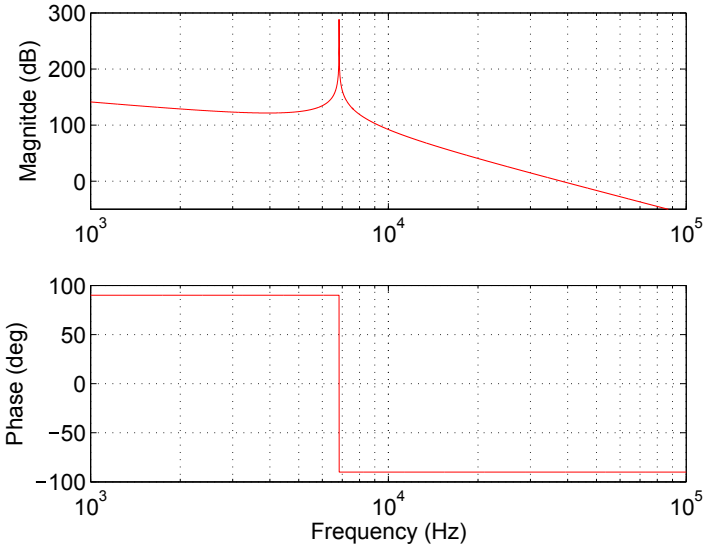

Figure 2.10: Bode diagram of the grid current with respect to the control signal for an LCL filter.

As an illustrative example, Fig. 2.10 shows the bode diagram of the grid current with respect to the control signal for some LCL filter values. Since it is a third order

filter, the slope at higher frequencies is $-60\,\mathrm{db/dec.}$, but it presents a high gain at the resonance frequency.

The most popular approaches to overcome this resonance issue are the passive and active damping techniques. The first one consists in adding passive dissipative elements and the second one consists in performing a feedback control loop from the filter capacitor current to change the closed-loop dynamics. In this section, both methods are presented and analysed, especially the active damping technique continuous and discrete time.

Nevertheless, as it will be shown in Chapter 4, a well designed controller can be robust enough and work perfectly without any damping technique, saving the losses from added components in the passive damping case, and saving sensors and the computation time of an extra control loop in the active damping one.

Fig. 2.11 shows the structure of an LCL filter with all the elements that will be considered in the next sections. Observe that this figure is different from Fig. 2.3 since it has a resistor r_c added in series to the filter capacitor. Hence, the Laplace domain of the input current $i_2(s)$ can be written as

$$i_2(s) = G_u(s)u(s) + G_{v_g}(s)v_g(s), \tag{2.21}$$

where $G_u(s) = n_u(s)/d(s) = -\frac{V_{C_0} r_c}{L_1 L_2}\left(s + \frac{1}{Cr_c}\right)/d(s)$ is the transfer function with respect to the control $u(s)$, $G_{v_g} = n_{v_g}(s)/d(s) = \frac{1}{L_2}\left(s^2 + \frac{r_1+r_c}{L_1}s + \frac{1}{L_1 C}\right)/d(s)$ is the transfer function with respect to the grid voltage $v_g(s)$ and $d(s) = s^3 + \left(\frac{r_1+r_c}{L_1} + \frac{r_2+r_c}{L_2}\right)s^2 + \left(\frac{L_1+L_2}{CL_1L_2} + \frac{r_1 r_2}{L_1 L_2} + r_c\frac{r_1+r_2}{L_1L_2}\right)s + \frac{r_1+r_2}{CL_1L_2}$ is the denominator polynomial. Note that $G_{v_g}(s)$ can be seen as the input admittance of the LCL filter.

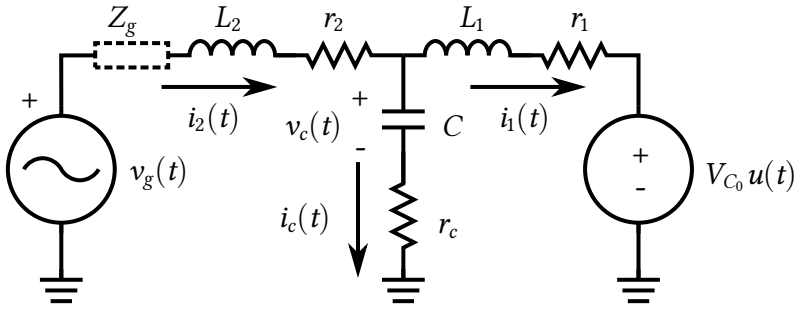

Figure 2.11: LCL filter schematic where $v_g(t)$ is the grid voltage, V_{C_0} is the bus voltage and $u(t) \in \{1, -1\}$ is the control signal coming from the VSC.

And a similar expression is obtained for the capacitor current $i_c(s)$

$$i_c(s) = H_u(s)u(s) + H_{v_g}(s)v_g(s), \tag{2.22}$$

where $H_u(s) = m_u(s)/d(s) = \frac{V_{C_0}}{L_1}\left(s^2 + \frac{r_2}{L_2}s\right)/d(s)$, $H_{v_g} = m_{v_g}(s)/d(s) = \frac{1}{L_2}\left(s^2 + \frac{r_1}{L_1}s\right)/d(s)$ and $d(s)$ is the same denominator as in (2.21).

2.6.1 Passive Damping

A first approach to limit the resonance peak consists in increasing the system damp by adding dissipative elements into the filter, traditionally a resistor r_C in series with the capacitor C (Wang et al., 2003). This method, called Passive Damping (PD), reduces considerably the undesired resonance oscillations, but also the filter performance at higher frequencies. Moreover, even if the stability is guaranteed for any resistance value, the energy dissipated by these elements increases the power losses in the converter (Routimo and Tuusa, 2007).

To understand how the PD works in a LCL filter, it is necessary to determine the role of r_1, r_2 and r_c. Therefore, neglecting all these resistances, the transfer function $G_u(s)|_{r_x=0}$, $x \in \{1, 2, c\}$ presents a relative degree of 3 (attenuation of $-60\,\text{dB/dec}$ at high frequencies) and an infinite resonance peak at $\omega_n = \sqrt{\frac{L_1+L_2}{CL_1L_2}}$

$$G_u(s)|_{r_x=0} = \frac{-\frac{V_{C_0}\omega_n^2}{L_1+L_2}}{s\left(s^2+\omega_n^2\right)}. \tag{2.23}$$

Note that the transfer function is marginally stable since the poles have zero real part, and they are simple. It is important to remark that ω_n can change if the grid impedance $Z_g(s) = r_g + L_g s$ varies, because the value of L_g is added to L_2. Fig. 2.12 shows the resonance frequency ω_n vs. $L_g + L_2$ graph varying from 10 µH to 1 mH for a filter with $L_1 = 550\,\mu\text{H}$ and $C = 720\,\mu\text{F}$.

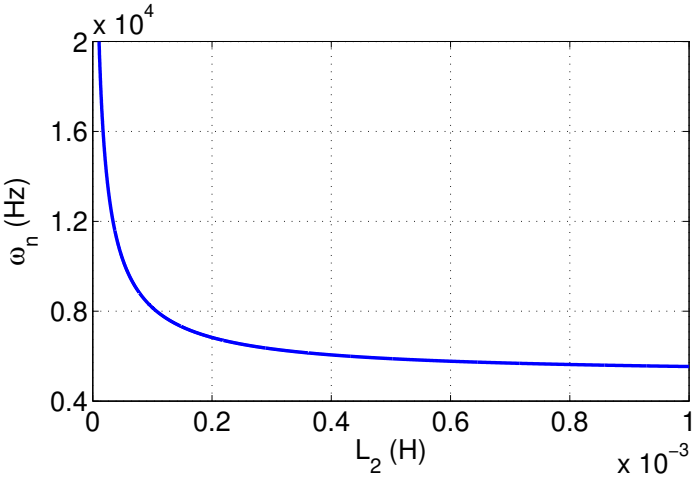

Figure 2.12: Values of the LCL filter resonance frequency ω_n depending on the inductance L_2 varying from 10 µH to 1 mH.

Considering $r_1 \neq 0$, $r_2 \neq 0$ and $r_C = 0$, the filter becomes stable and the relative degree of 3 is kept. Nevertheless, mostly all the input current flows through r_1 and r_2. Thus, it is not interesting to add dissipative elements at these positions since they will produce an important energy dissipation, reducing significantly the power transmission performance through the filter.

To study the case where $r_C \neq 0$, to simplify further calculations, r_1 and r_2 will be neglected in the following sections, even if the inductances have small parasitic resistances. This assumption will turn the transfer function marginally stable, but the conclusions obtained from the developments will not change qualitatively.

Therefore, the addition of a resistance in series with the capacitor ($r_c \neq 0$), gives the transfer function

$$G_u(s) = \frac{-\frac{V_{C_0}\omega_n^2}{L_1+L_2}(1 + Cr_c s)}{s\left(s^2 + Cr_c\omega_n^2 s + \omega_n^2\right)}. \tag{2.24}$$

It can be observed the appearance of a damping element proportional to r_c in the denominator. However, the relative degree is not 3 any more, but only 2 due to the appearance of a zero in the numerator, which means -40 dB/dec of attenuation at high frequencies. To highlight the PD behaviour, the bode diagrams for a typical filter with and without r_c are presented in Fig. 2.13. The parameters of the filter are $L_1 = 250\,\mu$H, $L_2 = 100\,\mu$H and $C = 300\,\mu$F.

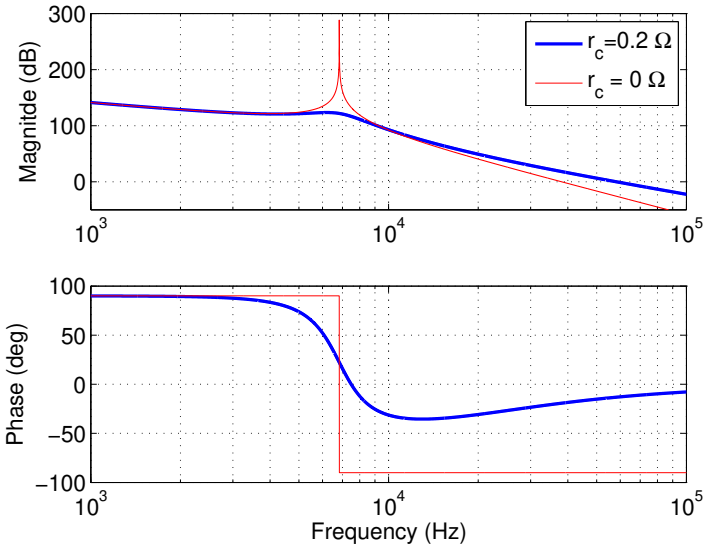

Figure 2.13: Bode diagrams for $G_u(s)$ with $\omega_n = 6.83$ kHz and $r_c = 0\,\Omega$ (red), $r_c = 0.2\,\Omega$ (blue).

The value of the resistance r_C does not affect significantly the resonance frequency of the filter. In other words, for a resistance $r_c > \frac{\sqrt{p}}{C\omega_n}$ the system will not present any more a resonance peak, where $p \approx 0.31712$ is the only positive real root of the polynomial $p^4 - 6p^3 + 3p^2 + 28p - 9 = 0$.

2.6.2 Continuous-Time Active Damping

Alternatively, Active Damping (AD) is a subtler approach: the addition of dissipative elements is not needed any more ($r_c = 0$) in favour of a feedback control loop. In short, the capacitor current $i_c(t)$ is measured and used to recalculate the control $u(t)$. Fig. 2.14 shows the AD control loop, where $K(s)$ is any causal controller of the form $\frac{b(s)}{a(s)}$. This way, the system dynamics is modified by increasing the damping, but keeping the filter properties at high frequencies. Many works presenting different AD implementations for power inverters can be found in literature; (Dahono, 2002, Teodorescu et al., 2003, Dannehl et al., 2010, Wu and Lehn, 2005) are some of them.

AD is the inner control loop in a power inverter, and if it is is not stable, higher level control loops may stabilise the system, but general performance will decrease since they will have to use a part of their control energy on this purpose. It will be shown that PD and continuous-time AD are always stable, but it is not the case for discrete-time AD: a proportional discrete-time AD loop may not be enough to guarantee the system stability (Wessels et al., 2008), and even more if grid impedance variations are considered. Consequently, high level controls will must be designed carefully to assure internal stability.

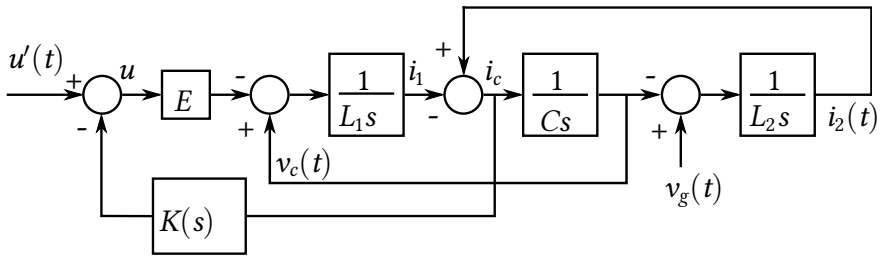

Figure 2.14: Filter block diagram with the general Active Damping feedback control loop.

The new closed loop equation for $i_2'(s)$ can be expressed as follows

$$i_2'(s) = G_u'(s)u'(s) + G_{v_g}'(s)v_g(s), \tag{2.25}$$

where $G_u'(s) = \frac{G_u}{H_uK+1}$ is the new transfer function with respect to the control $u'(s)$ and $G_{v_g}'(s) = \frac{G_{v_g}H_uK}{H_uK+1} + \frac{G_{v_g}}{H_uK+1} - \frac{G_uH_{v_g}K}{H_uK+1}$ is the new transfer function with respect to the grid voltage $v_g(s)$[10]. Observe that equation (2.25) has the same structure as equation (2.21).

In order to determine how the control signal $u'(s)$ affects the input current $i_2'(s)$,

[10]For the sake of clarity, dependencies on s have been dropped in transfer functions.

the transfer function $G'_u(s) = \frac{n_u(s)}{d_u(s)}$ can be rewritten as

$$G'_u(s) = \frac{n_u(s)a(s)}{a(s)d(s) + m_u(s)b(s)}. \tag{2.26}$$

The relative degree of this transfer function will always be 3 since $K(s)$ is causal and $\deg\{m_u(s)\} < \deg\{d(s)\}$, so the gain attenuation at high frequencies remains unchanged. The controller $K(s)$ contributes to change the dynamics of $G'_u(s)$; for instance, with a $K(s) = k_p$, the typical AD results in

$$G'_u(s) = \frac{-\frac{V_{C_0}\omega_n^2}{L_1+L_2}}{s\left(s^2 + \frac{k_p V_{C_0}}{L_1}s + \omega_n^2\right)}. \tag{2.27}$$

Like in (2.24), a dissipative term ($k_p V_{C_0}$) appears in the denominator. The dimension of this product is Ω and it is equivalent to a dissipative resistor, thus, the stability of the polynomial $s^2 + \frac{k_p V_{C_0}}{L_1}s + \omega_n^2$ is assured for every $k_p > 0$. Furthermore, a $k_p V_{C_0} > pL_1\omega_n$, where $p = \frac{1}{\sqrt{2}}(\sqrt{3} - 1) \approx 0.51763$, leads to a non-resonant gain. Observe that the value of k_p is related to the resistance value r_c in (2.24) by the expression $k_p = \frac{r_c}{V_{C_0}}\left(1 + \frac{L_1}{L_2}\right)$.

In Fig. 2.15, the bode diagram of $G'_u(s)$ is compared to the one achieved with the PD method $G_u(s)$. The filter parameters are the same as in Fig. 2.13 and the voltage bus $V_{C_0} = 300\,\text{V}$.

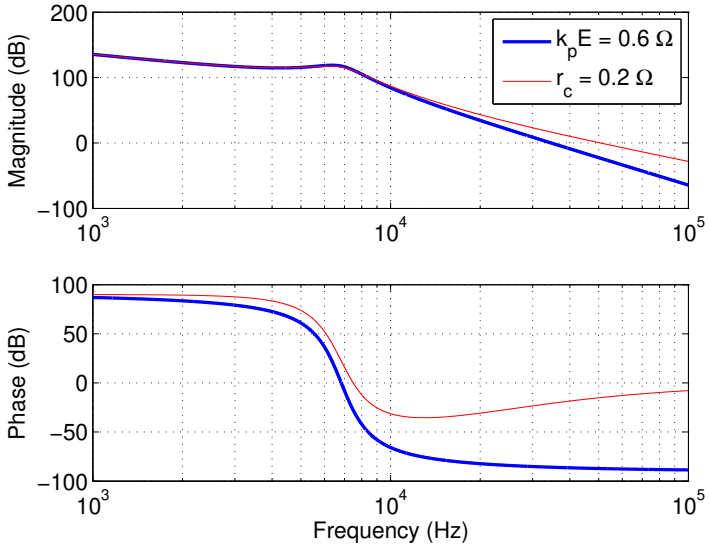

Figure 2.15: Bode diagrams for $G_u(s)$ with $r_c = 0.2\,\Omega$ (red) and for $G'_u(s)$ with $k_p = 0.002\,\text{A}^{-1}$ (blue). Both for $\omega_n = 6.83\,\text{kHz}$.

It is interesting to remark that both systems present the same behaviour at low frequencies, but they are different at higher frequencies (gain attenuation of -40dB/dec. for the PD vs. -60dB/dec. for the AD). Higher order controllers $K(s)$ would lead to more complex systems with a similar damping behaviour.

2.6.3 Discrete-Time Active Damping

When the AD control is implemented by means of a micro controller, the plant turns into a sampled-data control system. This fact has big implications on the final system operation, and even more if the unit delay of usual real discrete-time implementations is considered.

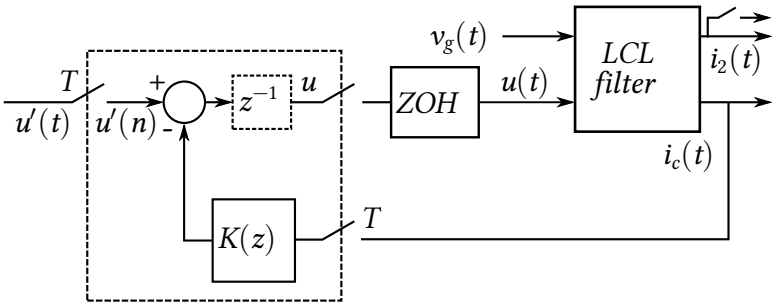

Figure 2.16: Sampled-data control system for the discrete-time Active Damping with sampling period T. The discrete-time controller is inside the dashed box.

The plant shown in Fig. 2.16 represents a discrete-time AD control over the LCL filter. The new expression for $i_2(z)$ can be written as

$$i_2'(z) = G_u'(z)u'(z) + G_{v_g}'(z), \tag{2.28}$$

where $G_u'(z) = \frac{(z^{-1})G_u}{(z^{-1})H_uK+1}$ is the new transfer function with respect to $u'(z)$ and $G_{v_g}'(z) = \frac{(z^{-1})G_{v_g}H_uK}{(z^{-1})H_uK+1} + \frac{G_{v_g}}{(z^{-1})H_uK+1} - \frac{(z^{-1})G_uH_{v_g}K}{(z^{-1})H_uK+1}$ the closed loop expression depending on $v_g(z)$. Note that dependencies on z have been dropped, the unit delay is shown in parentheses, and the sampling period is T.

The transfer functions $G_u(z)$ and $H_u(z)$ can be computed[11] from $G_u(s)$ and $H_u(s)$ as

$$G_u(z) = \mathcal{Z}\left\{G_{zoh}(s)G_u(s)\right\} = \frac{n_u(z)}{d(z)} \tag{2.29}$$

where the numerator is $n_u(z) = \frac{V_{C_0}(\sin(\omega_nT)-\omega_nT)z^2}{\omega_n(L_1+L_2)} + \frac{2V_{C_0}\omega_nT\cos(\omega_nT)z}{\omega_n(L_1+L_2)} - \frac{2V_{C_0}\sin(\omega_nT)z}{\omega_n(L_1+L_2)} +$

[11] $\mathcal{Z}\left\{G(s)\right\} = \mathfrak{Z}\left\{\mathcal{L}^{-1}\left\{G(s)\right\}(t)|_{t=nT}\right\}$.

$\frac{V_{C_0}(\sin(\omega_n T)-\omega_n T)}{\omega_n(L_1+L_2)}$, the denominator is $d(z) = (z-1)(z^2 - 2\cos(\omega_n T)z + 1)$, and

$$H_u(z) = \mathcal{Z}\{G_{zoh}(s)H_u(s)\} = \frac{m_u(z)}{d(z)} \tag{2.30}$$

where $m_u(z) = \frac{V_{C_0}\sin(\omega_n T)}{L_1\omega_n}(z-1)^2$ and $d(z)$ the same denominator as in (2.29).

Observe that the control action pass through a zero-order-hold (ZOH) with transfer function $G_{zoh}(s) = \frac{1-e^{-sT}}{s}$. The transfer functions $G_{v_g}(z)$ and $H_{v_g}(z)$ are obtained from $\mathcal{Z}\left\{G_{v_g}(s)v_g(s)\right\}$ and $\mathcal{Z}\left\{H_{v_g}(s)v_g(s)\right\}$ respectively, so the voltage grid $v_g(t)$ is embedded in their expression.

2.6.3.1 Discrete-Time AD without the Unit Delay

Neglecting the unit delay and using a constant controller $K(z) = k_p$, the denominator of $G_u'(z) = \frac{G_u}{H_u K+1} = \frac{n_1(z)}{d_1(z)}$ can be calculated as

$$d_1(z) = (z-1)(z^2 + \left(\frac{k_p V_{C_0}}{L_1\omega_n}\sin(\omega_n T) - 2\cos(\omega_n T)\right)z + 1 - \frac{k_p V_{C_0}}{L_1\omega_n}\sin(\omega_n T)). \tag{2.31}$$

The pole at $z = 1$ plays the same role as the pole at $s = 0$ in equations (2.23) and (2.27). The stability condition for k_p in order to assure that the other two poles are inside the unit circle can be found thanks to the Jury's criterion and it is[12]

$$0 < k_p < \frac{L_1\omega_n}{V_{C_0}\sin(\omega_n T)}(1+\cos(\omega_n T)) \tag{2.32}$$

Observe that the product $\omega_n T$ has big implications on the system stability. The sampling period T is usually fixed, but ω_n can present variations because of the grid impedance Z_g as explained in the previous section.

The graphical representation of the stability condition in (2.32) for a LCL filter with $\omega_n = 6.83\,\text{kHz}$ when varying ω_n from 0 to $\frac{\pi}{T}$, leads to the region depicted in Fig. 2.17. The only varying parameter in the product $\omega_n T$ is ω_n. A varying sample period T would lead to a different stability limits for k_p.

Note that the range of values of k_p that stabilise the quadratic factor in (2.31) reduces when ω_n increases until the range is null for $\omega_n T = \pi$. As shown in Fig. 2.12, an increase of the grid inductance L_g means a decrease of ω_n, what is favourable for the stability.

Continuous-time and discrete-time AD control behave different, so it is not easy

[12]The stability conditions have been calculated for a $\omega_n \in [0, \frac{\pi}{T}]$ in order to satisfy the sampling theorem ($\omega_n T \leq \pi$). Thus, $\omega_n = \frac{\pi}{T}$ is the maximum discrete-time frequency.

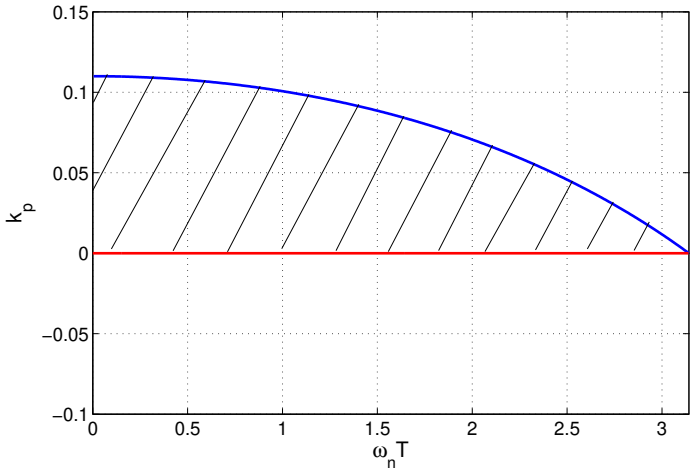

Figure 2.17: Stability region for the k_p parameter in function of the $\omega_n T$ angle for a LCL filter with $\omega_n = 6.83\,\text{kHz}$, $T = 50\,\mu\text{s}$ and without the unit delay. The region is delimited by the blue and red curves.

to give a physical interpretation of the value k_p. When varying this parameter, as it is shown in Fig. 2.18, poles of (2.31) move over the circle of constant radius $\sqrt{2(1-\cos(\omega_n T))}$ centred in $(1, 0)$, until they become real.

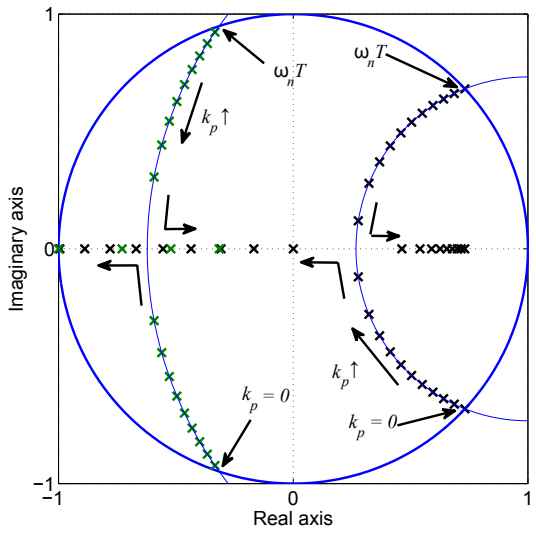

Figure 2.18: Root locus in function of the parameter k_p for $\omega_n T = \frac{\pi}{4}$ (black) and for $\omega_n T = \frac{5\pi}{9}$ (green).

Fig. 2.19 shows the comparison between the bode diagrams of the discrete-time transfer functions $G_u(z)$ and $G'_u(z)$. Both for the same parameters used in Fig. 2.15.

It can be seen that the discrete-time AD reduces the resonance peak and keeps the original attenuation of -60dB/dec. at high frequencies.

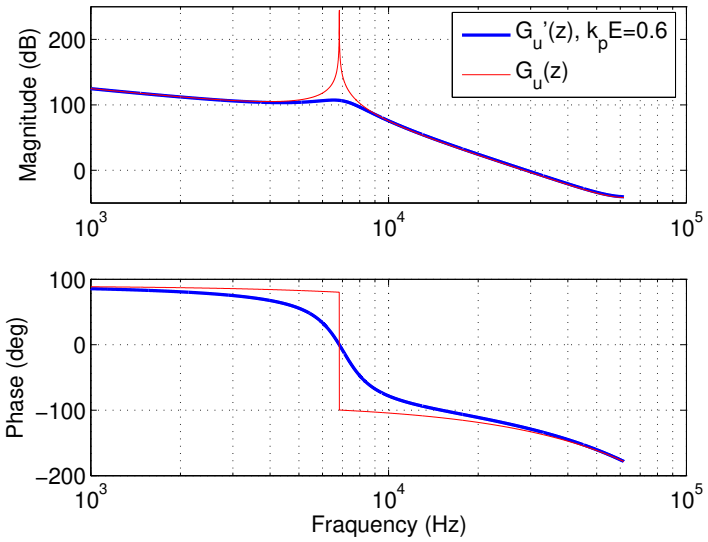

Figure 2.19: Bode diagrams of $G_u(z)$ and $G'_u(z)$ transfer functions for $\omega_n = 6.83\,\text{kHz}$ and $k_p V_{C_0} = 0.6$ for the second one.

2.6.3.2 Discrete-Time AD with the Unit Delay

The same procedure carried out in the previous subsection, but including the unit delay gives a new denominator for $G'_u(z) = \frac{z^{-1}G_u}{z^{-1}H_uK+1} = \frac{n_2(z)}{d_2(z)}$, yielding

$$d_2(z) = (z-1)(z^3 - 2\cos(\omega_n T)z^2 + \left(1 + \frac{k_p V_{C_0}}{L_1\omega_n}\sin(\omega_n T)\right)z - \frac{k_p V_{C_0}}{L_1\omega_n}\sin(\omega_n T)).$$

Applying again the Jury's criterion to the third degree polynomial, the new stability conditions are

$$\begin{aligned}
&\text{if} \quad 0 < \omega_n T < \frac{\pi}{3}, \quad 0 < k_p < \frac{L_1\omega_n}{V_{C_0}\sin(\omega_n T)}(2\cos(\omega_n T) - 1),\\
&\text{if} \quad \frac{\pi}{3} < \omega_n T < \frac{\pi}{2}, \quad \frac{L_1\omega_n}{V_{C_0}\sin(\omega_n T)}(2\cos(\omega_n T) - 1) < k_p < 0,\\
&\text{if} \quad \frac{\pi}{2} < \omega_n T < \pi, \quad -\frac{L_1\omega_n}{V_{C_0}\sin(\omega_n T)}(1 + \cos(\omega_n T)) < k_p < 0.
\end{aligned} \tag{2.33}$$

Fig. 2.20 contains the graphical representation of these stability conditions for k_p when varying ω_n from 0 to $\frac{\pi}{T}$.

Taking into account the unit delay, the stability conditions are completely different with respect to the previous case. Now, there are two points with a null stability region for k_p: the first one at $\omega_n T = \frac{\pi}{3}$ and second one at $\omega_n T = \pi$. Moreover, the sign of the stability range of k_p changes at $\omega_n T = \frac{\pi}{3}$. Therefore, it is not possible to

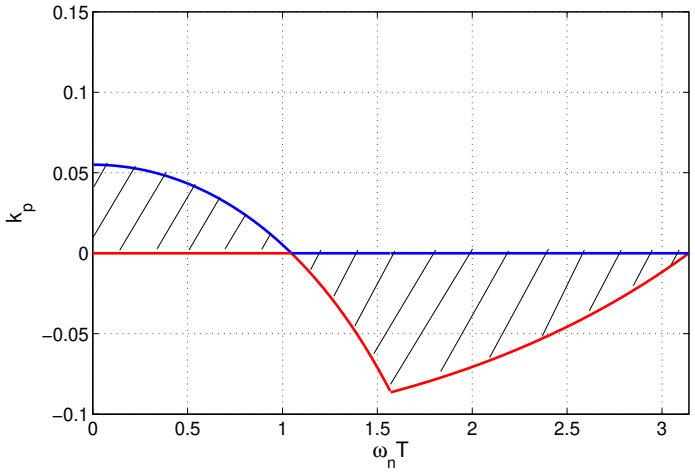

Figure 2.20: Stability region for the k_p parameter in function of the $\omega_n T$ angle for a LCL filter with $\omega_n = 6.83\,\text{kHz}$, $T = 50\,\mu\text{s}$ and with the unit delay taken into account. Upper limit appears in blue and lower limit in red.

find a constant k_p able to stabilise a discrete-time AD for any $\omega_n T$ angle. A more complex $K(z)$ controller (like a low-pass filter) could lead to better stability limits.

It is not clear how to obtain an analytic expression of the root locus in function of k_p from (2.33). Fig. 2.21 contains the root locus for $\omega_n T = \frac{\pi}{6}$, $\omega_n T = \frac{\pi}{2}$ and $\omega_n T = \frac{3\pi}{4}$, and Fig. 2.22 shows the comparison between the bode diagrams of the discrete-time transfer functions $G'_u(z)$ with and without the unit delay, both for the same filter parameters shown in Fig. 2.19.

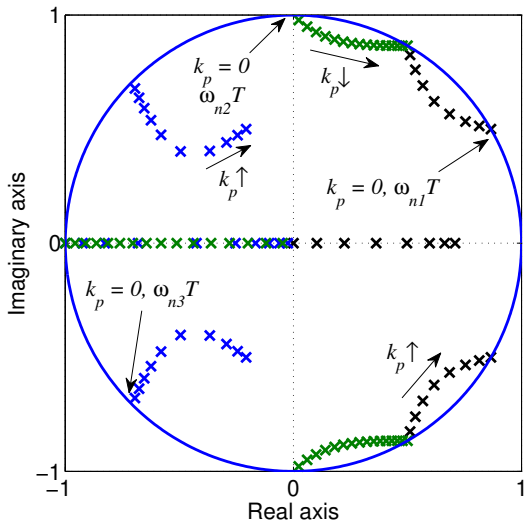

Figure 2.21: Root locus in function of the parameter k_p for $\omega_n T = \frac{\pi}{6}$ (black), $\omega_n T = \frac{\pi}{2}$ (green) and $\omega_n T = \frac{3\pi}{4}$ (blue).

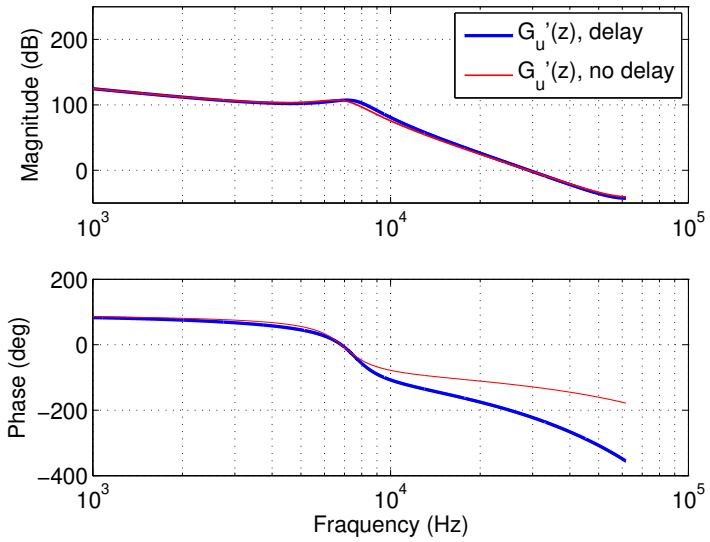

Figure 2.22: Bode diagrams of $G'_u(z)$ transfer functions with and without the unit delay for $\omega_n = 6.83\,\text{kHz}$ and $k_p = 0.002$.

Both bode diagrams are almost the same, but the resonance peak is higher when the unit delay is considered for the same value of k_p. Also, the phase loss is greater when taking into account the unit delay.

2.6.3.3 Implications for Higher Level Controls

To avoid internal instability in a control system, $\overline{\mathcal{U}}$-poles[13] and/or NMP-zeros of the plant must be treated carefully. In the previous section, it has been determined how to choose the parameter k_p in order to have a closed-loop transfer function $G'_u(z)$ with a stable denominator $d_2(z)$, but the numerator $n_2(z)$ is also important

$$\begin{aligned} n_2(z) = \frac{V_{C_0}}{\omega_n(L_1+L_2)}((\sin(\omega_n T) - \omega_n T)z^2 + \\ 2(\omega_n T\cos(\omega_n T) - \sin(\omega_n T))z + \\ \sin(\omega_n T) - \omega_n T). \end{aligned}$$

The kind of zeros of this second degree polynomial can be established by using again the Jury's criterion

$$\frac{\sin(\omega_n T)}{\omega_n T} > 1, \quad \cos(\omega_n T) > 1 \quad \text{and} \quad 2\frac{\sin(\omega_n T)}{\omega_n T} > 1 + \cos(\omega_n T).$$

[13] $\mathcal{U} = \{Z \in \mathbb{C} \text{ such that } |Z| < 1\}$ and $\overline{\mathcal{U}} = \mathbb{C} \setminus \mathcal{U}$. $\overline{\mathcal{U}}$-poles include unstable and marginally stable poles. $\overline{\mathcal{U}}$-zeros are usually called non minimum-phase zeros (NMP-zeros).

The two first conditions are never fulfilled, so one can conclude that for every ω_n and every T, one (or both) zeros will be over or out the unit circle. Fig. 2.23 shows the position of the zeros for a ω_n varying from 0 to $\frac{\pi}{T}$.

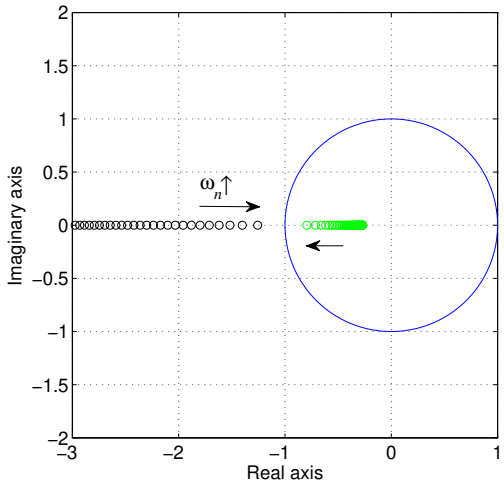

Figure 2.23: $G'_u(z)$ zeros in function of the LCL filter resonance frequency ω_n varying from 0 to $\frac{\pi}{T}$.

For this reason, in order to have a good performance, higher level controllers (like the main current control loop) must be carefully designed to deal with these NMP-zeros, since they cannot be cancelled.

"An expert is a person who has made all the mistakes that can be made in a very narrow field."

-Niels Bohr

3

Adaptive Feed-forward Cancellation Control Technique

3.1 Introduction

For the asymptotically output tracking and disturbances rejection, the Internal Model Principle (IMP) establishes that the open-loop transfer function of a system must contain a model of the references to be tracked and the disturbances to be rejected (Francis and Wonham, 1976). Referring to periodic signals, the corollary of this principle states that this is equivalent to have an open-loop transfer function which presents an infinity gain at the main frequency of the tracking/perturbation signal and its harmonics.

Linear controllers like the proportional-integral (PI) have infinite gain at zero frequency. This is suitable for regulation, but not good enough to face periodic disturbances. On the contrary, linear techniques as Repetitive Control, Proportional-Resonant Control or Adaptive Feed-forward Cancellation can give infinite gain at different frequencies, and have been proved to work very well in many different domains like mechanical or electrical (Manayathara et al., 1996, Lee, 1997) or electrical (Griñó et al., 2007).

The interest of AFC with respect to the other techniques is its flexibility. A repetitive controller (RC) cannot directly follow frequency changes in signals, which may cause big control action losses. Whereas, a resonator can be constantly tuned to the appropriate frequency by means of the carriers supplied by, for example, a phase-locked loop (PLL). Another AFC technique advantage with respect to RC is that high frequencies are not naturally amplified, since one can choose the number and the position of resonators in the control loop. Furthermore, each resonator has a zero that can be tuned to increase the robustness of the system, which is not directly possible with proportional resonant controllers.

On the other hand, there are more and more applications involving discrete-time controllers, due to the rapid technological advances on Digital Signal Processors (DSP). Digital controllers have many advantages that analogue ones do not have (memory, mathematical calculations, adaptability, etc.). Nevertheless, the use of a DSP to implement the controllers transforms the plant into a sampled-data control system, which also has some disadvantages (computational delays, time discretisation, etc.). As introduced earlier, it is possible to take these effects into account, if the whole controller design is carried out directly in discrete time.

Discrete-time resonators must have the same properties than the continuous-time ones, e.g., infinite gain at the exact frequency. However, an approximate discretisation process can create issues to the control system (Yepes et al., 2010). Note that resonators poles position is crucial: they must be precisely on the unit circle to give infinite gain and they must be at the right frequency or the controller will lose its properties.

Regarding the resonant controller design, each resonator adds two poles and one zero to the control-loop, so with few resonators the system increases its order rapidly. In literature, many guidelines to carry out a continuous-time AFC controllers design can be found (Bodson et al., 1994, Byl et al., 2005), and some works have been published concerning discrete-time resonators as well (Malo and Griñó, 2008, Yepes et al., 2011a,b, Yang et al., 2013), but there are still questions about the design which need a wider discussion.

3.2 Continuous- and Discrete-Time Resonator

Fig. 3.1 shows the block diagram of a continuous-time resonator. In spite of the origin of AFC control as an adaptive technique, it has been shown (Messner and Bodson, 2007) that, assuming the frequency ω_k as a constant value, a resonator is equivalent to the LTI system

$$R_k(s) = g_k \frac{s\cos(\varphi_k) + \omega_k \sin(\varphi_k)}{s^2 + \omega_k^2}. \tag{3.1}$$

where g_k, φ_k and ω_k are, respectively, the gain, the angle and the frequency of the k^{th} resonator.

Some authors work with discrete-time resonators by discretising the transfer function (3.1). As aforementioned, any approximation during the discretisation process can lead to undesired dynamical behaviours. Consequently, only an exact transformation is valid for the discrete-time resonator, that is, the impulse invariance[1],

$$R_k(z) = \mathcal{Z}\{R_k(s)\}, \tag{3.2}$$

where $R_k(z)$ is the corresponding discrete-time version of the continuous-time resonator $R_k(s)$.

It can be shown that this result is a particular case of the discrete-time resonator diagram depicted in Fig. 3.2.

Using the z-transform properties, the system can be expressed as a LTI system (Malo and Griñó, 2008)

$$R_k(z) = \frac{1}{2} g_k \left[H(z\mathrm{e}^{-j\omega_k T})\mathrm{e}^{-j\varphi_k} + H(z\mathrm{e}^{j\omega_k T})\mathrm{e}^{j\varphi_k} \right], \tag{3.3}$$

where $H(z) = \frac{H_n(z)}{H_d(z)}$ denotes any discrete-time transfer function. Hereunder there is the proof leading to this expression.

[1] $\mathcal{Z}\{G(s)\} = \mathfrak{Z}\left\{\mathcal{L}^{-1}\{G(s)\}(t)|_{t=nT}\right\}$, where T is the sampling period, $\mathcal{L}$ is the Laplace transform and $\mathfrak{Z}$ is the z-transform.

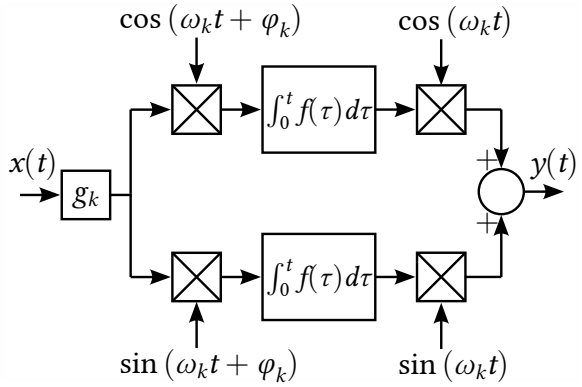

Figure 3.1: Continuous-time AFC resonator diagram.

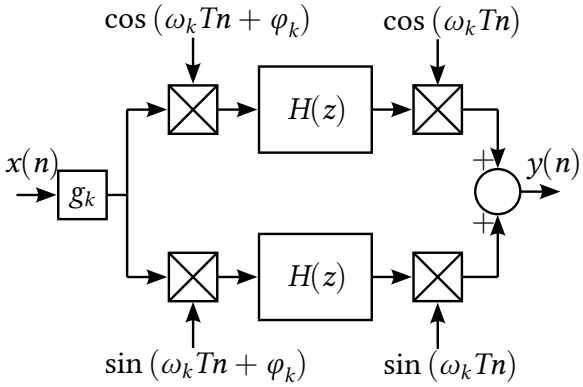

Figure 3.2: Discrete-time AFC resonator diagram.

Proof. Decomposing the sin and cos functions in exponential functions and applying the scaling in the z-domain property from the z transform

$$\mathcal{Z}\left\{a^n x(n)\right\} = X(a^{-1}z),$$

one can show that the equation of a discrete-time resonator, given by

$$\begin{aligned} y(n) = \mathcal{Z}^{-1}\left\{\mathcal{Z}\left\{g_k x(n)\cos\left(\omega_k Tn + \varphi_k\right)\right\}H(z)\right\}\cos\left(\omega_k Tn\right) + \\ \mathcal{Z}^{-1}\left\{\mathcal{Z}\left\{g_k x(n)\sin\left(\omega_k Tn + \varphi_k\right)\right\}H(z)\right\}\sin\left(\omega_k Tn\right), \end{aligned}$$

can be simplified into

$$\begin{aligned} Y(z) = \frac{1}{4}\left[\mathrm{e}^{-\mathrm{j}\varphi_k} g_k X(z\mathrm{e}^{\mathrm{j}nT\omega_k}) + \mathrm{e}^{\mathrm{j}\varphi_k} g_k X(z\mathrm{e}^{-\mathrm{j}nT\omega_k})\right] H(z)\,|_{z=\mathrm{e}^{-\mathrm{j}\omega_k Tn}} + \\ \frac{1}{4}\left[\mathrm{e}^{-\mathrm{j}\varphi_k} g_k X(z\mathrm{e}^{\mathrm{j}nT\omega_k}) + \mathrm{e}^{\mathrm{j}\varphi_k} g_k X(z\mathrm{e}^{-\mathrm{j}nT\omega_k})\right] H(z)\,|_{z=\mathrm{e}^{\mathrm{j}\omega_k Tn}} + \\ \frac{1}{4}\left[\mathrm{e}^{-\mathrm{j}\varphi_k} g_k X(z\mathrm{e}^{\mathrm{j}nT\omega_k}) - \mathrm{e}^{\mathrm{j}\varphi_k} g_k X(z\mathrm{e}^{-\mathrm{j}nT\omega_k})\right] H(z)\,|_{z=\mathrm{e}^{-\mathrm{j}\omega_k Tn}} - \\ \frac{1}{4}\left[\mathrm{e}^{-\mathrm{j}\varphi_k} g_k X(z\mathrm{e}^{\mathrm{j}nT\omega_k}) - \mathrm{e}^{\mathrm{j}\varphi_k} g_k X(z\mathrm{e}^{-\mathrm{j}nT\omega_k})\right] H(z)\,|_{z=\mathrm{e}^{\mathrm{j}\omega_k Tn}}, \end{aligned}$$

and cancelling, one arrives to

$$Y(z) = \frac{1}{2}\mathrm{e}^{-j\varphi_k} g_k X(z) H(z\mathrm{e}^{-j\omega_k T}) + \frac{1}{2}\mathrm{e}^{j\varphi_k} g_k X(z) H(z\mathrm{e}^{j\omega_k T})$$

which is equivalent to the expression 3.3. □

Finally, if a backward Euler integrator is chosen, i.e., $H(z) = \frac{z}{z-1}$, then, the z-

domain transfer function of the resonator becomes

$$R_k(z) = g_k \frac{\cos(\varphi_k) z^2 - \cos(\omega_k T + \varphi_k) z}{z^2 - 2\cos(\omega_k T) z + 1}, \tag{3.4}$$

which is exactly the same transfer function that one obtains by performing the transform in (3.2) with the transfer function[2] (3.1).

This result shows that it is worth working directly in discrete-time instead of translating a transfer function from continuous time; observe that the $H(z)$ block can be any kind of integrator, giving different properties to the resonator. As it will be addressed later in this chapter, the $H(z)$ block may even be a transfer function with finite gain at 0 Hz.

Analysing (3.4), it can be deduced that the transfer function has two poles and two zeros: both poles are marginally stable, placed at $z = e^{\pm \omega_k T}$, one zero is placed at $z = 0$ and the second one is placed at $z = \frac{\cos(\omega_k T + \varphi_k)}{\cos(\varphi_k)}$. This last zero is a function of φ_k, and as it will be explained later, it may be (and usually is) out of the unit circle, that is, it may be non-minimum phase (NMP). However, even if it seems unusual to the conventional placement of zeros, the same happens in continuous time, where this NMP-zero plays an important role for the controller robustness (Messner and Bodson, 2007).

3.2.1 Control Structure

Let's suppose the discrete-time control diagram depicted in Fig. 3.3, where the plant to be controlled is $P(z)$ and the AFC controller is $K(z)$. The usual structure of $K(z)$ is the addition of N resonators in parallel, $\sum_{k=1}^{N} R_k(z)$, giving infinite gain to the open-loop transfer function $L(z) = K(z)P(z)$ at the fundamental frequency (and the harmonics) of the reference signals to be tracked and the disturbance signals to be rejected. The plant $P(z)$ may be a closed-control loop, as in (Byl et al., 2005) to reduce the control effort of the resonant controller.

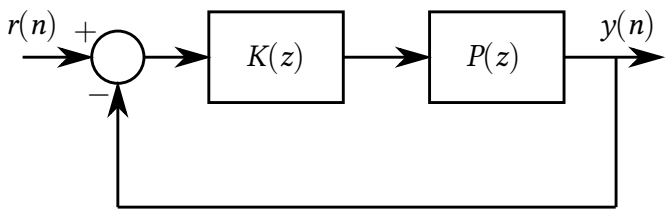

Figure 3.3: Discrete-time control diagram.

[2] This can be shown by a simply substitution operation.

Each resonator has two parameters to be tuned: the gain g_k and the angle φ_k. A control system with several resonators must be carefully designed and implemented by three main reasons:

- first, the controller order will be high and it must remain stable, so the resonator parameters must be chosen properly,
- second, the computation time grows with each resonator due to the increasing number of mathematical operations[3],
- and third, resonators they are sensitive to computation numerical errors since their poles are exactly over the unit circle[4].

3.2.2 AFC Control Design for Low Gains

3.2.2.1 Resonators Angles

When all the resonator gains g_k tend to 0, the closed-loop poles tend to the open-loop transfer function $L(z)$ ones, i.e., all the resonators poles tend to a position on the unit circle. Therefore, the departure angle is crucial for stability.

In continuous time, it has been shown with several different techniques that each resonator angle φ_k must coincide with the phase of the plant at each resonator frequency $\angle P(j\omega_k)$ in order to maximise the phase margin. Hence, when g_k increases, all the poles move into the open left half-plane with a perpendicular trajectory with respect to the imaginary axis (Messner and Bodson, 2007). Furthermore, one can see that the phases of the open-loop transfer function, $\angle L(j\omega_k)$, at the resonator frequencies ω_k, are zero, what is a sign of robustness (Byl et al., 2005).

The question is now if one can obtain some kind of equivalence of these design rules for a discrete-time system using discrete-time resonators. In order to answer this question, the idea is to force all resonators poles to follow the most robust possible trajectory when g_k increases, that is, the perpendicular line to the tangent of the unit circle at the point of departure[5], and analyse what happens to the resonators angles.

Fig. 3.4 shows the most robust closed-loop poles trajectories in a continuous-time system and in a discrete-time one.

[3]Each resonator increases by 2 the order of the controller and needs only 5 products and 3 additions (two from the discrete-time integrators). The necessary operations needed to compute the carriers of each frequency are carried out recursively from the signal produced by a PLL.

[4]That is why a resonator should not be implemented as a transfer function (any quantisation problem could lead to an unstable system), but as the diagram shown in Fig. 3.2

[5]An horizontal line over the s-plane ($\mathbb{I}\mathrm{m} = a$) becomes a straight line passing through the origin with slope aT, where T is the sampling period.

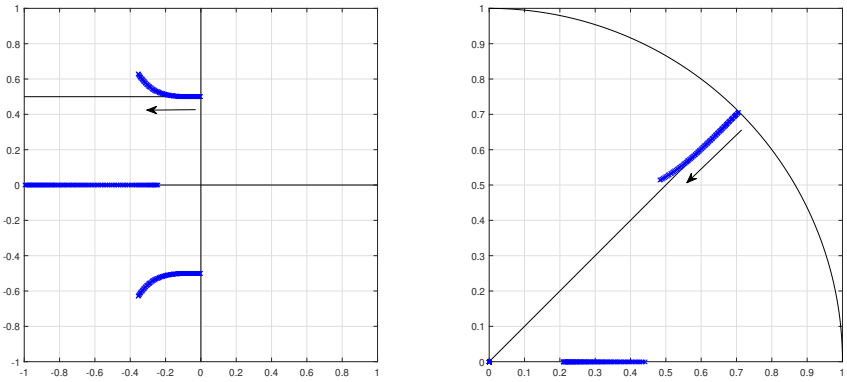

Figure 3.4: Desired closed-loop poles trajectories to maximise the robustness of a continuous-time system (left) and a discrete-time one (right).

Following Fig. 3.3, the closed-loop transfer function is $M(z) = \frac{K(z)P(z)}{1+K(z)P(z)}$, so the closed-loop poles are the roots of

$$1 + K(z)P(z) = 0. \tag{3.5}$$

Moreover, one can state that z is a function of each g_k, i.e., $z(g_k)$. Computing the derivative of $1 + K(z(g_k))P(z(g_k)) = 0$ with respect to each g_k when $g_k = 0$, it is possible to obtain the poles departure angles, since the place of the poles when $g_k = 0$ are known (those of the open-loop transfer function $L(z)$).

Next, setting $z(g_k) = \rho(g_k)e^{j\theta(g_k)}$, and replacing $z(0)$ by[6] $e^{j\omega_k T}$ and $z'(0)$ by $e^{j\omega_k T}\rho'(0) + je^{j\omega_k T}\theta'(0)$, one obtains the expression

$$H_n(1)P(e^{j\omega_k T}) + 2H_d'(1)\left[\rho'(0) + j\theta'(0)\right]e^{j\varphi_k} = 0. \tag{3.6}$$

The proof leading to 3.6 can be found below.

Proof. When the gains g_k are null, all the closed-loop resonator poles are on the unit circle. In order to evaluate their departure angle when the gain g_k increases, it is necessary to compute the derivative of the z variable in function of g_k with $g_k = 0$. Resonators are going to be used in the general form presented in (3.3). Nevertheless, to avoid any indeterminate form, one can split them in numerator and denominator

[6]Due to the symmetry of this problem, only positive frequencies will be considered.

as $R_k(z) = \frac{1}{2} g_k \frac{R_{nk}(z)}{R_{nk}(z)}$. Therefore, equation (3.5) can be written as

$$2\prod_{k=1}^{N} R_{dk}(z) + P(z)\sum_{k=1}^{N} g_k R_{nk}(z) \prod_{i=1, i\neq k}^{N} R_{di}(z) = 0. \tag{3.7}$$

Note that the variable z is a function of g_k. Without loss of generality, the implicit derivative is going to be carried out with respect to the gain g_1 (the same process could be carried out again with any g_k). Therefore, equation (3.7) can be rewritten as

$$\begin{aligned} 2R_{d1}(z(g_1))\prod_{k=2}^{N} R_{dk}(z(g_1)) + P(z(g_1))g_1 R_{n1}(z(g_1))\prod_{k=2}^{N} R_{dk}(z(g_1)) + \\ P(z(g_1))\sum_{k=2}^{N} g_k R_{nk}(z(g_1)) \prod_{i=1, i\neq k}^{N} R_{di}(z(g_1)) = 0. \end{aligned} \tag{3.8}$$

The derivative of the first term with respect to the gain g_1 when $g_1 = 0$ is simply

$$2R'_{d1}(e^{j\omega_1 T})z'(0)\prod_{k=2}^{N} R_{dk}(e^{j\omega_1 T}),$$

since[7] $z(0) = e^{j\omega_1 T}$ and[8] $R_{d1}(e^{j\omega_1 T}) = 0$.

The derivative of the second term when $g_1 = 0$ is

$$P(e^{j\omega_1 T})R_{n1}(e^{j\omega_1 T})\prod_{k=2}^{N} R_{dk}(e^{j\omega_1 T}).$$

And finally, the derivative of the third term is null, since again, $R_{d1}(e^{j\omega_1 T}) = 0$ and all the gains g_k are supposed to be null. Consequently, the derivative of (3.8) can be written as

$$2R'_{d1}(e^{j\omega_k T})z'(0) + P(e^{j\omega_1 T})R_{n1}(e^{j\omega_1 T}) = 0.$$

Replacing $R_{n1}(e^{j\omega_1 T})$ by[9] $H_n(1)H_d(e^{j2\omega_1 T})e^{-j\varphi_1}$, $R'_{d1}(e^{j\omega_1 T})$ by $H'_d(1)e^{-j\omega_1 T}H_d(e^{j2\omega_1 T})$ and simplifying, one arrives to the equation

$$2H'_d(1)e^{-j\omega_1 T}z'(0) + P(e^{j\omega_1 T})H_n(1)e^{-j\varphi_1} = 0,$$

where it is only necessary to replace $z'(0)$ by $e^{j\omega_1 T}\rho'(0) + je^{j\omega_1 T}\theta'(0)$ to obtain the

[7] Due to the root locus symmetry, only positive frequencies are considered.
[8] $R_{d1}(e^{j\omega_1 T}) = H_d(1)H_d(e^{j2\omega_1 T})$ and $H_d(1) = 0$ since the denominator of an integrator is $z - 1$.
[9] The numerator $R_{n1}(e^{j\omega_1 T})$ is $H_n(1)H_d(e^{j2\omega_1 T})e^{-j\varphi_1} + H_n(e^{j2\omega_1 T})H_d(1)e^{j\varphi_1}$, that is, $H_n(1)H_d(e^{j2\omega_1 T})e^{-j\varphi_1}$.

expression (3.6). □

Setting $P(e^{j\omega_k T}) = |P_k|e^{j\psi_k}$ (the module and the angle of the plant $P(z)$ at the frequency $\omega_k T$) and separating this equation into its real and imaginary parts, the resulting two-equation system can be solved in order to find the unknowns $\rho'(0)$ and $\theta'(0)$

$$\begin{aligned}\rho'(0) &= -\frac{|P_k|H_n(1)}{2H_d'(1)}\cos(\psi_k - \varphi_k)\\ \theta'(0) &= -\frac{|P_k|H_n(1)}{2H_d'(1)}\sin(\psi_k - \varphi_k).\end{aligned} \tag{3.9}$$

Finally, forcing the departure angles to be perpendicular to the tangent of the the unit circle at the point of departure, $\theta'(0) = 0$, one obtains the relationship between the resonators angles φ_k and the plant angles ψ_k; if it is chosen $\psi_k = \varphi_k$, it can be observed that, indeed, the trajectories for low gains will be the most robust one. Now, those trajectories will move towards the origin if $\rho'(0) < 0$, that is, if $\frac{H_n(1)}{H_d'(1)} > 0$ ($|P_k|$ is always positive), what is always true for an integrator.

This result shows that in discrete time, one arrives at the same conclusion as in continuous time: for low gains, the resonators angles φ_k must coincide with the plant angles ψ_k at the frequencies $\omega_k T$ to obtain the maximum phase margin. In other words, the estimated angle of the plant can be incorrect by as much $\pm\frac{\pi}{2}$ rad, exactly as in (Messner and Bodson, 2007), and the poles will still move into the unit circle.

On the other hand, another property follows from the previous demonstration. The addition of a resonator, causes a loss of π rad at the frequency which it is tuned. Choosing the angles for the resonators equal to those to the plant $\psi_k = \varphi_k$ at the working frequencies $\omega_k T$, it can be shown from (3.3) that the open-loop transfer function $L(z)$ presents a null phase at each resonator frequency $\omega_k T$. This can be explained since the phase of a resonator at ω_k is $-\varphi_k$ rad[10], exactly as shown in continuous time in (Byl et al., 2005).

Fig. 3.5 depicts the areas where the resonator zero is or not minimum phase in function of the frequency $\omega_k T$ and the angle φ_k. Since $\varphi_k = \psi_k$, the usual working area has been marked, showing that probably, the zero will be out of the unit circle. Normally, plants phases starts at 0 rad and diminish up to $-\frac{\pi}{2}$. On the other hand, the frequency $\omega_k T$ depends on the control system specifications, but in general remains in the first quadrant $[0, \frac{\pi}{2}]$.

[10] At the $\omega_k T$ frequency, the resonator phase presents a discontinuity of π rad, but the average is $-\varphi_k$, see (Malo and Griñó, 2008).

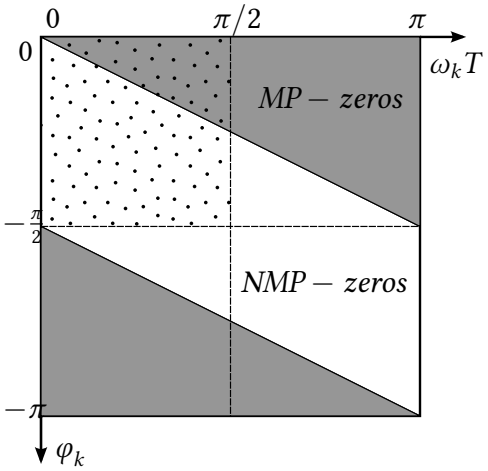

Figure 3.5: Areas where the resonator zero is MP or NMP in function of $\omega_k T$ and φ_k.

3.2.2.2 Resonators Gains

The design method presented for tuning the φ_k resonators angles ensures the maximum phase margin for low gains. The low-gain condition comes from the fact that the angles property is local and it is only valid for small values of $g_k > 0$. Furthermore, the g_k values cannot be increased indefinitely since the closed-loop poles tend to the open-loop transfer function zeros, and they are usually non-minimum-phase, giving an unstable system[11]. This fact can be explained because:

- first, the angles φ_k may place the resonators zeros outside the unit circle as previously explained,
- and second, most likely the plant $P(z)$ has been obtained from a continuous-time plant $P(s)$ using a ZOH and then, in general, it has relative degree of 1. This fact implies in some cases the appearance of sampling zeros, and usually the second one is non-minimum-phase (Åström et al., 1984).

Therefore, the pair stability and robustness are the keys to choose the gains values. A good indicator of robustness is the inverse of the sensitivity transfer function infinity norm $d = \|S(z)\|_\infty^{-1}$, where $S(z) = (1+L(z))^{-1}$. The value d represents the minimum distance from the open-loop transfer function polar plot, $L(e^{j\omega T})$, to the critical point -1. This constitutes an important robustness margin and gives significant informations about the closed-loop system. As a general design rule for robust controllers, the d value should be between 0.5 and 0.75 (Garcia et al., 2007).

3.2.2.3 Application Example

This example has been borrowed and adapted from (Messner and Bodson, 2007). Fig. 3.6 shows the plant to be controlled by means of a resonator. Being $P(s) =$

[11] Non-minimum-phase zeros are out of the unit circle

$\frac{1}{(s+10)(s+1)}$ the plant, $R_1(z) = g_1 \frac{\cos(\varphi_1)z^2 - \cos(\omega_1 T + \varphi_1)z}{z^2 - 2\cos(\omega_1 T)z + 1}$ the resonator and $r(n) = \sin(\omega_1 nT)$ the signal reference. The working frequency is $\omega_1 = \frac{1}{2}\,\frac{\text{rad}}{\text{s}}$.

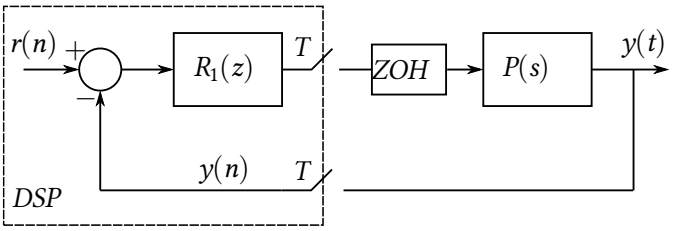

Figure 3.6: Control diagram of the sampled-data control system. The plant $P(s)$ is continuous-time and the control system works in discrete-time.

In order to perform the control design, the plant $P(s)$ is going to be discretised. For the sake of simplicity, the sampling period has been fixed to $T = \frac{\pi}{2}$ s. Applying the transformation (3.2), the obtained equivalent discrete-time plant is $P(z) = \frac{0.0769z + 0.00231}{z^2 - 0.2079z + 3.133\cdot 10^{-8}}$. In this plant, if necessary, one could add some sampling effects, as the computational delay as a pole at $z = 0$.

In Fig. 3.7, it can be observed the system root locus in the neighbourhood of $z = e^{j\frac{\pi}{4}}$ (one of the resonator poles) if the $\varphi_1 = \psi_1$ design rule is applied: the angle of the resonator φ_1 is the same as the angle of the plant $P(z)$ at the frequency $\omega_1 T = \frac{\pi}{4}$, i.e., $\psi_1 = \angle P(j\omega_1 T) = -0.9768$ rad. The gain g_1 is a positive value starting at 0.

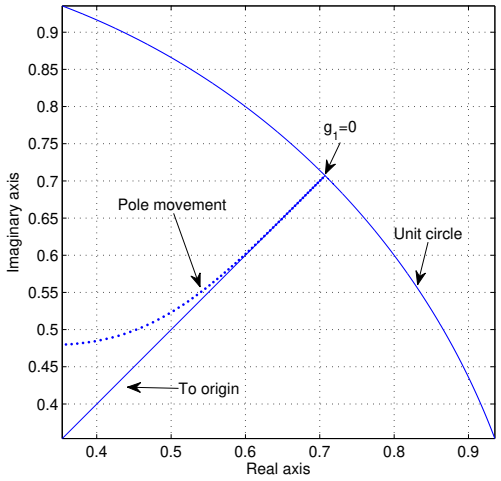

Figure 3.7: System root locus for low gain g_k in the neighbourhood of the resonator pole with $z = e^{j\frac{\pi}{4}}$.

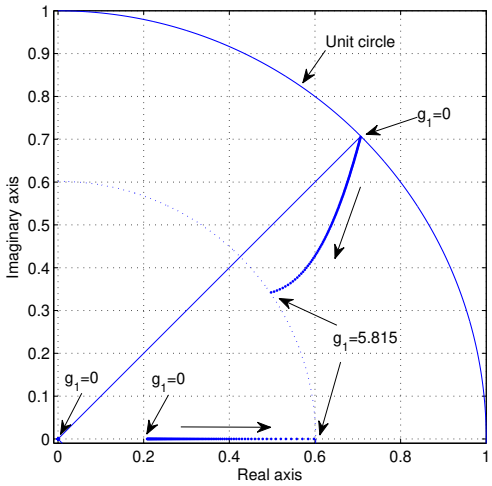

Figure 3.8: Root locus showing the point that minimises the modulus of the dominating closed-loop poles.

Indeed, for low gains, the departure angle of the pole is perpendicular to the tangent of the unit circle at the point of departure, and it moves towards the origin.

Note also that the zero of the resonator is NMP: $z = \frac{\cos(\omega_1 T + \varphi_1)}{\cos(\varphi_1)} = 1.7542$. Nevertheless, this is the angle φ_1 that maximises the phase margin.

Regarding the tuning of the gain, the only condition is that it has to be small. For example, a gain of $g_1 = 2$ gives a minimum distance from the open loop Nyquist plot to the critical point of $d = 0.856$, but the settling time is around 60 s. This is a robust solution, but the gain could be increased to adjust the balance robustness/time response.

As an experiment, a set of phase φ_1 and gain g_1 values that minimises the transient duration can be found. For a determined value of φ_1, when increasing the gain g_1, resonator poles first move towards the origin and the dominant pole of the plant moves the opposite. Therefore, the optimum point occurs when the three poles are at the same distance from the origin. This distance from the origin is a function of φ_1, and can also be minimised.

As depicted in Fig. 3.8, the found values minimising the transient duration are $g_1 = 5.815$ and $\varphi_1 = -1.505$ rad. In this case $d = 0.319$, but the settling time reduces to 15 s approximately. These results can be observed in simulations depicted in Figs. 3.9 and 3.10.

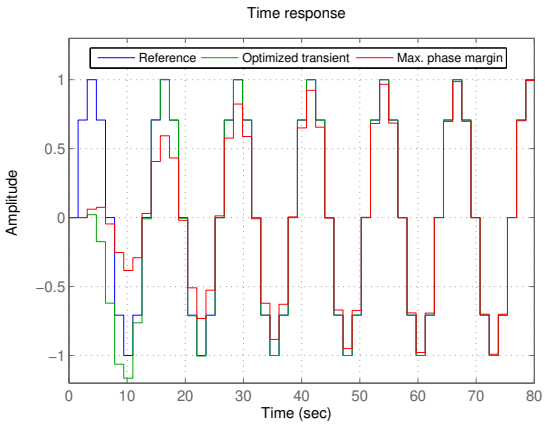

Figure 3.9: Comparison of both transient responses: reference (blue), maximum phase margin (red) and optimised transient (green).

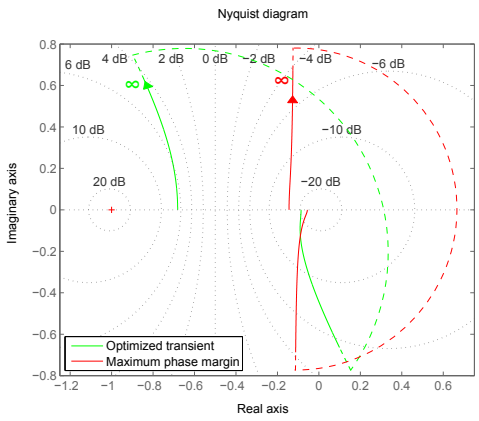

Figure 3.10: Comparison of the the open-loop Nyquist plots: maximum phase margin (red) and optimised transient (green).

The dashed lines in Fig. 3.10 represent the π rad leap with infinite gain produced at the resonator frequency. For the case where the phase margin is maximum, the asymptote produced by the discontinuity is perpendicular to the real axis, giving the maximum robustness to the system. Any deviation in this angle will move the polar plot closer to the critical point -1.

3.2.3 AFC Control Design for Arbitrary Gains

The problem of finding the resonators gains can be seen as an LTI parameter-dependent (LTIPD) system or a fixed-order controller design.

In (Zhang, 2003), the stability problem of arbitrary LTIPD systems is extensively investigated: it is a non-convex non-smooth problem and probably, without an analytic solution. However, the theory developed based on Lyapunov functions is very interesting from the mathematical point of view.

Still, the need of a general criterion for tuning the resonator gains leads to the consideration of using numerical algorithms, and fortunately, there are some research lines dealing with this problem, for example the fixed-order controller design problem. Two of these options are HInfStruct (Apkarian and Noll, 2006, Bruinsma and Steinbuch, 1990) and HIFOO (Arzelier et al., 2011, Gumussoy et al., 2009).

Since the slowest time constant of a system is related to the farthest pole with respect to the origin, the objective of using an optimisation algorithm is to minimise the transient duration. This is equivalent of finding the optimum gains g_k which minimise the largest pole modulus. It is also necessary to add another condition to set the minimum robustness of the system or to check the robustness of the design found by the numerical methods to assess its viability.

The discrete-time version of HIFOO, HIFOOD, can be used to solve this optimisation problem. HIFOOD is aimed at solving fixed-order stabilisation and performance optimisation problems. It depends on a hybrid algorithm for non-smooth, non-convex optimisation based on quasi-Newton updating and gradient sampling. In particular, HIFOO can address the fixed-order robust stability margin (pseudo-spectral abscissa) optimisation problem. In the Appendix B there is the code for an example using HIFOO to tune the g_k resonators values.

The main drawback of this approach is that the solution found (if any) will be a local optimum and possibly, very sensitive to the initial conditions. However, this method gives a systematic procedure to tune the controllers and it can also be a good starting point to know the order of magnitude of the gains which stabilise the plant.

Finally, it is important to highlight that this algorithm can be also used not only to tune the resonators gains g_k, but also their angles φ_k. Nevertheless, the optimisation problem becomes even harder since the number of parameters to tune is doubled and the controller structure is not a set of constants (static output feedback) any more.

3.3 Finite-Gain Resonators

As it has been shown, resonators gain is infinite at the frequency in which they are tuned, but they decrease very quickly on the neighbourhood, so, frequency variations in the reference or disturbance signals may cause robustness problems and a decrease in the closed-loop system performance (Costa-Castelló et al., 2009). Hence, it is necessary the use of adaptive techniques to keep them continuously tuned at the right frequency. This is normally carried out by a Phase-Locked Loop (PLL), which is always synchronised with the signals to be tracked or rejected. Note that in this case, the associated dynamics of the PLL will have an impact on the global system dynamics and, the dynamical analysis becomes too complex to analyse it.

Therefore, two complementary points are discussed in this section. First, for systems which present low frequency variations (e.g. grid-connected power converters), it would be interesting to determine if the resonators bandwidth are large enough around a fixed frequency (e.g. the nominal electrical grid frequency) to consider getting rid of the PLL. If the answer is affirmative, the second point is to consider if the substitution of the infinite-gain by finite-gain resonators is viable. By suppressing the PLL, the global system dynamical behaviour would be easier to study due to its simpler dynamics, and it might present a faster response. By using finite-gain resonators, even if the tracking error will not be exactly null, the practical implementation is much simpler and less critical since the poles controllers are not any more over the unit circle, but inside.

The block diagram presented in Fig. 3.2 represents a generic resonator. When the $H(z)$ block is a first order system (i.e. $H(z) = \frac{z}{z-a_k}$, with $0 < a_k < 1$), the new resonator transfer function $R_k(z)$ becomes

$$R_k(z) = g_k \frac{\cos(\varphi_k) z^2 - a_k \cos(\omega_k + \varphi_k) z}{z^2 - 2a_k \cos(\omega_k) z + a_k^2}. \tag{3.10}$$

Note that if the new parameter a_k tends to 1, this expression tends to the infinite-gain resonator transfer function (3.4). Analysing (3.10), one can verify that the poles are placed at $z = a_k e^{\pm j\omega_k}$, the maximum of the gain is not infinite any more and it is not placed at the ω_k frequency. In fact, the expression giving the new frequency ω'_k where the maximum can be found is

$$\begin{aligned} 0 = \cos(\varphi_k)\cos(\omega_k + \varphi_k)[(1 - a_k^2)^2 + 2a_k^2(\cos(2\omega_k) - \cos(2\omega'_k))] - \\ [1 + \cos(2\varphi_k) + a_k^2(1 + \cos(\omega_k + \varphi_k))][(1 + a_k^2)\cos(\omega_k) - 2a_k \cos(\omega'_k)]. \end{aligned}$$

This is a complicated equation involving ω'_k and ω_k. If a_k tends to 1, indeed, both frequencies coincide: $\omega'_k = \omega_k$. For a value of $a_k < 1$, supposing ω'_k as a function

of a_k (i.e. $\omega'_k(a_k)$) and finding $\frac{\mathrm{d}}{\mathrm{d}a_k}\omega'_k(a_k)$ (the derivative of ω'_k with respect to the a_k parameter), it can be observed that $\frac{\mathrm{d}}{\mathrm{d}a_k}\omega'_k(a_k)$ is really small (it is proportional to $1-a_k$). Therefore, the supposition that the maximum is placed at ω_k (that is $\omega'_k = \omega_k$) is acceptable, and this value is given by the expression

$$|R_k(\mathrm{e}^{j\omega_k})|^2 = g_k^2 \left(\frac{1 + a_k(1-a_k) - (1-a_k)\cos(2\varphi_k)}{2(1-a_k)^2\,(1 + a_k^2 - 2a_k\cos(2\omega_k))} + \frac{-a_k\cos(2\omega_k) + a_k(1-a_k)\cos[2(\varphi_k+\omega_k)]}{2(1-a_k)^2\,(1 + a_k^2 - 2a_k\cos(2\omega_k))} \right). \tag{3.11}$$

The bandwidth $\Delta\omega_k$ of each finite-gain resonator can be approximately computed from the $H(z)$ transfer function and it can be written as

$$\Delta\omega_k = 2\arccos\left(\frac{1 + a_k^2 - (1-a_k)^2 p_k^2}{2a_k}\right),$$

where $20\log p_k$ represents (in dB) the gain reduction with respect to the resonator maximum value.

Regarding the phase, it does not present a discontinuity at ω_k and its value is not $-\varphi_k$, but it tends to it when a_k tends to 1. Fig. 3.11 shows a comparison between both kind of resonators. Observe that the infinite-gain resonator magnitude is always greater than the finite-gain resonator, but for a_k values close to 1, their behaviour will be really similar.

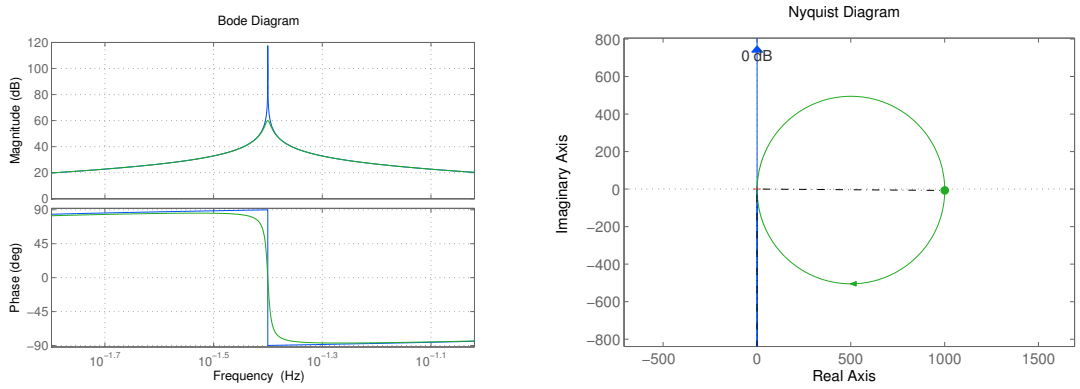

Figure 3.11: Bode and Nyquist diagrams of an infinite-gain (blue) and a finite-gain (green) resonator. The values of the parameters are: $g_k = 2$, $\varphi_k = 0$ and $a_k = 0.999$.

Finite-gain resonators will affect each other at each frequency ω_k and the tracking error will not be null, but the design for each a_k, g_k and φ_k can be performed so this error is really small and the robustness of the system is maximised. Finally, the transfer function derived in (3.10) could be implemented as it is; since $a_k < 1$, there will not be stability issues associated to numerical problems. Furthermore,

the carriers computation is not necessary, so the number of mathematical operations decreases with respect to the infinite-gain resonator.

3.3.1 Robustness Maximisation for Low Gains

Analogously to the infinite-gain resonators case, and following the same controller structure from Fig. 3.3, $K(z)$ will be the addition of N finite-gain resonators in parallel, $\sum_{k=1}^{N} R_k(z)$.

For a fixed a_k value, each resonator has two parameters to be tuned: the gain g_k and the angle φ_k. The open-loop poles are inside the unit circle and the objective is to force all the resonators poles to follow the most robust possible trajectory when g_k increases, that is, the perpendicular line to the tangent of the circle of radius a_k at the point of departure, and towards the origin.

The starting equations for the finite-gain resonators case are the same: the closed-loop transfer function is $T(z) = \frac{K(z)P(z)}{1+K(z)P(z)}$, and the closed-loop poles are the roots of $1 + K(z)P(z) = 0$, exactly as in 3.5.

At this point, one can see the complex variable z as a function of each g_k, i.e., $z(g_k)$. The derivative of $1 + K(z(g_k))P(z(g_k)) = 0$ with respect to each g_k when $g_k = 0$ will give the information about the poles departure angles, since the place of the poles when $g_k = 0$ are known.

Next, setting $z(g_k) = \rho(g_k)e^{j\theta(g_k)}$, and replacing $z(0)$ by[12] $a_k e^{j\omega_k}$ and $z'(0)$ by $e^{j\omega_k}\rho'(0) + a_k j e^{j\omega_k}\theta'(0)$, one obtains the expression

$$0 = H_n(a_k)P(a_k e^{j\omega_k}) + 2H'_d(a_k)\left[\rho'(0) + a_k j\theta'(0)\right]e^{j\varphi_k} \tag{3.12}$$

The proof which leads to 3.12 can be found below.

Proof. When the gains g_k are null, all the closed-loop resonator poles are on the circle of radius a_k. Exactly as in the case of infinite-gain resonators, the information about their departure angle when the gain g_k increases is in the derivative of the z variable in function of g_k at $g_k = 0$. Starting from the equation (3.8), the derivative of the first term with respect to the gain g_1 when $g_1 = 0$ is

$$2R'_{d1}(a_1 e^{j\omega_1})z'(0)\prod_{k=2}^{N} R_{dk}(a_1 e^{j\omega_1}),$$

since[13] $z(0) = a_1 e^{j\omega_1}$ and[14] $R_{d1}(a_1 e^{j\omega_1}) = 0$.

[12] Due to the symmetry of this problem, only positive frequencies will be considered.
[13] Due to the root locus symmetry, only positive frequencies are considered.
[14] $R_{d1}(a_1 e^{j\omega_1}) = H_d(a_1)H_d(a_1 e^{j2\omega_1})$ and $H_d(a_1) = 0$ since the denominator of the transfer function is

The derivative of the second term with respect to g_1 when $g_1 = 0$ is

$$P(a_1 e^{j\omega_1}) R_{n1}(a_1 e^{j\omega_1}) \prod_{k=2}^{N} R_{dk}(a_1 e^{j\omega_1}).$$

And finally, the derivative of the third term with respect to g_1 when $g_1 = 0$ is null, since again, $R_{d1}(a_1 e^{j\omega_1}) = 0$ and all the gains g_k are supposed to be null.

Consequently, the derivative of (3.8) turns out to be

$$2R'_{d1}(a_1 e^{j\omega_1}) z'(0) + P(a_1 e^{j\omega_1}) R_{n1}(a_1 e^{j\omega_1}) = 0.$$

Replacing $R_{n1}(a_1 e^{j\omega_1})$ by[15] $H_n(a_1) H_d(a_1 e^{j2\omega_1}) e^{-j\varphi_1}$, $R'_{d1}(a_1 e^{j\omega_1})$ by $H'_d(a_1) e^{-j\omega_1} H_d(a_1 e^{j2\omega_1})$ and simplifying, one arrives to the equation

$$2H'_d(a_1) e^{-j\omega_1} z'(0) + P(a_1 e^{j\omega_1}) H_n(a_1) e^{-j\varphi_1} = 0,$$

where it is only necessary to replace $z'(0)$ by $e^{j\omega_1}\rho'(0) + a_1 j e^{j\omega_1}\theta'(0)$ to obtain the expression (3.12). □

Setting $P(a_k e^{j\omega_k}) = |P_k| e^{j\psi_k}$ (the module and the angle of the plant $P(z)$ when z is replaced by $a_k e^{\omega_k}$) and separating this equation into its real and imaginary parts, the resulting two-equation system can be solved in order to find the unknowns $\rho'(0)$ and $\theta'(0)$

$$\rho'(0) = -\frac{|P_k| H_n(a_k)}{2H'_d(a_k)} \cos(\psi_k - \varphi_k)$$
$$\theta'(0) = -\frac{|P_k| H_n(a_k)}{2H'_d(a_k)} \sin(\psi_k - \varphi_k).$$

Thus, forcing the departure angles to be perpendicular to the tangent of the circle of radius a_k at the point of departure, $\theta'(0) = 0$, one obtains the relationship between the resonators angles φ_k and the plant angles ψ_k; if it is chosen $\varphi_k = \psi_k$, it can be observed that, indeed, trajectories for low gains will be the predicted ones. Those trajectories will move towards the origin if $\rho'(0) < 0$, that is, if $\frac{H_n(a_k)}{H'_d(a_k)} > 0$ ($|P_k|$ is always positive).

It is important to observe that when performing the limit when a_k tends to one,

$z - a_1$.

[15] The numerator $R_{n1}(a_1 e^{j\omega_1})$ is $H_n(a_1) H_d(a_1 e^{j2\omega_1}) e^{-j\varphi_1} + H_n(a_1 e^{j2\omega_1}) H_d(a_1) e^{j\varphi_1}$, that is, $H_n(a_1) H_d(a_1 e^{j2\omega_1}) e^{-j\varphi_1}$.

this condition becomes the rule for infinite-gain resonators

$$\lim_{a_k \to 1} \psi_k = \lim_{a_k \to 1} \angle P(a_k e^{j\omega_k}) = \angle P(e^{j\omega_k}).$$

3.3.2 Finite-Gain Resonator Design

In order to obtain a robust resonator design, first it must be set the value of the open-loop transfer function $L(z)$ at the ω_k frequency, b_k (e.g. $b_k = 1000$, that is, 60 dB). This value must be large since it will determine the controller performance at the nominal frequency ω_k. Then, it must be chosen the value p_k, which represents the gain between the maximum (b_k) and the line where the gain curve will present the desired bandwidth $\Delta\omega_k^*$ (e.g. $-20 \log p_k = -30$ dB.). Therefore, the value $\frac{b_k}{p_k}$ determines the controller performance at the bounds of the desired bandwidth, that is, p_k represents the maximum detuning of the controller over $\Delta\omega_k^*$. The equation which relates the parameters p_k and $\Delta\omega_k^*$ to a_k is

$$a_k = \frac{p_k^2 - \cos\left(\frac{\Delta\omega_k^*}{2}\right)}{p_k^2 - 1} - \frac{\sqrt{-1 + 2p_k^2 - 2p_k^2 \cos\left(\frac{\Delta\omega_k^*}{2}\right) + \cos^2\left(\frac{\Delta\omega_k^*}{2}\right)}}{p_k^2 - 1} \tag{3.13}$$

The values of the open-loop maxima are given by the square root of the expression (3.11), which depends linearly on the g_k gains, multiplied by the gain of the plant at the ω_k frequencies (i.e. $|P(e^{j\omega_k})|$). The different p_k values should be chosen to ensure that the resulting parameters a_k are under the closest value of 1 that will produce numerical issues in the arithmetic unit working precision that is going to be used to compute the control signal (e.g. single, double, etc.). Note that, for a fixed bandwidth, the bigger p_k is, the closer a_k will be to 1 and the smaller $\frac{b_k}{p_k}$ value will be.

Once all the a_k parameters have been obtained, the φ_k angles can be computed by applying the rule deduced in the previous Section: $\varphi_k = \angle P(a_k e^{j\omega_k})$.

Finally, the g_k values must be those that will fulfil the condition imposed by b_k. Obviously, they must be smaller than the critical value that will destabilise the system and it is important to verify the robustness of the final controller. If the computed values of g_k give a low robust controller or an unstable plant, the b_k and p_k values need to be arranged in order to obtain new less demanding specifications.

The design procedure above-mentioned can be summarised as follows:

- **Step 1**. Choose the desired maximum values of the open-loop transfer function $L(z)$ at the ω_k frequency.

- **Step 2**. Determine the necessary a_k which are a function of the desired bandwidths $\Delta\omega_k^*$ and the gain decay set by p_k by means of the expression (3.13).

- **Step 3**. Compute all the φ_k thanks to the design rule derived in the previous Section: $\varphi_k = \angle P(a_k e^{j\omega_k})$.

- **Step 4**. Set the gains g_k which fulfils the condition imposed in Step 1. Verify that these g_k does not destabilise the control system and verify that it is robust enough.

3.3.3 Implementation Example

Let's consider again the continuous-time transfer function $P(s)$ with two stable poles $s = -1$ and $s = -10$: $P(s) = \frac{10}{(s+1)(s+10)}$. In Table 3.1, all the used parameters are listed.

Table 3.1: System Parameters for a Finite-Gain Resonator Controller Design.

T	$\frac{\pi}{8}$ s
$\omega_1 T$	$\frac{1}{4}\ \frac{\text{rad}}{\text{s}}$
$\Delta\omega_1^* T$	$0.02\ \omega_1 T\ \frac{\text{rad}}{\text{s}}$
$20 \log b_1$	60 dB
$20 \log p_1$	25 dB

The resulting discrete-time plant $P(z)$ discretised using a ZOH (Zero-Order Hold) at the sampling period T is $P(z) = \frac{0.2519z+0.06644}{z^2-0.6949z+0.0133}$. The gain at the $\omega_1 T$ frequency is $|P(e^{j\omega_1 T})| = 0.969661$. On the other hand, using p_1 and $\Delta\omega_1^* T$ in expression (3.13), a value for $a_1 = 0.9999447$ is obtained. Once a_1 has been determined, φ_k can be computed by using the design rule in Step 3; therefore $\varphi_1 = \angle P(a_1 e^{j\omega_1 T}) = -0.319743$ rad. Fig. 3.12 depicts the closed-loop poles for low gains. As it can be observed, when g_1 increases, the trajectory is perpendicular to the tangent of the circle of radius a_k at the point of departure, and towards the origin. In this case, a_k is really close to 1 and the closed-loop pole departure angle is almost the same with respect to the infinite-gain resonators case. The differences get more noticeable as a_k decreases.

The gain g_1 must be chosen to fulfil the condition imposed by b_1, but the system must remain stable. In this case, the necessary gain is $g_1 = 0.1140639$. With this g_1, the value of the open-loop system gain at ω_1 is $20 \log |L(e^{j\omega_1 T})| = 60$ dB, so the gain

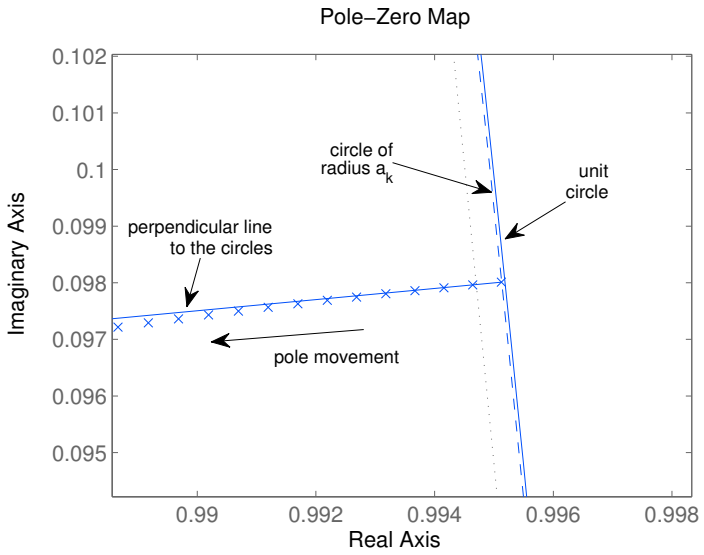

Figure 3.12: Finite-gain closed-loop poles when gains g_k are low.

at the frequencies $(\omega_1 \pm \frac{\Delta\omega_1^*}{2})T$ is $20\log|L(e^{j(\omega_1 \pm \frac{\Delta\omega_1^*}{2})T})| = 20\log\left(\frac{|L(e^{j\omega_1 T})|}{p_k}\right) = 35\,\text{dB}$, as expected.

The open-loop and closed-loop transfer-function bode diagrams are shown in Fig. 3.13 and the open-loop Nyquist diagram in depicted in Fig. 3.14. Observe that the system is stable and robust, since the minimum distance from the open-loop Nyquist diagram to the critical point -1 is $d = \frac{1}{\|S(z)\|_\infty} = 0.689857$, where $S(z) = \frac{1}{1+L(z)}$ is the closed-loop sensitivity transfer function.

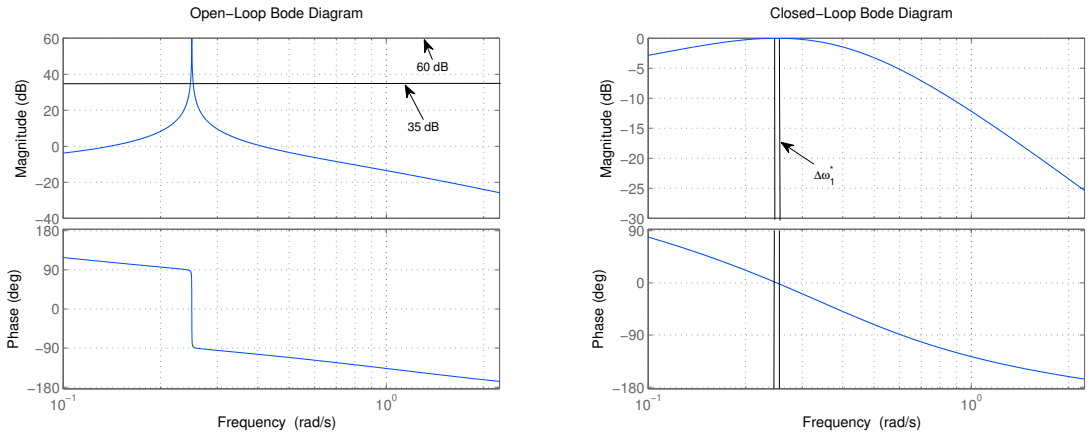

Figure 3.13: Open-loop (left) and closed-loop (right) transfer-function bode diagrams.

Finally, the system responses and the tracking errors when the reference signal frequency is $\omega_1 T$ and $(\omega_1 + \frac{\Delta\omega_1}{2})T$ are depicted in Fig. 3.15. Note that the reference is well tracked in both cases; in the first one, the closed-loop transfer function

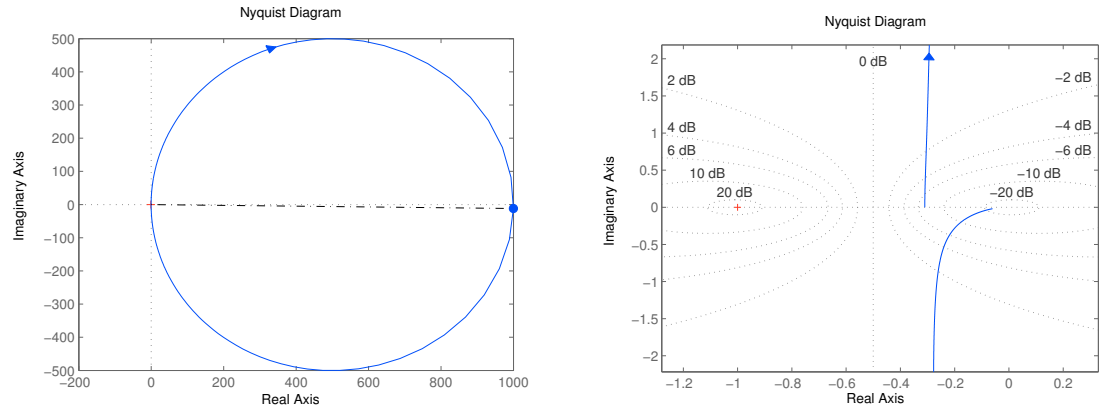

Figure 3.14: Open-loop Nyquist diagram (left) and a detail zoom near the critical point -1 (right).

$T(z)$, regarding the reference signal amplitude, presents a gain of 0.999001 and a phase equal to $-2.079154 \cdot 10^{-7}$ rad and in the second one, the closed-loop gain is 0.998943 and the phase is -0.017676 rad. As it can be observed, the error is due basically to the phase shift and not to the gain. The error $E(z)$ can be computed thanks to the sensitivity transfer function $S(z)$ since $S(z) = \frac{E(z)}{R(z)}$, where $R(z)$ is the reference signal. Therefore, the amplitude of the errors in steady state represented in Fig. 3.15 are given by $|S(e^{j\omega_1 T})| = 0.000999$, that is, a 0.0999% for the first case and $|S(e^{j(\omega_1+\frac{\Delta\omega_1^*}{2})T})| = 0.017699$, that is, a 1.7699% for the second one.

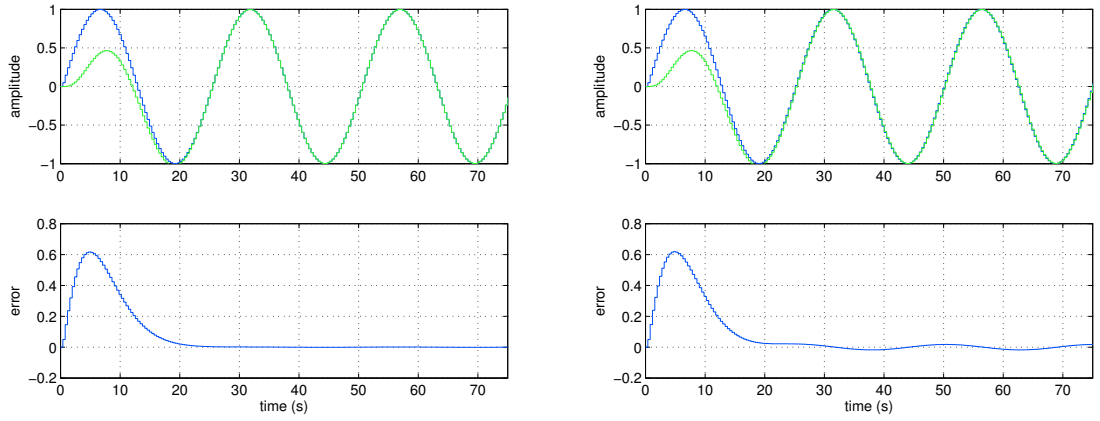

Figure 3.15: Transients and tracking errors when the reference signal frequency is $\omega_1 T$ (left) and $(\omega_1 + \frac{\Delta\omega_1^*}{2})T$ (right).

3.4 Limitation of Resonators Amplitude

Integrators are usually limited to avoid excessive values at their output (for example, to prevent actuators saturation). Nevertheless, if the limit is reached, the

closed loop opens and the permanent error can be integrated in excess producing several dynamical problems, like large overshoots or slow responses in big transients.

An anti-windup protection is always a good practice to keep the integrators value between limits, to fix the maximum disturbance to be rejected by the controller and to avoid excessive overshoots during big transients. However, in tracking problems, linear saturation is not suitable since the signals will be clipped and their frequency spectrum can be significantly modified.

Therefore, in order to avoid distortion on the output signal, the resonators limitation must be performed in their amplitude, which is the envelope of the output signal. This can be seen clearly by analysing the equations describing the resonator dynamic behaviour from[16] Fig. 3.1

$$\begin{aligned} \begin{bmatrix} \frac{\mathrm{d}x_1}{\mathrm{d}t} \\ \frac{\mathrm{d}x_2}{\mathrm{d}t} \end{bmatrix} &= g \begin{bmatrix} \cos(\omega t + \varphi) \\ \sin(\omega t + \varphi) \end{bmatrix} u \\ y &= \begin{bmatrix} \cos(\omega t) & \sin(\omega t) \end{bmatrix} \begin{bmatrix} x_1 \\ x_2 \end{bmatrix} \end{aligned} \tag{3.14}$$

Note that the output amplitude will be given by the value[17] $\rho = \sqrt{x_1^2 + x_2^2}$. In this case, a polar-coordinate transformation is useful to simplify the equations, yielding[18]

$$\begin{aligned} \begin{bmatrix} \frac{\mathrm{d}\rho}{\mathrm{d}t} \\ \rho\frac{\mathrm{d}\theta}{\mathrm{d}t} \end{bmatrix} &= g \begin{bmatrix} \cos(\omega t + \varphi - \theta) \\ \sin(\omega t + \varphi - \theta) \end{bmatrix} u \\ y &= \rho \sin(\omega t + \theta). \end{aligned} \tag{3.15}$$

The amplitude steady-state can only be reached when the input signal u (which is the error signal) is null[19]. Otherwise, since there is not limitation, there will not be an equilibrium and the amplitude will grow indefinitely. Note that even if the input signal u may be composed by the resonator angular frequency ω and other multiples, the only frequency which will be integrated is ω. All the other frequencies will be present in the system, but attenuated since the gain is only infinite at the resonance frequency.

Fig. 3.16 depicts the proposed limitation loop for a continuous-time resonator.

[16] Time dependencies have been dropped.

[17] After some trigonometrical transformations, the resonator output can be rewritten from $y = x_1 \cos(\omega t) + x_2 \sin(\omega t)$ to the expression $y = \sqrt{x_1^2 + x_2^2} \sin\left(\omega t + \arctan\frac{x_2}{x_1}\right)$

[18] The usual polar-coordinate change $\begin{cases} x_1 = \rho\cos(\theta) \\ x_2 = \rho\sin(\theta) \end{cases}$ has been performed.

[19] More precisely, since u may be composed by different harmonics, the steady-state will be attained when the ω frequency is not present in the error signal.

Observe that $\sqrt{x_1^2 + x_2^2}$ is the limited signal and the proportional path K closes the anti-windup loop. The saturation block has its lower limit at 0 (the amplitude cannot be negative) and the upper limit at a fixed value $\bar{\rho}$. This method can be seen as a limitation in the frequency domain since each resonator can be tuned independently.

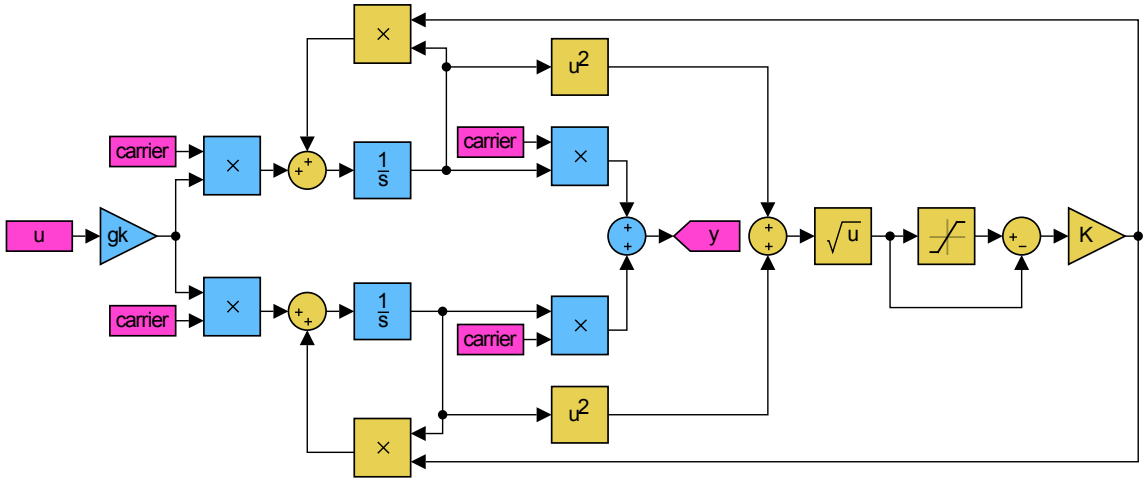

Figure 3.16: Continuous-time limitation block diagram: inputs and outputs are coloured in pink, resonator elements in blue, and the limitation loop in yellow.

After rewriting the equations adding the limitation loop and performing the same change of variables, the new polar-coordinate system supposing positive saturation can be simply written as

$$\begin{aligned} \begin{bmatrix} \frac{\mathrm{d}\rho}{\mathrm{d}t} \\ \rho\frac{\mathrm{d}\theta}{\mathrm{d}t} \end{bmatrix} &= g \begin{bmatrix} \cos(\omega t + \varphi - \theta) \\ \sin(\omega t + \varphi - \theta) \end{bmatrix} u + \begin{bmatrix} 1 \\ 0 \end{bmatrix} K\rho(\bar{\rho} - \rho) \\ y &= \rho\cos(\omega t + \theta). \end{aligned} \tag{3.16}$$

Observe that the amplitude equation is modified by the new limitation term, but the phase equation remains unmodified. This means that, in steady-state, the phase θ will be the same as in the case without limitation. On the other hand, supposing an error of amplitude e at the fundamental frequency ω, the steady-state output amplitude value can be obtained by forcing the derivatives to be zero, yielding to the quadratic equation[20] $\frac{ge}{2} + K\rho^*(\bar{\rho} - \rho^*) = 0$.

The positive solution will give the steady-state saturation value ρ^*, which depends on the upper saturation limit $\bar{\rho}$, the resonator gain g, the anti-windup gain

[20]For simplicity, the oscillating terms with average zero have been dropped since their contribution is negligible. Therefore, the resulting expression is the average value of the real solution.

K, and the amplitude of the error e

$$\rho^* = \frac{\bar{\rho}}{2} + \sqrt{\frac{\bar{\rho}^2}{4} + \frac{ge}{2K}}.$$

It is interesting to highlight that exactly as happens with the usual integrator anti-windup loops, the limit of this value when K tends to infinity is just $\bar{\rho}$, that is, $\lim_{K\to\infty} \rho^* = \bar{\rho}$.

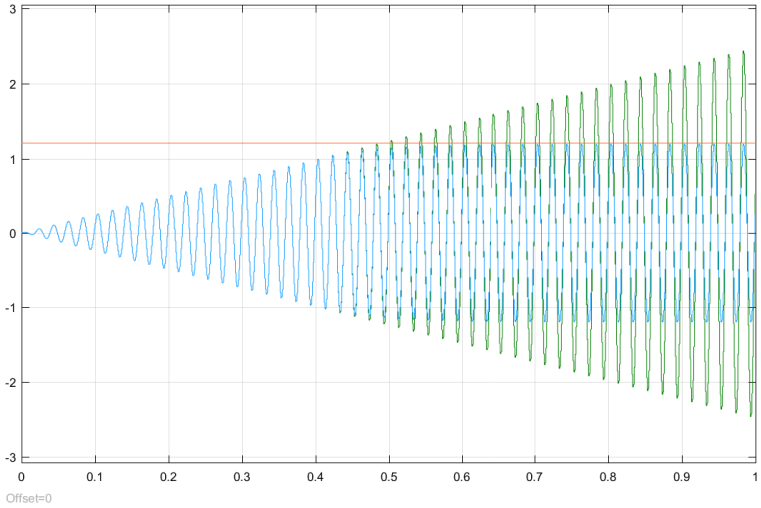

Figure 3.17: Comparison of the output of a resonator with (blue) and without (green) limitation, and the theoretical maximum value (red).

The way of finding the right value of K is the same that for integrator anti-windups. When the saturation is active the main loop opens, the anti-windup one closes and K will determine its dynamics. From (3.16), the differential equation for $\rho(t)$ is[21] $\frac{\mathrm{d}\rho(t)}{\mathrm{dt}} = K\rho(t)(\bar{\rho} - \rho(t))$, whose solution in function of the initial condition $\rho(0)$ can be written as

$$\rho(t) = \frac{\bar{\rho}\mathrm{e}^{K\bar{\rho}t}\rho(0)}{\bar{\rho} + (\mathrm{e}^{K\bar{\rho}t} - 1)\rho(0)}.$$

As is can be observed, the expression is non-linear, but the most relevant element from this expression is time constant $K\bar{\rho}$.

On a final note, this limitation loop can be used directly in discrete-time by simply replacing the continuous-time integrators by discrete-time ones. Fig. 3.17 shows a discrete-time simulation comparing the output of a resonator with and without limitation. The parameters are $T = 1 \cdot 10^{-3}$ s, $e = 1$, $\omega = 2\pi 50 T$ rad $g = 5$ and $K = 10$.

[21] The term depending on the input signal u is neglected since it can be seen as a disturbance when the saturation is active.

With these parameters, the expected value for ρ is approximately 1.21, which matches the simulation result. The fact that the amplitude is limited when the anti-windup loop starts acting, but the phase remains the same for both resonators, guarantees the proper operation of the controller whilst the saturation is active.

"Extraordinary claims require extraordinary evidence."

-Carl Sagan

4

Control Structure and Design

4.1 Introduction

After the power converters analysis, it has been determined that the control objectives are attainable. Also, the resonator, which is the main control component, has been studied and a design method has been developed. Now, it is just a matter of putting all the control elements together in a controller structure.

It is important to highlight that the topologies addressed are almost the same from a control point of view: the full bridge single-phase VSC can be modelled as a single-input single-output (SISO) transfer function and the three-phase three-wire, after the $0\alpha\beta$ transformation, can be seen as two identical and decoupled SISO single-phase transfer functions.

4.2 Digital Control Architecture

Fig. 4.1 and 4.2 show the proposed control block diagram for the single- and three-phase VSC respectively. As it can be observed, it is a typical cascade control loop carried out in two levels: an inner current-control loop and an outer voltage-control loop. Note that for the three-phase VSC there will be 2 identical current controllers running in parallel: one for each of the α and β components.

As it will be explained further down, the carriers used to produce the references for the current controllers are generated by a synchronous reference frame PLL with a Moving Average Filter (SRL-PLL MAF) (Golestan et al., 2014).

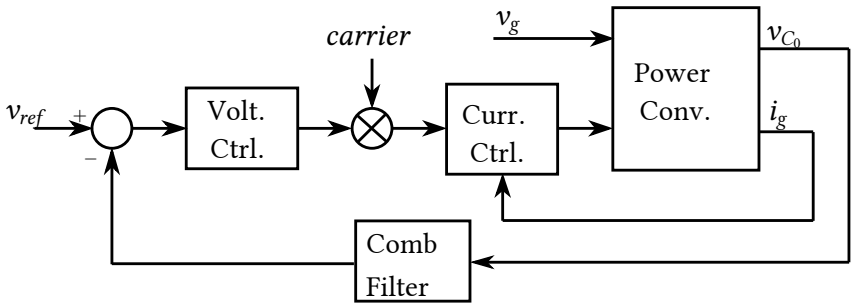

Figure 4.1: Controller block diagram for the single-phase VSC.

Since both topologies are almost the same from a control perspective, so they are their controllers. The only differences in the three-phase with respect to the single-phase control are: the $\alpha\beta$ transformation[1] and that there are two decoupled current loops working in parallel instead of only one. Therefore, all the controller elements discussed in the next subsections will be common to both architectures.

[1]The only change produced by this linear transformation is the gain of the transfer function.

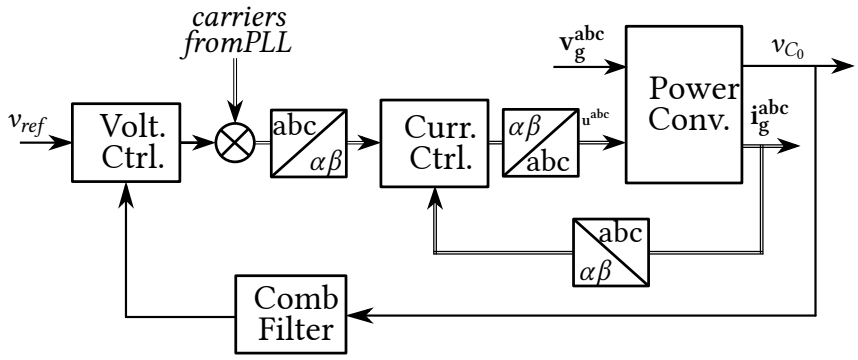

Figure 4.2: Controller block diagram for the three-phase VSC. Double line path means vector variable.

4.2.1 Current Control Loop

The inner control loop (depicted in Fig. 4.3) has three parts: the stabilisation controller $K(z)$, the feed-forward filter $F(z)$ and the resonators bank $R(z)$ (with a proportional and an integral path).

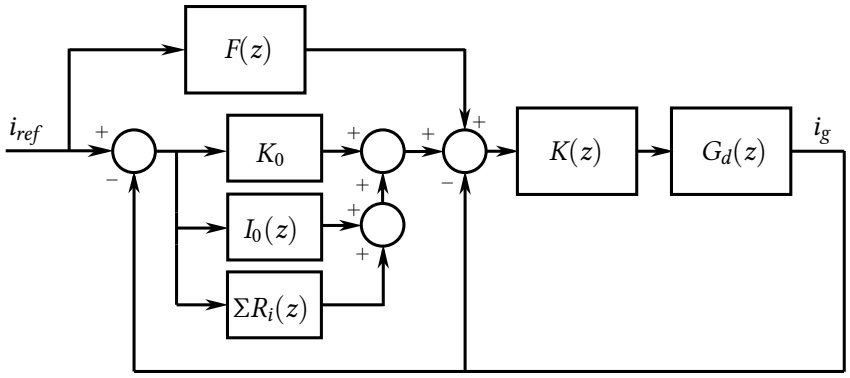

Figure 4.3: Current controller block diagram.

Before starting the controller design, it is important to make sure that the currents flowing into the DC bus $\mathbf{i}_f$ at $t = 0$ are null (or small) to avoid big inrush currents at the converter start-up. This can be obtained by performing the simple variable change

$$\mathbf{w}^{\alpha\beta} = \mathbf{v}_g^{\alpha\beta} - v_{c_0}\mathbf{u}^{\alpha\beta}$$

.

Because $\mathbf{v}_c^{\alpha\beta} \approx \mathbf{v}_g^{\alpha\beta}$ (since the LCL filter input impedance is small) and the effect of parasitic resistive elements is negligible, at $t = 0$, $\mathbf{i}_f^{\alpha\beta}(0) \approx \mathbf{0}$ if $\mathbf{w}^{\alpha\beta}(0) = \mathbf{0}$.

4.2.1.1 Stabilisation Controller

The stabilisation controller $K(z)$ is a low-order controller which presents the fastest dynamics with respect to the other control loops. The aim of this inner loop is to modify the original open-loop transfer function $G_d(z)$ so that:

- The resonant peak produced by the LCL filter is reduced.
- High frequencies are attenuated as much as possible.
- The gain of the closed-loop transfer function at the grid frequency is close to 1 and the phase close to 0 (to track the current references and reject the disturbances at its best).

These objectives can be obtained by choosing an appropriate structure for $K(z)$, for example, a low-pass filter $k\frac{z}{z-a}$, with $k > 0$ and $-1 < a < 1$. Note that this extra loop can be seen as a loop-shaping technique to help maximising the controller robustness and reducing the control effort of the other controllers.

In order to quantify the effect of this controller, let's start by the discrete-time equation (in the z-domain) that relates the control actions with the grid current

$$i(z) = G_d(z)w(z) + G_{v_g}(z),$$

where $G_d(z)$ is the third-order discrete-time transfer function[2] with respect to the control signal $w(z)$, and the term $G_{v_g}(z)$ is related to the input admittance of the LCL filter and represents the loop disturbance.

The closed loop equation in the z-domain, involving the controller $K(z)$, can be written as $i(z) = G'_d(z)i_r(z) + G'_{v_g}(z)$, where $i_r(z)$ is the current reference, $G'_d(z)$ is the closed-loop transfer function[3] $\frac{G_dK}{1+G_dK}$ and $G'_{v_g}(z)$ is the closed-loop transfer function $\frac{1}{1+G_dK}G_{v_g}$.

Observe that if $G'_d(z)$ tends to 1, $G'_{v_g}(z)$ tends to 0 since $\frac{G_dK}{1+G_dK} + \frac{1}{1+G_dK} = 1, \forall\omega$. Therefore, at the grid frequency (50 Hz) the first term should be close to 1 in order to follow correctly $i_r(z)$ and minimise $G_{v_g}(z)$. On the other hand, for robustness reasons, the closed-loop transfer function should have low gain at higher frequencies.

4.2.1.2 Resonators bank

All the resonators are placed in parallel and each one is tuned to a different frequency ω_k. Besides a resonator at the grid fundamental frequency, it is not necessary to place a resonator in every harmonic: as shown in previous chapters

[2] The relative degree of this transfer function is one due to the apparition of sampling-zeros.
[3] Dependencies on z have been dropped.

the even harmonics are null, and in the three-phase three-wire case there are not multiples of three harmonics either. Therefore, only the $1, 3, 5, 7, 9, \ldots, n^{th}$ harmonics need a resonator in the single-phase VSC and only the $1, 5, 7, 11, 13\ldots, n^{th}$ harmonics need a resonator in the three-phase one.

An integrator can be added in parallel to get rid of the currents average values (this element can be seen as a resonator working at 0 Hz)[4]. And finally, since the dynamics of the resonators is slow, a proportional path K_0 is added in order to let the fast disturbances reach the inner control loop to be rejected as soon as possible. This can be seen as the equivalent of the proportional path in a usual PI controller.

4.2.1.3 Feed-Forward Filter

This element $F(z)$ is another loop-shaping component. It is not strictly necessary, but it reduces the resonators control effort. If the plant transfer function $G'_d(z)$ was perfectly known, the ideal $F(z)$ would be its inversion, i.e. $F(z) = \frac{1}{G'_d(z)}$. This way, the resonators would not have to work and would not be necessary.

In reality, is not possible to know perfectly $G'_d(z)$ and its inverse would be a non-causal transfer function. Therefore, $F(z)$ can be chosen to be a causal transfer function (e.g. a low-pass filter structure or simply a constant) so its frequency response is similar to $\frac{1}{G'_d(z)}$ at the fundamental frequency (50 Hz).

4.2.2 Voltage Control Loop

4.2.2.1 Voltage Controller

The main function of this loop is to balance the active power of the whole system, finding the right value for the grid currents amplitude to keep the DC bus voltage average value constant. To do so, the input to this controller is the difference between the DC bus voltage reference and the mean value of the DC bus voltage $\overline{v_{c_0}}$.

This amplitude is then multiplied by the carriers from the PLL, becoming a grid-synchronised reference for the current controller. This reference would give a unity-power-factor operation. Reactive power can be generated just by adding a sinusoidal signal of arbitrary amplitude and phase of $\frac{\pi}{2}$ with respect to the original reference. The apparent power will have an inductive component if this amplitude is positive, and it will have a capacitive component otherwise.

[4]Obviously, adding an integrator at this loop implies that current sensors has been properly calibrated to avoid DC offsets. Moreover, feedback signals have been low-pass filtered to avoid discrete-time DC components due to the aliasing phenomenon in the time-domain sampling operation at the AD converters.

Because the voltage loop is performing a regulation, the structure for this controller is chosen to be a discrete-time proportional-integral controller, which can be designed from a high level point of view. Supposing that the converter is in steady-state and vc_0 is a constant value V_{C_0}, an active power balance can be done from (2.5). Then, the last equation from (2.1) can be rewritten using a new variable $\tilde{v}_{C_0}$ as

$$C_0 \frac{d}{dt}\tilde{v}_{C_0} = -\frac{\tilde{v}_{C_0}}{R} + \frac{1}{2}\frac{V}{V_{C_0}} I.$$

From this point, it is easy to obtain the transfer function

$$\frac{\tilde{v}_{C_0}(s)}{I(s)} = \frac{k}{RC_0 s + 1},$$

where $k = \frac{RV}{2V_{C_0}}$. Once it is discretised following (2.20), the PI controller $C(z)$ can be designed by means of any usual synthesis method.

Finally, it is important to remark that when the converter works as an inverter, this voltage loop is not necessary and needs to be opened: the DC bus voltage is imposed externally and the reference will be directly the amplitudes and phases of the desired grid currents.

4.2.2.2 Comb Filter

In the single-phase VSC, the steady-sate DC bus voltage v_{c_0} will present oscillations at twice the mains frequency. And even if in the three-phase case, this value should be constant, it may present oscillations if working conditions are not ideal (e.g. if grid voltages are not balanced). So, a FIR comb filter has been added in the feedback path of the voltage control loop in order to extract the DC bus voltage average value.

The z-domain transfer function of the N order comb filter is $\frac{\overline{v_{C_0}}(z)}{v_{C_0}(z)} = \frac{1}{N}\frac{1-z^{-N}}{1-z^{-1}}$ (Proakis and Manolakis, 1988). The bode plot of a comb filter is depicted in Fig. 4.4.

It is important to remark that the steady-state value is reached after only NT seconds, rejecting completely all the harmonics. This kind of filters can only be carried out in the discrete-time domain, and there is not an equivalent of a comb filter in continuous time.

The length N of the filter is designed to reject periodic signals with fundamental period equal to the grid period. It uses the information from the PLL in order to follow the frequency variations and it is implemented with an approximation of a fractional delay computation, so it can work when the sampling frequency is not an integer multiple of the mains fundamental frequency.

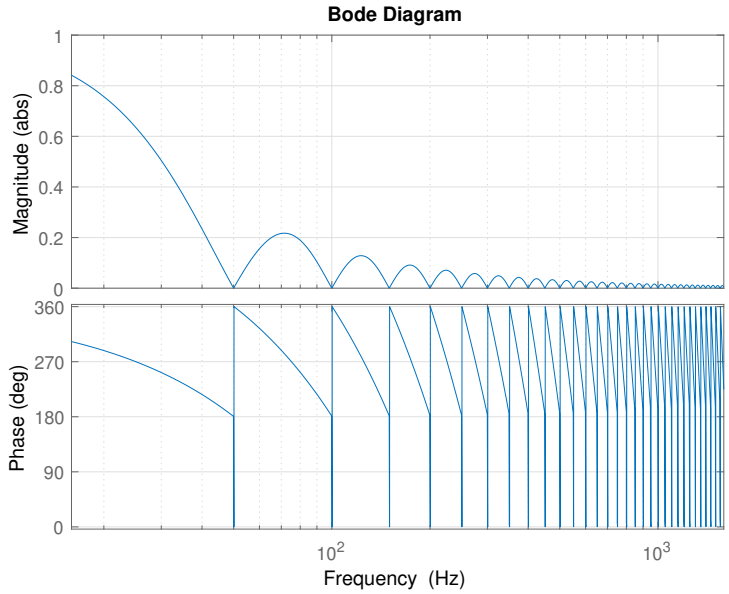

Figure 4.4: Bode diagram of a comb filter.

4.2.2.3 Current Control Loop Resonators Reset

In order to give a fast controller response when a disturbance occurs (more precisely, when the load decreases instantaneously), all the resonators are set to zero if the DC bus voltage reaches a pre-fixed value greater than the reference. This action reduces drastically the gird currents and therefore, the DC bus voltage will decrease as well. The reset is implemented by means of a hysteresis to avoid multiple resets due to any noises in the measurement.

Furthermore, since the resonators reset clears all the integration performed until the load transient, the currents reach the new steady state very quickly. The resonators dynamics is slow and they work really well in steady state, but they can take some time to reach a new steady state when a disturbance occurs.

Thus, the DC bus voltage during the load transient will always be under a pre-fixed maximum value and it will return to its reference value faster. Moreover, just after the transient, the grid currents will not present high frequency harmonics since all the resonators are empty.

4.2.2.4 Load Current Feed-Forward

It has been explained how the outer voltage controller performs a power balance of the converter. When a change in the load occurs, in order to make the response time virtually instantaneous, a feed-forward path from the load current i_{load} can been added to this control loop.

The idea is to include into the computations not only the information from the DC bus voltage v_{C_o}, but also from the load current. Therefore, since the phase-to-neutral voltages, the DC bus voltage and the load current are measured, an ideal power balance can be performed to obtain the necessary grid current references. This way, the voltage PI controller will only have to finely adjust this value in order to compensate the losses from parasitic elements and other possible modelling errors. Fig. 4.5 shows the block diagram of this new element in the voltage control loop.

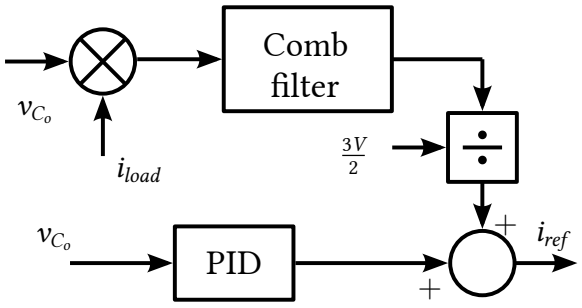

Figure 4.5: Diagram for the load current feed-forward.

First, the measured DC bus voltage and the load current are multiplied and filtered using a FIR comb filter (the same type as the one placed at the voltage controller feedback path) to compute the average value of the active power drained by the load. Then, this power output is divided by $\frac{3}{2}$ of the phase-to-neutral voltages RMS value to obtain the necessary line current references fulfilling the active power balance.

The advantages of this element are clear: the voltage controller only has to compensate the small error produced by the feed-forward loop estimation. Nevertheless, it implies the use an extra current transducer and some extra computations. It is important to remark that this compensation system has been added to improve the dynamical response against load variations, but it is not strictly necessary.

4.2.3 Choosing the Sampling Period

Many factors must be taken into account when choosing the controller sampling period, like the desired bandwidth, the converter switching frequency or the computation time.

Ideally, and according to the Shannon sampling theorem, the maximum dynamic frequency to be controlled must be half of the sampling frequency (in reality, this is too optimistic since the gain at high frequencies is generally small). On the other hand, in a power converter, the maximum useful sampling frequency is twice

the switching frequency: deciding independently when to close and open a switch every switching period.

Special attention should be paid if the sampling frequency is an integer multiple (or submultiple) of the switching frequency, since there will be aliasing in the measurements. This problem can be addressed by using anti-aliasing filters.

Obviously, the main limitation when choosing this control period is the computation time. However, with all the technological advances being made on the micro-processors technology (like floating point hardware units, control law accelerators, etc.), it is possible to reach very short times.

4.2.4 Phase-Locked Loop and Carriers Computation

As mentioned in the introduction of this section, the phase-locked loop is a synchronous reference frame PLL with a Moving Average Filter (SRL-PLL MAF) (Golestan et al., 2014). It uses the same comb filter described in this chapter to improve the harmonic rejection and dynamic response. The output is a sine-wave of amplitude 1 synchronised in phase and frequency to the phase-to-neutral voltage (or voltages in the case of the three-phase VSC).

Every resonator needs four carriers (i.e., $\cos(n\omega t)$, $\cos(n\omega t + \varphi_k)$, $\sin(n\omega t)$ and $\sin(n\omega t + \varphi_k)$) that are generated from the PLL output, that is, $\sin(\omega t)$ and $\cos(\omega t)$. It is easy to show that the resonators carriers do not need to have the same angle as the line-to-neutral voltage that they are intended to control: the important parameters are the angles φ_k. This simplifies the computations since the same carriers can be used across all the phases.

It is possible to obtain all the carriers from the original PLL signals by the means of a recursive algorithm. The first step is to realise that both $\cos(n\omega t + \varphi_k)$ and $\sin(n\omega t + \varphi_k)$ can be split in products and sums using trigonometrical identities

$$\begin{aligned}\cos(n\omega t + \varphi_k) &= \cos(n\omega t)\cos(\varphi_k) - \sin(n\omega t)\sin(\varphi_k)\\ \sin(n\omega t + \varphi_k) &= \sin(n\omega t)\cos(\varphi_k) + \cos(n\omega t)\sin(\varphi_k).\end{aligned}$$

Note that since the φ_k values are constants, $\cos(\varphi_k)$ and $\sin(\varphi_k)$ are constant values as well. Finally, using the same trigonometrical properties as before, $\cos(n\omega t)$ and $\sin(n\omega t)$ can be written as

$$\begin{aligned}\cos((n-1)\omega t + \omega t) &= \cos((n-1)\omega t)\cos(\omega t) - \sin((n-1)\omega t)\sin(\omega t)\\ \sin((n-1)\omega t + \omega t) &= \sin((n-1)\omega t)\cos(\omega t) + \cos((n-1)\omega t)\sin(\omega t).\end{aligned}$$

Therefore, it is possible to compute all the carriers from the original signals

$\sin(\omega t)$ and $\cos(\omega t)$. For example, $\cos(3\omega t + \varphi_k)$ can be computed like this

$$\begin{aligned}
\cos(2\omega t) &= \cos(\omega t + \omega t) = \cos(\omega t)\cos(\omega t) - \sin(\omega t)\sin(\omega t) \\
\sin(2\omega t) &= \sin(\omega t + \omega t) = \sin(\omega t)\cos(\omega t) + \cos(\omega t)\sin(\omega t) \\
\cos(3\omega t) &= \cos(2\omega t + \omega t) = \cos(2\omega t)\cos(\omega t) - \sin(2\omega t)\sin(\omega t) \\
\sin(3\omega t) &= \sin(2\omega t + \omega t) = \sin(2\omega t)\cos(\omega t) + \cos(2\omega t)\sin(\omega t) \\
\cos(3\omega t + \varphi_k) &= \cos(3\omega t)\cos(\varphi_k) - \sin(3\omega t)\sin(\varphi_k)
\end{aligned}$$

Observe that it is also possible to save computation time if there is not a resonator for every harmonic. For example, the carriers for the $n = 5$ resonator can be computed with the $n = 2$ and $n = 3$ resonators carriers, with no need for the $n = 4$ resonator computation.

4.3 Single-Phase VSC Controller Design

In order to design the single-phase full-bridge VSC controller, the physical values of the plant shown in Table 4.1 are going to be considered and Table 4.2 lists the nominal input and output values. Following the reasoning from earlier in this chapter, the sampling period for this controller has been chosen to be be $T = 50\,\mu s$ since:

- As it will be detailed in the next chapter, the switching frequency for the converter will be 20 kHz (mostly defined by the power elements).

- The DSP computation time can be optimized to take around 45 µs, therefore 50 µs was chosen to give an extra margin.

In this application, there is another important constraint regarding the sampling time: the LCL filter resonance frequency needs to be above the maximum bandwidth of the controller (to avoid unnecessary amplification of the control signals), below the Shannon sampling theorem limit (10 kHz, so the controller is able to reduce its effects) and obviously, below the switching frequency (20 kHz) in order to filter all the high frequency spectral content.

Once the sampling frequency is fixed, the easiest way to finely adjust the resonance frequency without modifying the inductors is by changing the capacitor value from the LCL filter.

Table 4.1: Built Voltage Source Converter Parameter Values for Both Single-Phase and Three-Phase VSC.

L_1	540 µH	r_1	0.43 Ω
L_2	184 µH	r_2	0.15 Ω
C	10 µF	C_0	470 µF

Table 4.2: Single-Phase Input and Output Values.

V	$230\sqrt{2}$ V	ω_1	50 Hz
V_{C_0}	400 V	R	83.3 Ω

4.3.1 Current Control Loop

4.3.1.1 Stabilising Controller

For the chosen structure of $K(z) = k\frac{z}{z-a}$, and the plant values listed in Table 4.1, the values for $K(z)$ have been chosen to be $k = 0.3$ and $a = 0.85$. In Fig. 4.6 the bode diagrams of the closed-loop transfer functions $G_d(z)$ and $G'_d(z)$ are depicted.

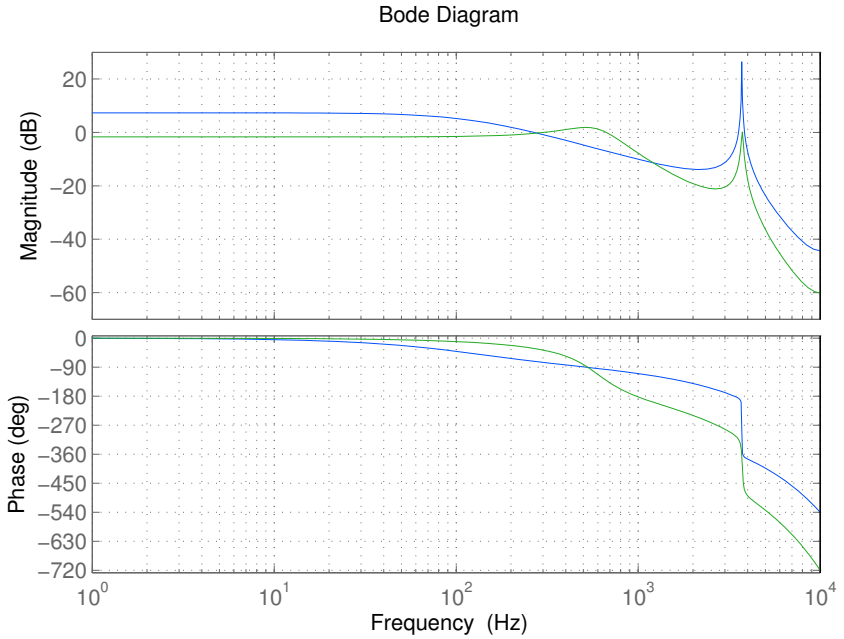

Figure 4.6: Bode diagrams of $G_d(z)$ (blue) and $G'_d(z)$ (green) for the single-phase VSC.

Note the difference between the two bode diagrams and how at 50 Hz, $G'_d(z)$ is close to 1 and the resonance peak is significantly reduced, preventing the LCL filter resonance. The new transfer function $G'_d(z)$ will be seen as the plant to be controlled.

4.3.1.2 Feed-Forward Filter

To compensate the amplitude and phase of the grid current with respect to the sinusoidal references, $F(z)$ has been chosen to be simply a constant k_{inv}, corresponding to the magnitude of $\frac{1}{G_d'(z)}$ at $z = e^{j2\pi 50T}$, that is, $F(z) = k_{inv} = 1.2085$.

4.3.1.3 Resonators

As mentioned earlier, electrical signals are usually symmetrical in such a way that they contain only odd harmonics. Therefore, there is no need to place resonators at even harmonics.

Following the design procedure from the previous chapter, in order to maximise the controller robustness, the resonator angles φ_k must coincide with the phase of the plant at the considered frequency ω_k. Therefore, the poles trajectories of the new closed-loop transfer function $P(z) = \frac{KG_d}{1+KG_d}$ will be perpendicular to the unit circle (Orellana and Griñó, 2013).

On the other hand, in this case, the resonators gains have been chosen empirically according to Table 4.3, decreasing their values as frequency increases since the content of harmonics at high frequencies is smaller. Finally, the integrator $I_0(z)$ will be $5 \cdot 10^{-5} \frac{z}{1-z}$ and the constant K_0 will have a value of 0.1. This will serve as a comparison to the most formalised numerical methods discussed previously.

Table 4.3: Resonators Parameter Values for the Single-Phase Controller.

Res.no.	ω_k (rad/s)	φ_k (rad)	g_k
1	$2\pi 50$	-0.0929	0.025
3	$2\pi 150$	-0.2874	0.008
5	$2\pi 250$	-0.5117	0.005
7	$2\pi 350$	-0.7972	0.002
9	$2\pi 450$	-1.1877	0.001
11	$2\pi 550$	-1.6966	0.0005
13	$2\pi 650$	-2.2130	0.0002
15	$2\pi 750$	-2.6115	0.0001
17	$2\pi 850$	-2.8925	0.00009

Fig. 4.7 shows the open-loop transfer function $L = G_d'\Sigma R_k$. Observe how the gain is infinite and the phase is null at the desired frequencies. Regarding the robustness, as indicated previously, a good indicator is the minimum distance[5] d from the open-

[5]This value is given by the inverse of the sensitivity transfer function infinity norm, $d = \frac{1}{\|S\|_\infty}$, where $S(z) = (1 + L(z))^{-1}$.

loop $L(z)$ Nyquist plot to the critical point -1. In this case, the obtained value is $d = 0.68$, indicating that the design is robust.

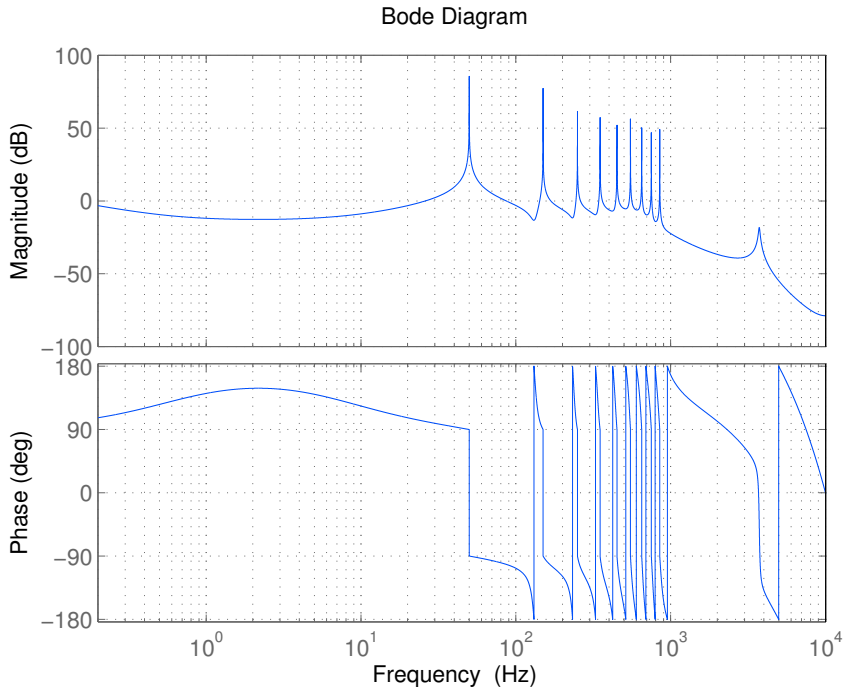

Figure 4.7: Bode diagram of the open-loop transfer function L for the three-phase VSC.

Out of curiosity, Fig. 4.8 depicts a resonator closed-loop pole trajectory when increasing linearly the gain from 0 to its final value. Observe how the trajectory is perpendicular to the unit circle when the gain tends to 0.

4.3.2 Voltage Control Loop

As it can be observed in Fig. 4.1 and 4.2, the voltage control loop structure is the same for both converters. The only difference is the gain variation due to the different DC bus voltage regulation values in both cases.

For the single-phase VSC, the designed proportional-integral compensator that gives the desired dynamic response and that will be implemented is

$$C(z) = 0.504 + 2.507 \cdot 10^{-4} \frac{z}{z-1}.$$

This controller has been obtained by usual design methods.

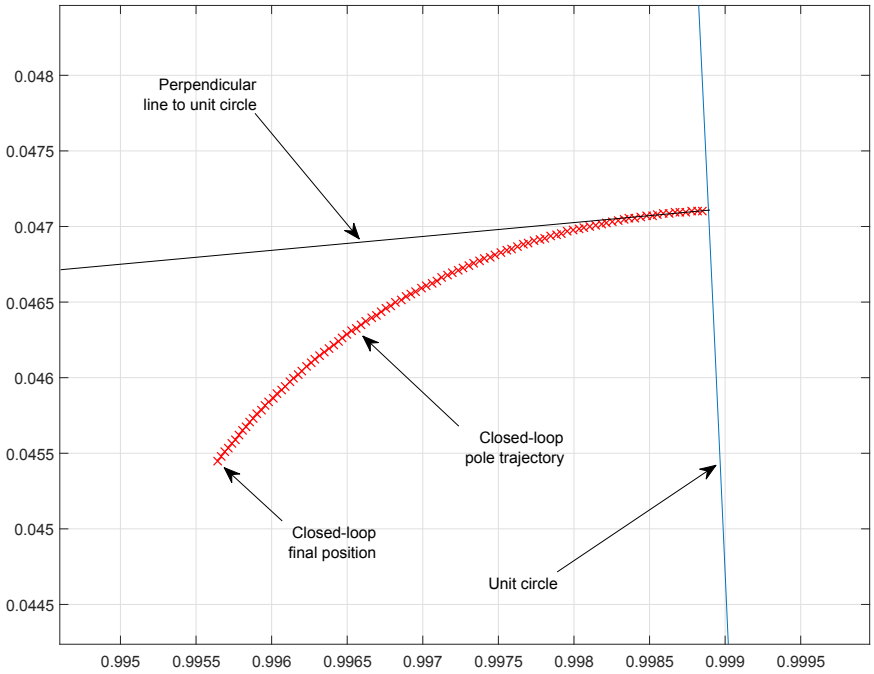

Figure 4.8: Resonator closed-loop pole trajectory.

4.4 Three-Phase VSC Controller Design

For this VSC topology, the physical parameters are the same than in the previous section listed in Table 4.1, and Table 4.4 lists the nominal input and output values. The sampling period for this controller will be again $T = 50\,\mu s$ following the same reasons from the previous application.

Table 4.4: Three-Phase Input and Output Values.

V	$230\sqrt{2}\,V$	ω_1	$50\,Hz$
V_{C_0}	$800\,V$	R	$83.3\,\Omega$

4.4.1 Current Control Loop

4.4.1.1 Stabilisation Controller

For the chosen structure of $K(z) = k\frac{z}{z-a}$, and the values of the plant listed in Table 4.1, the selected values for $K(z)$ are $k = 0.074$ and $a = 0.92$. In Fig. 4.9 the bode diagrams of the closed-loop transfer functions $G_d(z)$ and $G'_d(z)$ are depicted.

Exactly as happens in the previous section, $G'_d(z)$ is close to 1 at $50\,Hz$ and the resonance peak is reduced.

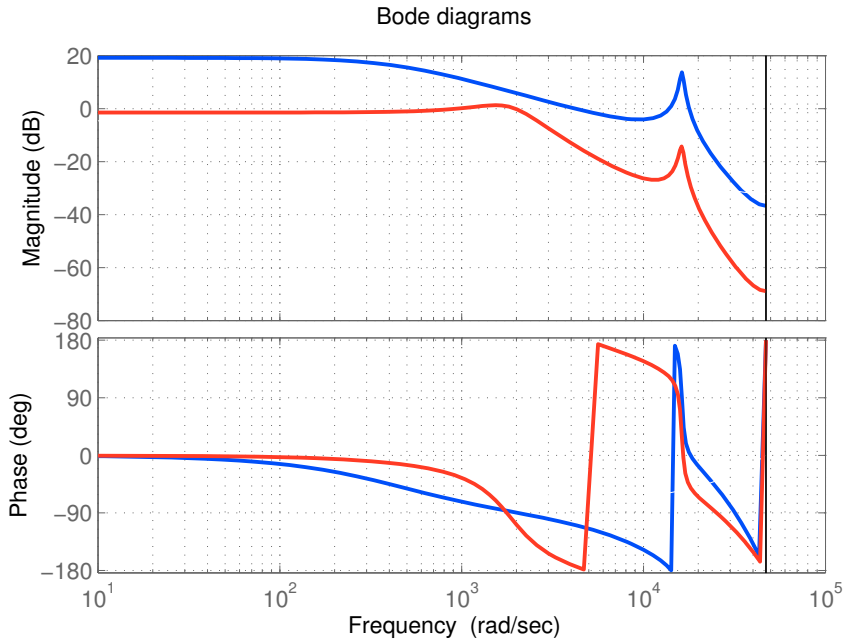

Figure 4.9: Bode diagrams of $G_d(z)$ (blue) and $G'_d(z)$ (red). for the three-phase-phase VSC.

4.4.1.2 Feed-Forward Filter

Analogously to the single-phase VSC, $F(z)$ will be a constant value as well, corresponding to the magnitude of $\frac{1}{G'_d(e^{j2\pi 50})}$. In this case, $F(z) = k_{inv} = 1.0396$.

4.4.1.3 Resonators Bank

For the three-phase VSC, resonators are only needed at odd frequencies which are not multiple of three, as justified earlier. The angles φ_k have been chosen as usual, following the design rule of small gains to maximise the controller robustness.

On the other hand, the gains g_k have been determined by the HIFOOD numerical system discussed in the previous chapter. In the Appendix B there is an example of code using HIFOO explaining how to tune these gains. The constant K_0 value has also been determined numerically giving a proportional path of $K_0 = 0.615$. Table 4.5 contains the tuning values of all resonators.

Note that in this case, there are two current controllers working in parallel. This means that there are 14 resonators in total. Fig. 4.10 shows the open-loop bode diagram for the three-phase VSC.

The infinity norm of the sensitivity transfer function $\|\frac{1}{1+L}\|_\infty$ indicates that the minimum distance from the open-loop Nyquist plot to the critical point is $d = 0.608$. Therefore, it can be concluded that the controller is robust.

Table 4.5: Resonators Parameter Values for the Three-Phase Converter.

Res.no.	$\omega_k\,(\mathrm{rad/s})$	$\varphi_k\,(\mathrm{rad})$	g_k
1	$2\pi 50$	-0.2328	0.0154
5	$2\pi 250$	-0.7601	0.0119
7	$2\pi 350$	-1.9420	0.0149
11	$2\pi 550$	-2.5537	0.0119
13	$2\pi 650$	-2.7221	0.0136
17	$2\pi 850$	-2.9512	0.0115
19	$2\pi 950$	-3.0370	0.0059

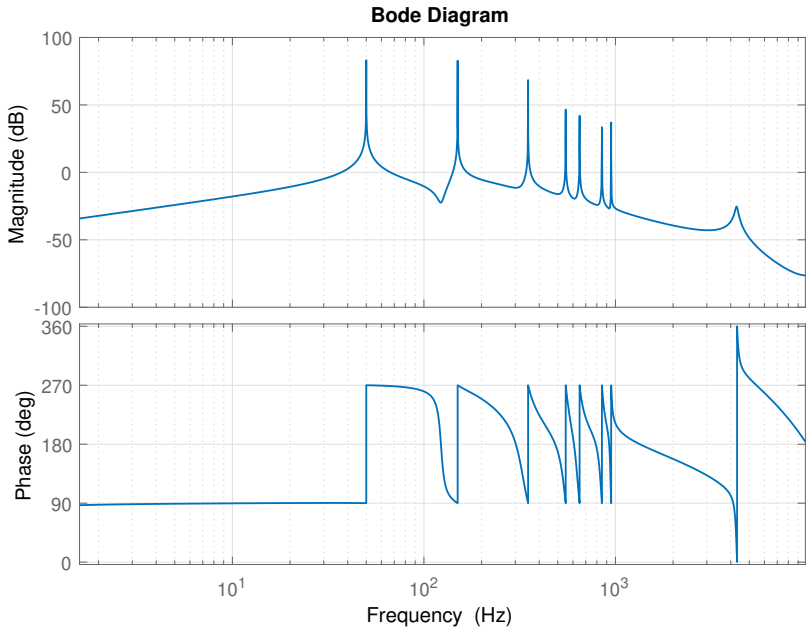

Figure 4.10: $G_d'\Sigma R_k$ open-loop bode diagram for the three-phase VSC.

4.4.2 Voltage Control Loop

The design of this proportional-integral controller is carried out exactly as in the single-phase case. The only difference is the gain variation since the DC bus voltage value regulation is different, 800 V instead of 400 V. The resulting voltage controller giving the desired dynamic response and that will be implemented is

$$C(z) = 0.9 + 1.75 \cdot 10^{-3} \frac{z}{z-1}.$$

It is worth recalling that this controller is only necessary during rectification op-

eration. When the converter is used as an inverter, this loop needs to be opened and the references will be directly the respective grid currents amplitudes and angles for each phase.

4.5 Simulation Results

Some simulations have been performed to validate the theoretical results before the controller implementation. They correspond to the three-phase three-wire VSC since it is the most complete controller (it has two independent single-phase controllers running in parallel) and it is possible to simulate, for example, grid unbalances.

4.5.1 Pre-Charge and Start-Up

As shown in Fig. 4.11, a pre-charge system carried out by a uncontrolled rectifier takes the converter to an equilibrium point, close to the operation one, in order to minimise the inrush currents. This equilibrium point corresponds to[6] $\frac{3\sqrt{3}}{\pi}V \approx 538\,\text{V}$. In practice, the pre-load is carried out by means of a power resistor that will charge the DC bus through the semiconductor parasitic diodes. Once the bus is charged, the resistor is short-circuited by a relay or a mosfet.

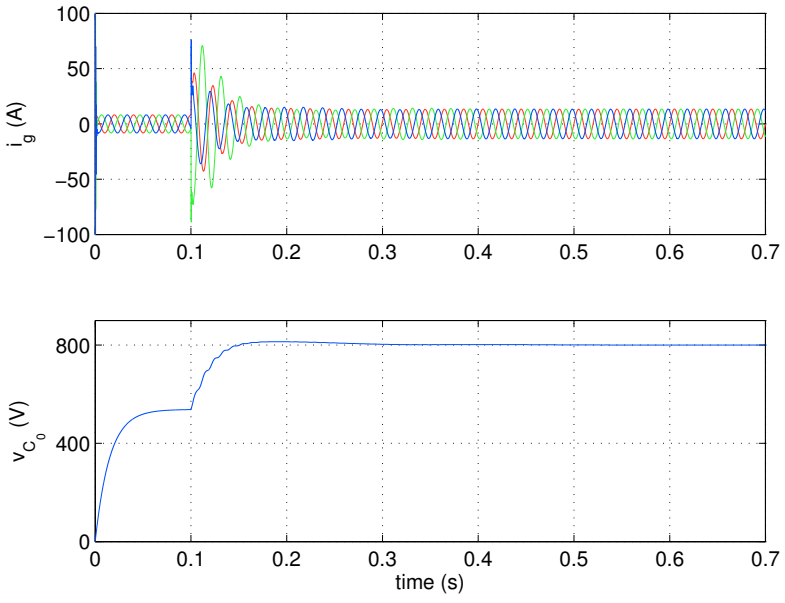

Figure 4.11: Start-up in normal working conditions. Evolution of $\mathbf{i}_g$ and v_{c_0}.

The first transient (very fast, 1 ms, almost not noticeable in the figure) corresponds to the line currents starting to flow into the three inductors L_2 and capacit-

[6] This corresponds to the output voltage average value in an uncontrolled rectifier.

ors C branches from the LCL filter. It is a high current transient, but it is fast and presents a low energy. Immediately after, the DC bus is charged trough the power resistor during 0.1 s.

Finally, the controller is turned on, taking DC bus voltage to the desired value $v_{c_0} = 800\,\text{V}$. In single-phase or three-phase four-wires converters, it is usual to start the controller during the grid voltages zero-crossing to avoid big transients. In this case, it is not possible since all the phases need to start at the same time and when one phase is 0, the other two are apart 120 deg.

4.5.2 Grid Impedance Disturbances

Fig. 4.12 shows the operation of the power converter under a big grid impedance variation. Observe that when the grid impedance increases instantaneously, the system remains stable and reaches the steady state in few grid periods.

The grid inductance L_g varies from 0 µH to 500 µH. This is not a realistic test, but it shows the controller robustness.

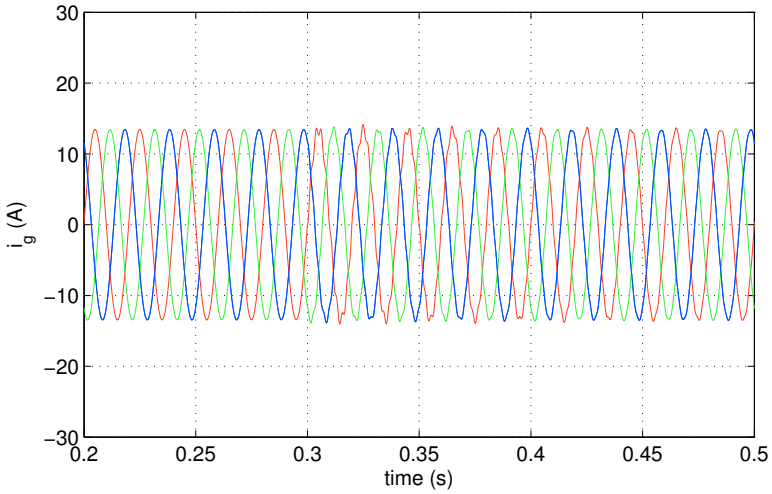

Figure 4.12: Behaviour of $\mathbf{i_g}$ when a change on the grid inductance L_g from 0 µH to 500 µH occurs at $t = 0.3\,\text{s}$.

It is not represented in the figure, but the voltage at the connection point changes as well when the grid impedance does. This behaviour, as discussed previously, is due to the uncontrolled loop created by this element: the more current is flowing, the more voltage is produced across the grid impedance, modifying the voltage at the connection point.

4.5.3 Load Variations

In Fig. 4.13, a load variation is shown from 2 kW to 20 kW ($R = 320\,\Omega$ to $R = 32\,\Omega$) and vice-versa.

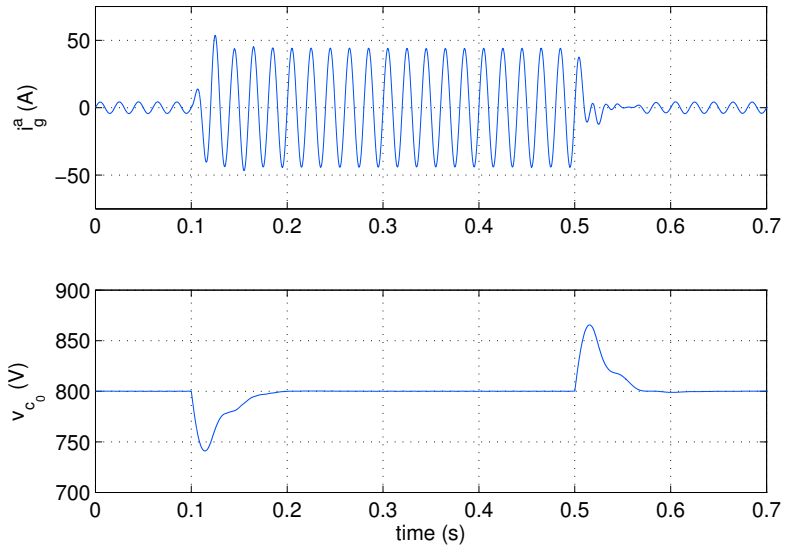

Figure 4.13: Response of i_g^a and v_{c_0} when the load varies from $R = 320\,\Omega$ to $R = 32\,\Omega$ at $t = 0.1\,\text{s}$ and vice-versa at $t = 0.5\,\text{s}$.

Observe how the steady-state is achieved quickly in both transitions. Also, the overshoot and undershoot during the transients are approximately about a 10% of the nominal value.

This simulation did not include any of the techniques described before to improve the dynamic response (like the resonators reset or the load current feedforward compensation), showing that the controller does not need them to get a good performance.

4.5.4 Grid Unbalances

Finally, Fig. 4.14 shows a sag in the grid voltage between the two phases b and c (v_g^b). Observe that when the sag occurs, the line currents $\mathbf{i}_g$ increase in order to keep the active power balance.

It is important to remark that, as predicted, the DC bus voltage v_{c_0} is not constant any more and it oscillates around the reference value. This behaviour justifies the use of the FIR comb filter in the voltage control loop feedback path. The amplitude of these oscillations can be predicted by the mathematical model obtained in Chapter 2, even when a phase is completely missing.

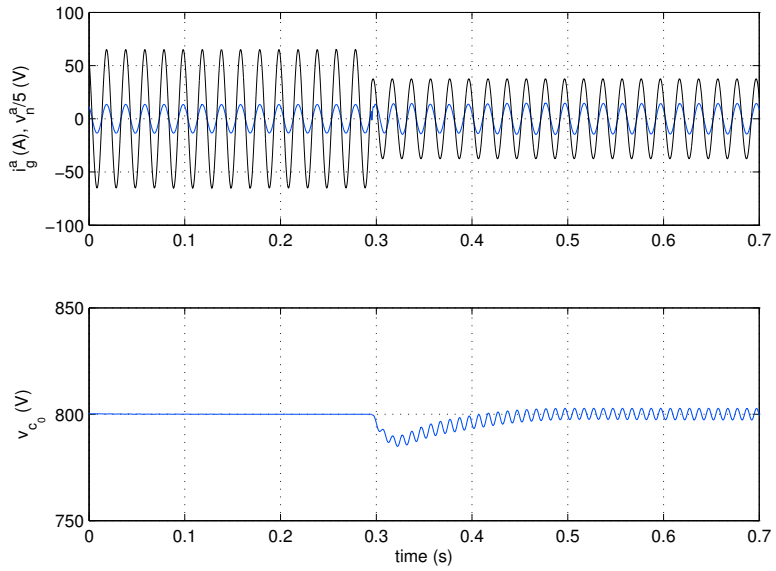

Figure 4.14: Response of i_g^a and v_{c_0} when a sag in $v_g^{b'}$ of a 33.33% of the nominal value happens at $t = 0.3$ s. The measured line-to-neutral voltage v_n^a is depicted with scale 1:5.

Besides this ripple effect, the bus decreases initially (since one phase presents a sag), but recovers in around 100 ms. Also, note that the phase-to-neutral voltage v_n^a is always in phase with the corresponding line current i_g^a, giving a unity-power-factor operation.

"Le savant n'est pas l'homme qui fournit de vraies réponses ; c'est celui qui pose les vraies questions."

-Claude Lévi-Strauss

5

Implementation and Experimental Results

5.1 Introduction

In order to validate all the theoretical results and the simulations, a single- and three-phase voltage source converters have been built and a set of experiments have been carried out. This is by far the most complicated part in this thesis for three main reasons. First, because it is necessary to build all the power hardware (especially inductors), implement drivers for the semiconductors and develop the signals acquisition and control cards. Second, because the designed digital controller has to be implemented into a DSP, so all the operations to be executed by the processor need to be properly coded. And third, because one must deal with a full range of multidisciplinary issues like: electromagnetic compatibility (EMC), common-mode voltages, grounding, thermal dissipation, etc. Despite the importance of these topics in the power supplies industry, they remain undiscussed in this thesis as they are self contained topics in their own right.

5.2 Plant Characteristics & Experimental Setup

From the electrical diagrams shown in Chapter 2, both power converters addressed in this thesis have a very similar hardware. Therefore, a main plant has been conceived so the the single-phase full-bridge VSC can be obtained from the three-phase three-wire VSC by changing a few connections and the DSP firmware. This already shows the versatility of a digital controller in real applications, being able to completely change the behaviour of a same plant by only replacing the firmware on the processor.

Fig. 5.1 shows the plant built for this research, which is composed by:

- A linear programmable three-phase voltage source 360-AMX from Pacific, able to perform all kind of grid disturbances (unbalances, sags, swells, voltage harmonics, ringings, etc.). The nominal working conditions are: phase-to-neutral voltages 230 V, 50 Hz (one phase or three phases).
- The inductive bank, which is a three-phase series connection of inductances placed between the voltage source and the power converter in order to simulate a weak grid. The values of the equivalent inductance goes from 10 µH up to 4.1 mH.
- The power board: a module of three 80 A and 1200 V half bridges of IGBTs connected in parallel (with reference VS-40MT120UHAPbF from Vishay Semiconductors), mounted on an aluminium heat sink.
- A TMS320F28335 floating point DSP from Texas Instruments™ (Texas Instruments, 2016) in a development board.

- The acquisition and conditioning signals circuit for the grid and bus currents and voltages. The signals are low-pass filtered to remove the aliasing and scaled to fit into the dynamic range of the DSP analogue-to-digital converters (ADCs).
- Three double-channel isolated drivers. They receive the control signals computed by the DSP and drive the IGBT gates.
- The resistive load made of a parallel connection of three power 250 Ω resistances.
- For the inverter operation, two 600 V TDK-Lambda Genesys 600-17 DC power supplies in series are connected to the DC bus of the converter to get 800 V.
- Finally, for the inverter operation as well, a set of three transformers connected between the mains and the LCL filter to obtain a good isolation at high frequencies.

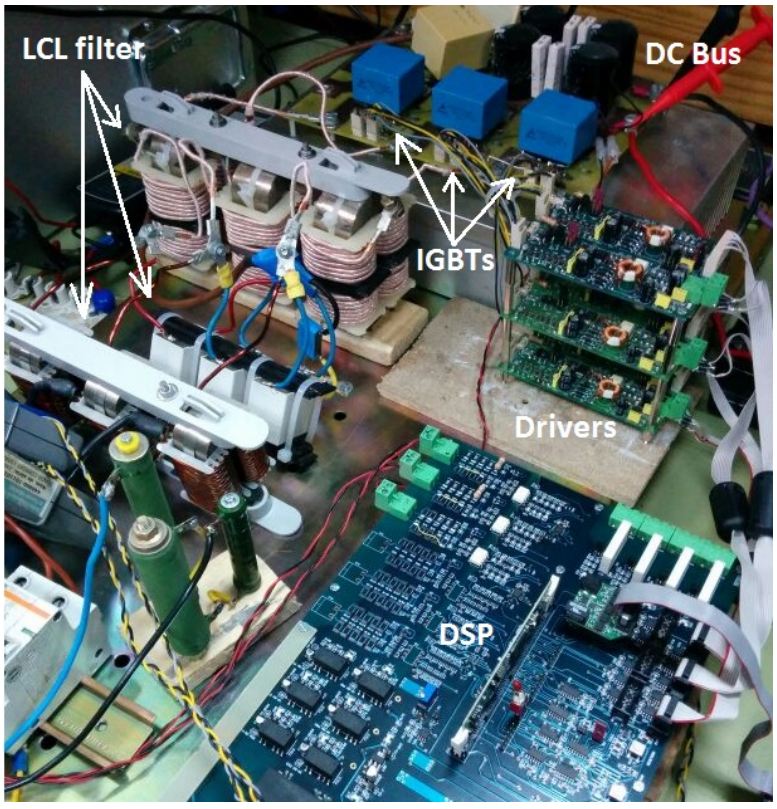

Figure 5.1: Picture of the power hardware, drivers, signal acquisition and DSP card.

As mentioned in the previous chapter, the DC bus voltage will be regulated to 400 V for the single-phase VSC and to 800 V for the three-phase one. Table 4.1 shows the physical values of the plant.

5.2.1 Switching Frequency and Sampling Period

The hardware has been conceived for a switching frequency of 20 kHz. Regarding the pulse-width modulation, all the control signals are modulated using uniform centred pulse single-update PWM. A dead time of 2.0 µs has been found as the shortest time to avoid short-circuits during the IGBT switching in the same leg in any load condition.

The choice of the sampling period for the controller is a very interesting topic, directly related to its bandwidth. For an averaged controlled switched power supply, it does not make any sense to set the controller sampling at more of twice the switching frequency. In this thesis, the sampling rate is set to be the same as the switching frequency, so the PWM is updated every period. This can create some aliasing problems which are carefully addressed by the use of low-pass filters.

5.2.2 Signal Conditioning System

5.2.2.1 Voltages Conditioning

All the voltages and currents measured from the plant need to be adapted to the DSP ADC. The complete chain for the voltage measuring is:

1. Voltage scaling and noise filtering. A resistor divider reduces the high-voltage measurements to low-level voltages so they can be handled by the rest of the analogue conditioning chain. The resistor divider gain is determined if function of the maximum voltage to be measured. Also, a passive RC filter will attenuate the high-frequency noises present in the signal to be measured.

2. Isolation. The DSP is isolated from the converter. Therefore, a linear optocoupler ACPL-790B-000E is used and its secondary side is grounded to the isolated DSP ground (Avago Technologies, 2016a).

3. Anti-aliasing filtering and final scaling adjustment. Since the measurements are taken at the same rate than the switching frequency (20 kHz), an aliasing in form of a DC value is expected in the measurements. To avoid this problem, an active low-pass filter (implemented by a differential operational amplifier) has been added to attenuate the higher frequencies[1], and to adjust the voltage levels to the 3.3 V ADC full scale voltage. If the measure is AC, an offset of 1.5 V is introduced to be able to read negative voltages.

[1] In discrete time, any frequency above $\frac{f_s}{2}$, where f_s is the sampling frequency, will be aliased as a lower frequency component. In particular, a discrete-time sinusoidal signal of f_o frequency $''A\sin(2\pi f_o \frac{n}{f_s} + \theta)''$ where the sampling frequency f_s is equal to f_o, will be aliased as the DC value $A\sin(\theta)$, $\forall n \in \mathbb{Z}$. To minimize these effects, the low-pass filter implemented in this application attenuates all frequency components from approximately 5 kHz. The filter is first order and has a static gain of 1.

5.2.2.2 Currents Conditioning

The currents measuring chain is very similar to the voltages one. The only difference is that the measured currents (given by Hall effect sensors) are already isolated:

1. Current scaling and noise filtering. For the same current, the LM-100 sensors give a proportional voltage to the output resistor value, which must be chosen to adjust the dynamic range (LEM, 2016). Then, a passive RC filter will attenuate the high-frequency noises present in the current signal to be measured.

2. Anti-aliasing filtering and final scaling adjustment. The output sensor voltage signal is already isolated, so it can directly be low-pass filtered to avoid aliasing and adjusted to the 3.3 V ADC full scale voltage level.

To protect the ADC from negative or over voltages in both cases, two diodes (one to 3.3 V and another one to the ground) have been added just at the ADC input. Finally, an RC filter placed just at the ADC input will attenuate noises and the capacitor will give the necessary peak current during the measurement operation.

5.2.3 Drivers

The drivers developed at the Control Laboratory can be configured so they can be used for different applications and with different semiconductors technologies (Si, SiC): they are dual (there are two drivers per module) and each output voltage can be positive or negative, they have an enable and a reset signal, a hardware protection to avoid both channels to be switched on at the same time (to prevent short-circuits), an output hardware protection to avoid damage to propagate backwards (transil, fuse and diodes), and a configurable threshold voltage to trigger the driver saturation signal. This threshold voltage is defined by changing a number of diodes in series connected to the desaturation detection pin from the driver IC (Avago Technologies, 2016b).

5.2.4 Digital Signal Processor

The controller has been implemented in the TMS320F28335 controlCARD from Texas Instruments™ (Texas Instruments, 2010). In this card for evaluation and development, a TMS320F28335 DSP is included in a board with a DIMM100 connector that can be plugged directly into the acquisition signals card. Programming and real-time debugging are possible thanks to a JTAG probe.

The internal clock frequency of this DSP is 150 MHz and the floating point unit executes a complete operation in two clock cycles, that is, at a frequency of 75 MHz.

5.2.5 Other Important Features

5.2.5.1 Dealing with Common-Mode Voltage

Active front-end converters like the three-phase three-wire converter present common mode voltage issues since the DC bus voltage moves with respect the input ground due to the switching. The drivers need to follow these fast voltage changes and may have problems to properly switch the IGBTs. In order to reduce those effects, the filter proposed in (Acharya and John, 2010) has been implemented.

As shown in Fig. 5.2, this filter consists on two capacitors of 2 µF in series, and connected in parallel to the DC bus capacitor. Then, the midpoint is connected to the common node of the LCL filter capacitors. Finally, this common node is connected to the ground by means of a 0.022 µF capacitor. This results in a transformation of the common-mode voltage into a common-mode current flowing through the cable joining the DC bus and the LCL filter.

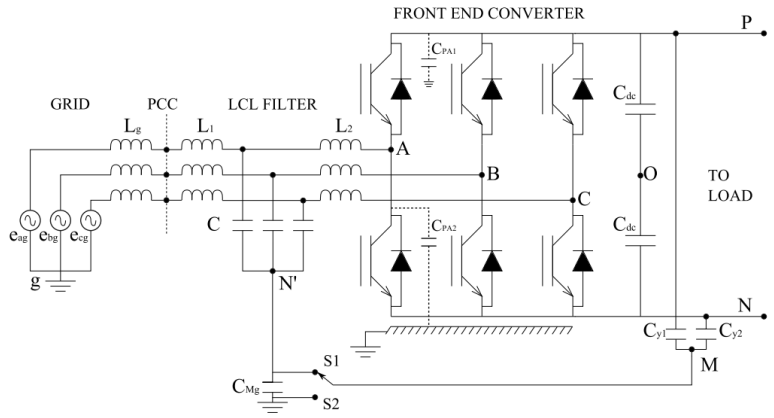

Figure 5.2: Schematic borrowed from (Acharya and John, 2010) showing the implemented common-mode filter.

5.2.5.2 System Start Up

If the DC bus capacitors are discharged and the converter is connected to the electrical grid, this will produce a big inrush current that could damage the IGBTs. That is why, a pre-load resistor connected to the mains circuit breaker is used to charge the DC bus capacitors through the IGBTs diodes.

There will always be the first transient to charge the grid side inductors and the capacitors from the LCL filter, but since their values are small, this transient does not present a high energy. Once the DC bus voltage is the grid rectified value, the pre-load resistor can be short-circuited and the converter can be switched on.

In Fig. 5.3 the start-up operation can be observed. First the DC bus capacitors are charged through the pre-load resistor, then it is short-circuited and finally the

converter is switched on. This is the same procedure for both converters.

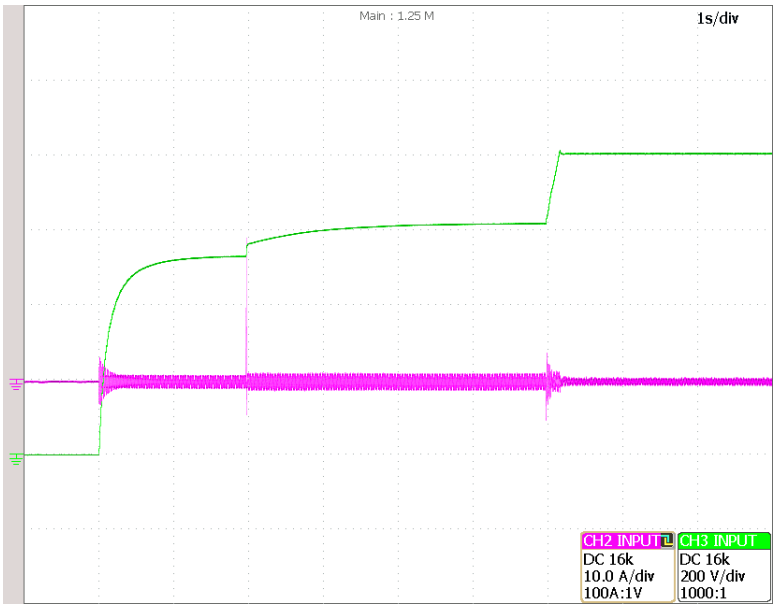

Figure 5.3: Start-up operation of the converters.

The voltage just before the start-up of the converter is then the rectified voltage. Theoretically it should be $230\sqrt{6} \approx 563.38\,\text{V}$ but it is found to be $\approx 620\,\text{V}$. This is due to the the common-mode voltage compensation filter described in the previous section: a small current flows from the middle point of the bus to the LCL filter capacitors common point. This exact behaviour has been found in simulation as well.

5.2.5.3 Grid Isolation Transformers

For the inversion operation, two DC voltage power supplies in series are connected to the DC bus. These power supplies are supposed to be isolated, but when trying to inject current to the mains, high frequency currents take a path to the earth and open the differential protection switch (30 mA). This may be due to a high frequency isolation fault on the DC voltage power supplies. To avoid this problem, three low-frequency transformers have been connected between the converter and the electrical grid.

Fig. 5.4 depicts the schematic of the transformers and Table 5.1 lists the measured values at 50 Hz for one of them. The turns ratio n is calculated as the geometric mean of the turns ratio in open and short circuit, that is, $n = \sqrt{n_o n_c} = 1.00763$.

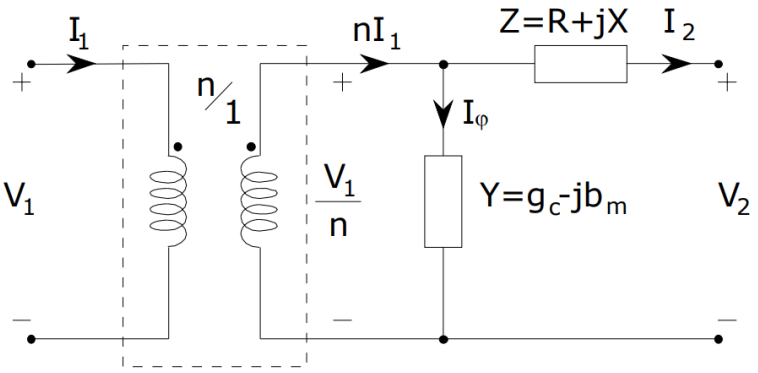

Figure 5.4: Low frequency transformers equivalent schematic.

Table 5.1: Low-Frequency Isolation Transformers Parameter Values.

X	1.085 µH	R	0.303 mΩ
b_m	1.827 mH	g_c	0.694 Ω
n_o	0.979	n_s	1.037

5.3 Controller Implementation

This section is devoted to the operation of the DSP for the real-time control of the converters. Besides the controller, all the configurations for the DSP, interruptions, peripherals and memory are also carried out in Simulink™ by using the Embedded Coder Support Package for Texas Instruments C2000 Processors.

5.3.1 Controller Execution Structure

A general interruption has been set to perform the control task at the sampling frequency of 20 kHz, that is, every 50 µs. This interruption triggers the ADCs and when the conversion is done, all the controller computations are carried out. Finally, the new control values obtained are loaded into the PWM modulators. As earlier pointed out, the output PWM control signal going to the drivers (the switching frequency) has same frequency value of 20 kHz.

Obviously, the sampling, the controller computation tasks and the PWM modulators loading cannot last longer than 50 µs to avoid overruns in the execution. As an external protection, a watchdog is triggered every time the interruption is executed. If this does not happen because the firmware crashes or any other reason, it instantly stops the converter by disabling the drivers.

5.3.2 Automatic Code Generation

Some years ago, without floating point units and the lack of real-time debugging tools (among other difficulties), the implementation of a digital controller was not a simple task. Nowadays, as an example, a controller designed in Simulink™ (from Matlab™) can be automatically coded by the Embedded Coder Toolbox™. This generates a project ready to be compiled in Code Composer Studio™ and programmed into the DSP, the whole operation taking only a few seconds. Moreover, any parameter value can be updated in real time for debugging or tuning purposes.

Fig.5.5 shows the high level of the developed controller in Simulink™. This is the main interruption code, executed periodically. Observe the inputs (ADCs) on the left-hand side of the image, the outputs (PWMs) on the right, and the controller in between. The main advantages of this design methodology are the possibility to simulate the controller in the same environment before the implementation, and the configuration and design by means of a graphical interface.

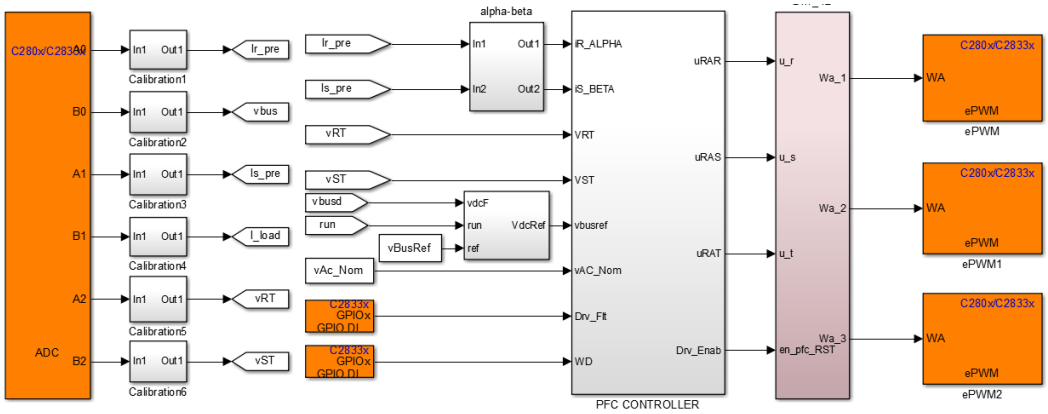

Figure 5.5: High level of the controller designed in Simulink™, ready to be built, compiled and programmed into the DSP.

5.3.2.1 Hand-Written Code vs. Automatically Generated Code

This topic can be very extensive, and even if there are some studies comparing both methods, the results are very specific and difficult to extrapolate. The humble ideas expressed here are only based on personal experience and are very generic.

The main difference between hand-written and automatically generated code is their structure. The last one tends to be more monolithic (with longer, but less number of functions). It can also be optimised for different objectives including traceability, execution efficiency or RAM memory optimisation, generating very complex projects in a matter of seconds. It is virtually error free and in the case of Embedded Coder™ from Matlab™, the generated code is certified for critical applications like automotive.

On the other hand, a firmware engineer has full freedom to write the code, accessing to any configuration or peripheral options that may not be available from the automatic code generation tool. The resulting code tends to be lighter since it is less conservative (only including necessary protections or castings on variables) but will take longer to finish and may contain errors difficult to fix. In general, time execution are very similar for both cases, being the hand-written code slightly faster.

Finally, it is important to mention that there are tools to check the generated code in software and hardware. The first one uses the generated code to run a simulation, and the second one needs a hardware in the loop (HIL) testing device that will work with the real DSP.

5.3.3 Code Optimisation and Fast Library

A Fast Run-Time Support library (Texas Instruments, 2008) is available on-line for the TMS320F28335 DSP in order to accelerate the computation of some time consuming mathematical operations like divisions, square roots or trigonometric functions. In our case, this library was used only for divisions since the sin and cos functions are implemented by means of look-up-tables, and the square roots by using another method based on the feedback loop shown in Fig. 5.6.

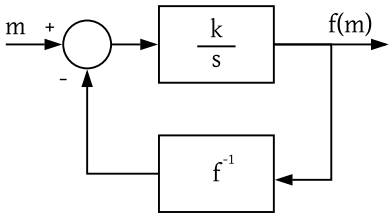

Figure 5.6: Feedback loop used to compute the square root function.

Thus, the function of the input parameter m, $f(m)$, can be seen as the steady-state value of the output[2] y of this non-linear differential equation

$$\frac{\mathrm{d}}{\mathrm{d}t}y = \frac{1}{k}(m - f^{-1}(y)),$$

where k is a constant value, proportional to the settling-time. It is easy to prove that the solution in steady state is simply $y = f(m)$.

Hence, to compute the square root, f^{-1} needs to be the square function. This is very useful since the square root function is a time consuming operation for a DSP, but not its inverse (the square function). Therefore, this method gives (after a short

[2]Time dependencies have been dropped for an easier reading.

transient depending on the constant parameter k) the square root of a slow moving input $m(t)$ within a few multiplications and additions.

The differential equation $\frac{\mathrm{d}}{\mathrm{d}t}y = \frac{1}{k}(m - y^2)$ turns out to be a Riccati's equation and the closed form solution is $y = \sqrt{m}\tanh\left(\frac{\sqrt{m}}{k}t\right)$ (for a null initial condition). This formula can be used to properly choose the parameter k from a dynamics point of view.

5.4 Set-up as a Rectifier

5.4.1 Single-Phase VSC

In this section, the experimental results for the full-bridge single-phase VSI as a rectifier are presented. From the full plant (three-phase three-wire VSC), only one LCL branch is used and one of the three legs from the bridge is permanently open. The other two legs will switch in a complementary fashion, exactly as it happens in an H bridge.

The nominal load is $83.3\,\Omega$ ($1.92\,\mathrm{kW}$ since the average DC bus voltage is set to be $400\,\mathrm{V}$). In steady state, the controller will keep the current in phase with the grid voltage in all cases, giving a unitary power factor[3].

5.4.1.1 Steady-State Operation

Fig. 5.7 shows the steady-state of the converter at zero load. It is important to highlight that the operation at zero current does not present any difficulty since the converter is bi-directional. In uni-directional converters, it is usual to have a pulsating current at zero or very light load. There is a small current consumed by the converter which corresponds to the losses generated by the parasitic resistances of the components (Joule effect) and the semiconductors switching losses. This dissipated power is approximately $50\,\mathrm{W}$ since the RMS value of the measured current is $\approx 0.21\,\mathrm{A}$.

On the other hand, the steady-state operation of the converter at full load is shown in Fig. 5.8. Fig. 5.9 presents the grid current harmonic content, the active and apparent power, and the power factor measurements. In this case the efficiency of the rectifier is around 94.5%.

Note that in those frequencies where a resonator is placed, the current harmonic content is null, or very small. Also note that, as predicted in Chapter 2, the voltage bus oscillates around the reference value. The theoretical voltage ripple is $31.6\,\mathrm{V}$, very similar to the actual ripple in the waveform (around $32\,\mathrm{V}$).

[3]Unity-power-factor operation means $\cos\varphi = 1$ with respect to the mains fundamental frequency.

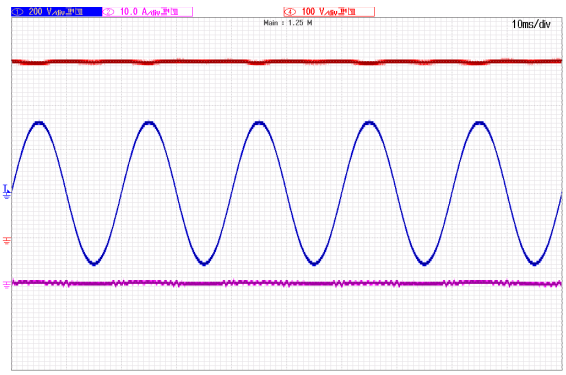

Figure 5.7: Steady-state operation of the single-phase VSC at no load. DC bus voltage (red, 100V/div), grid current (pink, 10A/div) y grid voltage (blue, 200V/div).

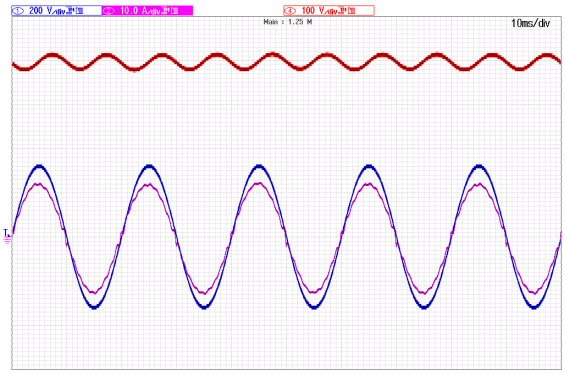

Figure 5.8: Steady-state operation of the converter at full load (83.3 Ω). DC bus voltage (red, 100V/div), grid current (pink, 10A/div) y grid voltage (blue, 200V/div).

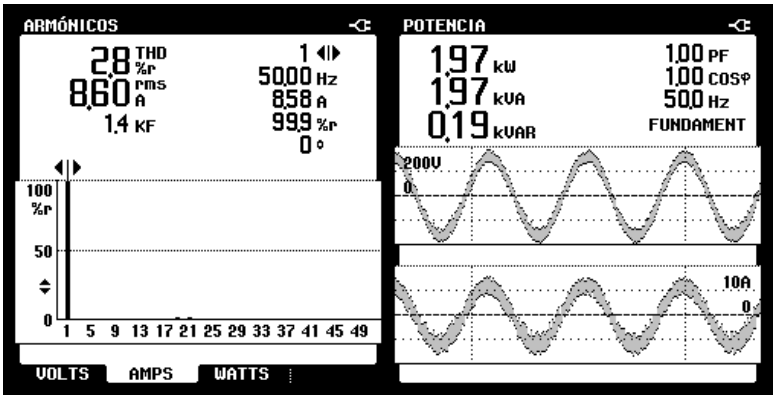

Figure 5.9: Steady-state grid current harmonic content at full load (left). Steady-state power factor, P and Q graphics (right).

This fact justifies the use of the comb filter in the feedback path in order to extract the signal average value. Even if the voltage PI controller would attenuate any disturbance at 100 Hz, the comb filter can reject it completely reducing the control effort of the current loop.

5.4.1.2 Load Variations

Fig. 5.10 represent, a transition from no load to full load (83.3 Ω) and vice versa. The second case is the most unfavourable, but the system reaches the steady-state in 150 ms, i.e., less than 8 grid voltage periods.

As it can be observed, the overshoot in the second case is only a 10% of the nominal value. On the other hand, the harmonic components present in the grid current just after the transient will take a bit longer to disappear since the resonators gains are not as optimised as they could.

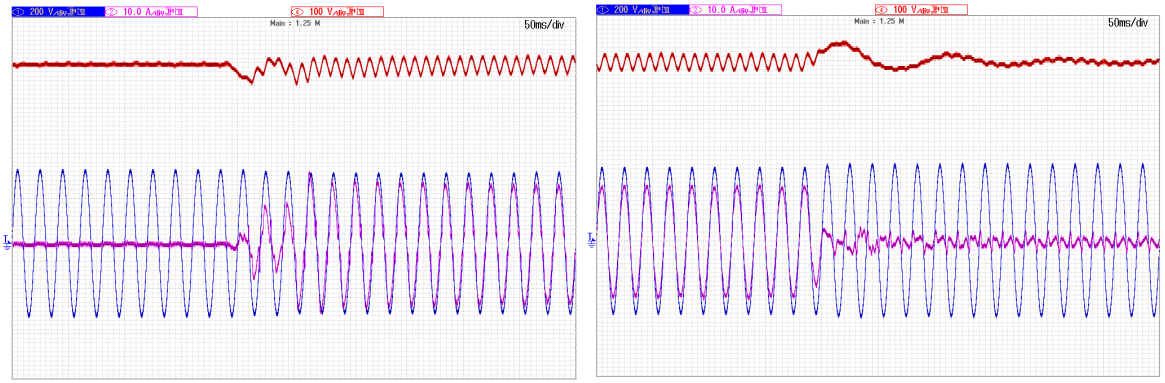

Figure 5.10: Variation from no load to full load (83.3 Ω) and vice-versa. DC bus voltage (red, 100V/div), grid current (pink, 10A/div) and grid voltage (blue, 200V/div).

As it was already presented in Chapter 4 and as it will be shown in other experimental results along this chapter, setting the values for the resonators gains obtained thanks to the HIFOO numerical method, and using the resonators reset, will give a faster dynamics without compromising the system robustness.

5.4.1.3 Distorted Grid Voltage

Fig. 5.11 shows the converter operation when the grid voltage presents harmonics according to the IEC 77A Class 1 pattern.

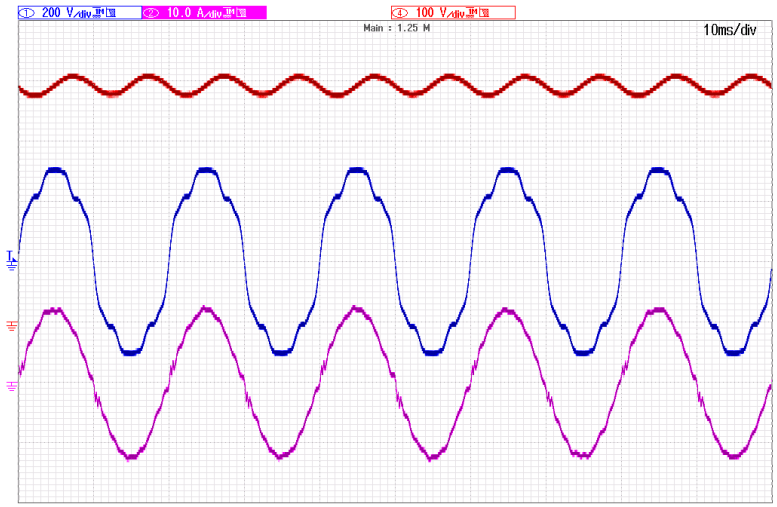

Figure 5.11: Steady-state at full load with grid voltage according to the IEC 77A Class 1 pattern. DC bus voltage (red, 100V/div), grid current (pink, 10A/div) and grid voltage (blue, 200V/div).

And Fig. 5.12 shows the grid voltage and current harmonic content. Exactly as in the first tests, and even if the grid voltage presents harmonics, the grid current harmonic content is very low (except, obviously, for the 50 Hz component).

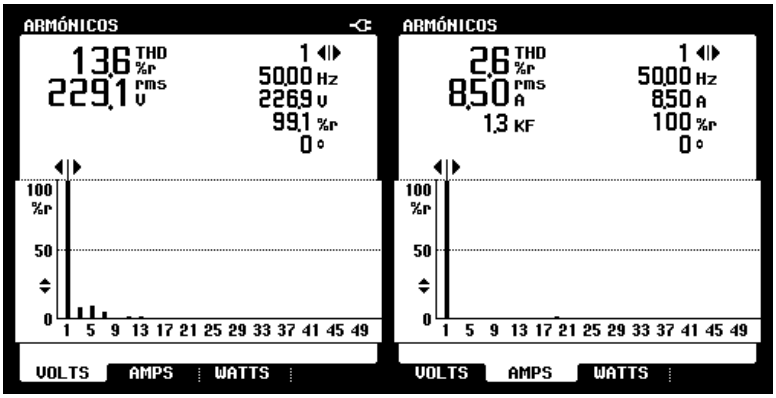

Figure 5.12: Harmonic content to full load according to the IEC 77A Class 1 pattern (left) and grid current (right).

This fact shows the good reference tracking and disturbance attenuation capabilities of the resonant controller for periodic signals with spectral content at the frequencies where the resonators are located. At higher frequencies, the closed-loop plant behaves as a low-pass filter and the harmonic content is naturally very small.

5.4.2 Three-Phase Three-Wire VSC

Several experimental tests have been carried out as a rectifier to test the performance of the designed controller in the three-phase three-wire VSC. These include operation in steady state (full load, no load, with different power factors and with a large inductive grid impedance) and during transients (load variations, sags, swells, frequency variations and ringings). Note that the resonator gains used for this application have been found by using the HIFOO numerical algorithm.

5.4.2.1 Steady-State Operation

Fig. 5.13 shows the operation of the rectifier at no load in steady state. The currents that can be observed correspond to the losses of the converter, since the load is not consuming any power (approximately 150 W). Observe that even if the currents are small (~ 0.24 A RMS per phase), the controller forces them to be sinusoidal and in phase with the mains at all times.

On the other hand, Fig. 5.14 shows the unity-power-factor operation of the rectifier at full load in steady state. In this case, the load resistance is again $R = 83.3\,\Omega$. Since the DC bus voltage is regulated to 800 V, the dissipated power by the load is 7.68 kW. And Fig. 5.15 presents the the power quality and line currents harmonics spectrum in all three phases. Observe that the currents harmonics are small for all frequencies, being 1% the measured THD.

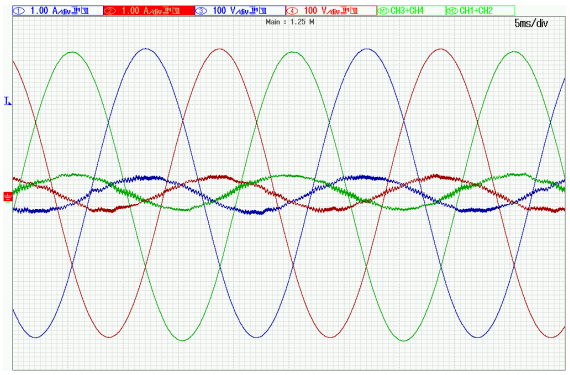

Figure 5.13: Phase-to-neutral voltages and line currents at no load (currents 1A/div, voltages 100V/div).

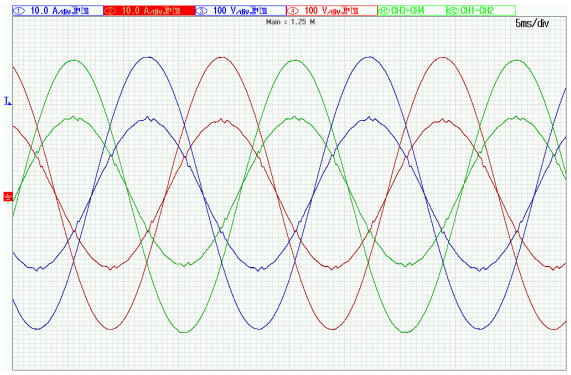

Figure 5.14: Phase-to-neutral voltages and line currents at full load (currents 10A/div, voltages 100V/div).

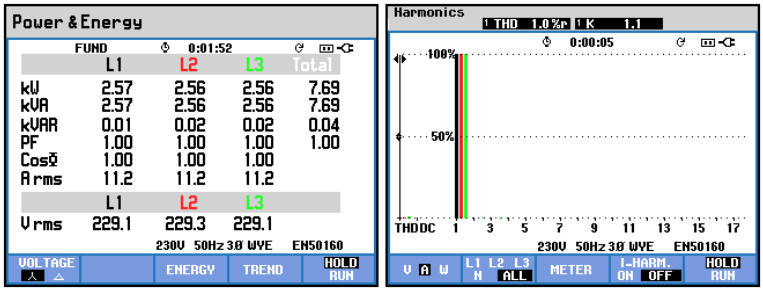

Figure 5.15: Power quality in all three phases (left) and line currents harmonics content (right) at full load and unity-power-factor operation.

The DC bus voltage is not depicted in these waveforms, but as it will be shown in the next experimental results, it does not present any appreciable low frequency ripple as predicted by the theory in Chapter 2.

5.4.2.2 Load and DC Bus Voltage Variations

This section is devoted to load transition and variations in the DC bus voltage. The no-load to full-load (and vice-versa) transitions are shown in Fig. 5.16. As it can be observed, the first transient presents less than 2% undershot and a 6.5% overshoot during the second one. Also note that the steady state is reached in approximately 60 ms in both cases.

The effect of the resonators reset (implemented in this case) can be observed in the transition from full load to no load (the difference of performance can be compared with respect to Fig. 5.10). When the load is disconnected, the only available path for the flowing current is the DC bus capacitor and the DC bus voltage starts to increase. However, when the resonators reset is triggered, the current demand decreases and the reference value is quickly recovered. Furthermore, the currents do not present high frequency harmonics since all resonators are empty.

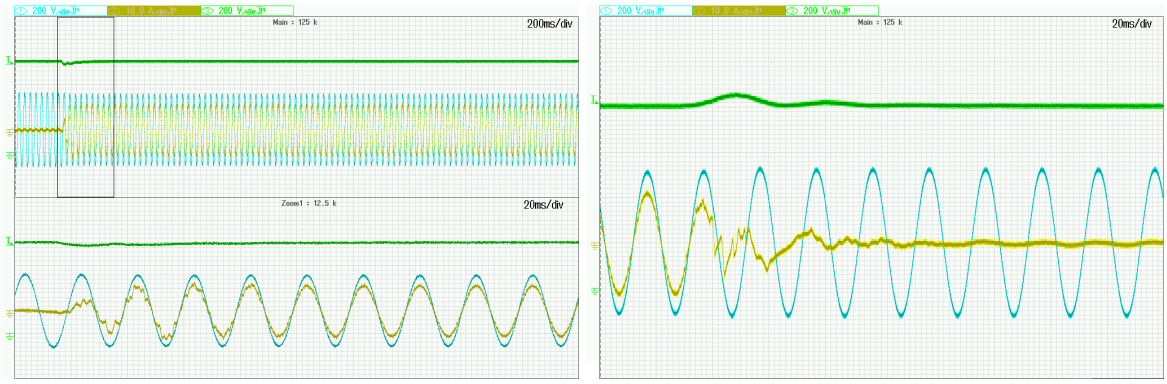

Figure 5.16: Transitions from no-load to full-load (left) and vice-versa (right) in the three-phase VSC. Phase-to-neutral voltage (blue: 200 V/div), line current (yellow: 10 A/div), DC bus voltage (green: 200 V/div).

Another interesting test carried out is the introduction of variations in the DC bus voltage, presented in Fig. 5.17. The voltage set point was changed from 800 V to 750 V and back to 800 V again. There is almost no under nor overshoot and the transient lasts 3 grid cycles in the first case and only 2 in the second one. While the bus voltage is 750 V and since the load is a resistor, the currents decrease fulfilling the Ohm's law to keep the same DC bus voltage value.

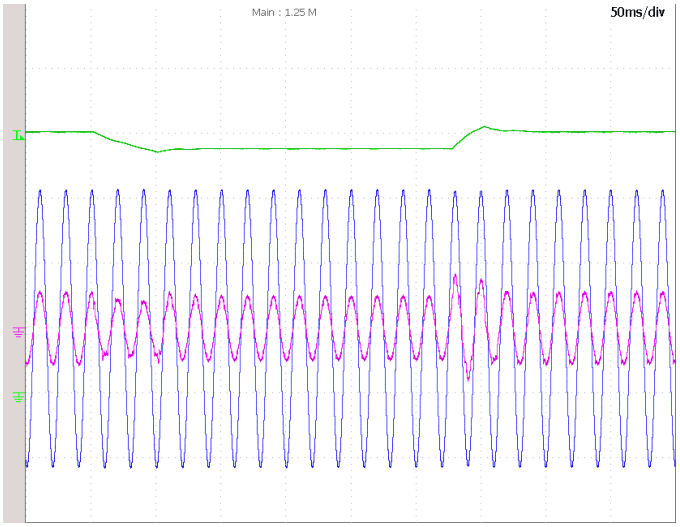

Figure 5.17: Variations in the DC bus voltage from 800 V to 750 V and vice-versa. Phase-to-neutral voltage (blue: 150 V/div), line current (pink: 10 A/div), DC bus voltage (green: 200 V/div).

5.4.2.3 Large Grid Impedance

Large grid impedances are common in electrical systems with, for example, too thin cables or weak generators. This is a source of problems since the current consumption will change the voltage at the connection point as explained in Chapter

2. In some cases, this can create undesired oscillations and the controller has to be robust enough to face these disturbances.

In the same vein, an issue which is attracting increasing attention is the stabilisation of micro-grids or on-board grids (like in planes and boats) due to the growing number of converters (behaving like constant power loads or CPL) that they need to handle.

These experimental results show the capability of the converter to work normally when the grid impedance is large. Fig. 5.18 presents the converter steady-state operation with a grid impedance of 4.1 mH per phase at full load. Note that the measurements are taken at the input of the converter, just after the inductors simulating the grid impedance since it is seen as part of the mains.

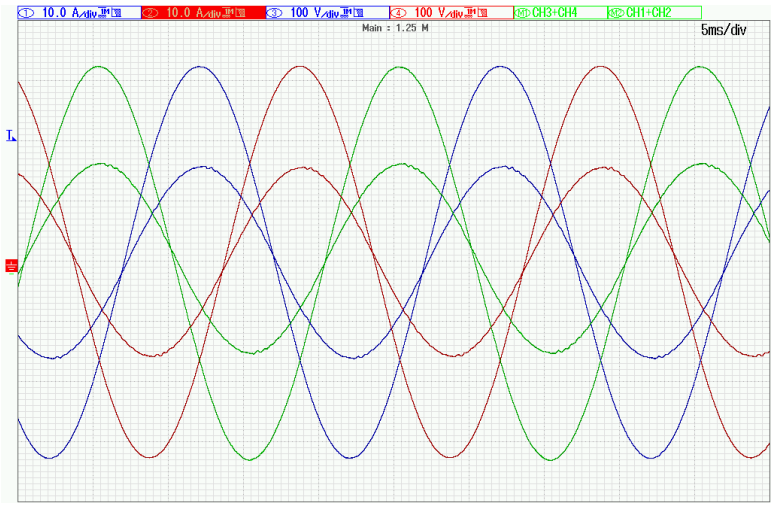

Figure 5.18: Rectifier operation in steady state with an inductive grid impedance of 4.1 mH. The signal scales can be found at the top of the screen capture.

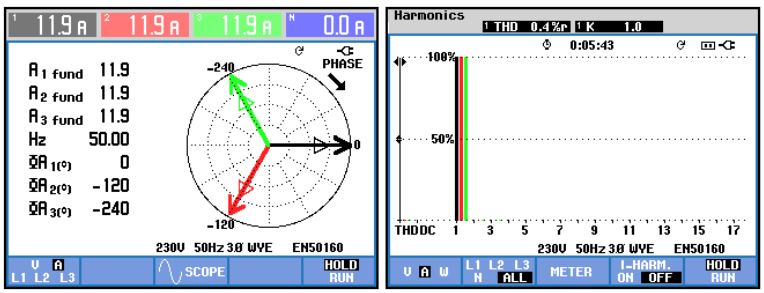

Figure 5.19: Currents vectors and harmonic content for full load with an inductive grid impedance of 4.1 mH.

The grid inductance is added to the LCL filter, increasing the attenuation and filtering high frequency harmonics even more. The 4.1 mH from the grid moves the LCL resonance frequency from 4.3 kHz to 2.3 kHz. As a reference, the attenuation

from the control signal to the phase-to-neutral currents at 20 kHz is reduced in 30 dB approximately. That explains why the measured value of THD for all phases, as shown in Fig. 5.19, is only 0.4% with respect to the 1.0% obtained in same case, but with no grid impedance (Figs. 5.14 and 5.15).

5.4.2.4 Reactive Power Generation

Adding a reactive component to the input currents can be useful in several circumstances. One of the most important ones is to improve the power factor, usually achieved by adding capacitor banks in parallel to the mains and compensate the inductive currents. But this is not the only possibility when working with reactive powers. For example, it is also a way to deal with the aforementioned stability issues related to the grid impedance, helping to restore the electrical grid.

In these tests, the converter is compelled to produce reactive power. Therefore, the currents amplitudes increase and their phases change in order to fulfil the active power balance imposed by the voltage controller.

Fig. 5.20 depicts the steady state of the converter when a capacitive current of 8 A is demanded, that is, 3.9 kVA. Fig. 5.21 shows the power quality and the currents harmonic content can be observed. Note that the power factor is only 0.03 and the THD is only 0.5%.

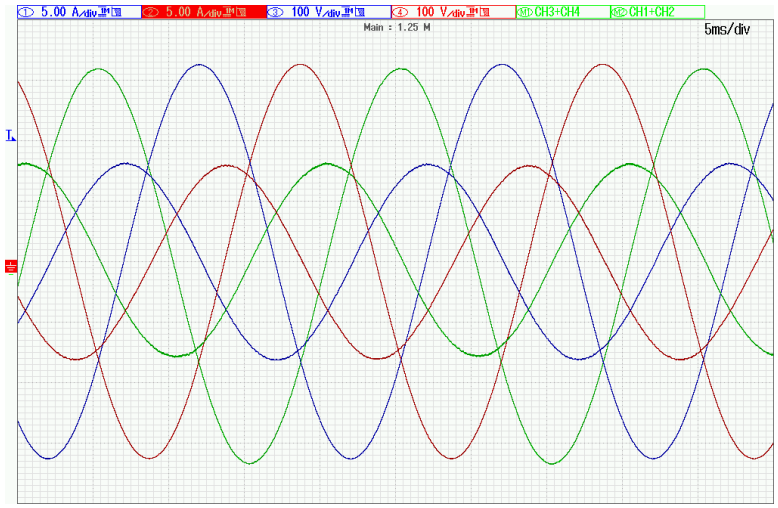

Figure 5.20: Phase-to-neutral voltages and line currents at no load in steady state when a reactive power of 3.9 kVA is demanded. The signal scales can be found at the top of the screen capture.

For the sake of conciseness, more experimental results dealing with reactive power are included in the next section, where the converter operates as an inverter connected to the electrical grid.

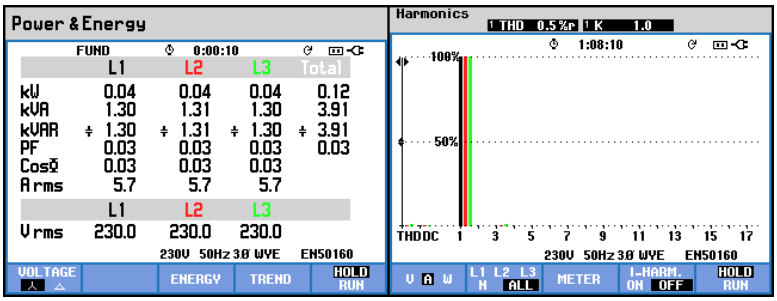

Figure 5.21: Power quality in all three phases (left) and line currents harmonics content (right) when a reactive power of 3.9 kVA is demanded.

5.4.2.5 Sags and Swells

The endurance of the controller facing sags and swells has been tested with the ITI (CBEMA) curve (Information Technology Industry Council, 2000) as a reference. Fig. 5.22 depicts one version of this curve, borrowed from (Brito et al., 2014). The purpose of this curve is to test the equipment integrity (especially when the voltage swell is a very high percentage of the nominal value) and only the right half of the graph is interesting to show the controller performance.

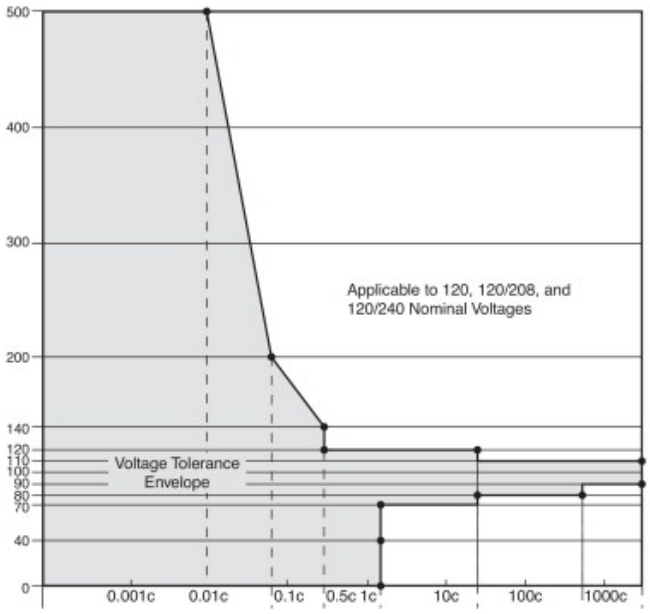

Figure 5.22: Version of the ITI (CBEMA) curve for the security of electricity supply, borrowed from (Brito et al., 2014). The vertical axis represents the % of the mains voltage nominal value and the horizontal axis the time in grid cycles.

Fig. 5.23 shows a 500 ms duration swell of 120% of the mains voltage nominal value and then, an indefinite sag of an 80%. The steady-sate is reached in both cases reliably.

The limitation for swells is not the controller itself, but the boost condition: by

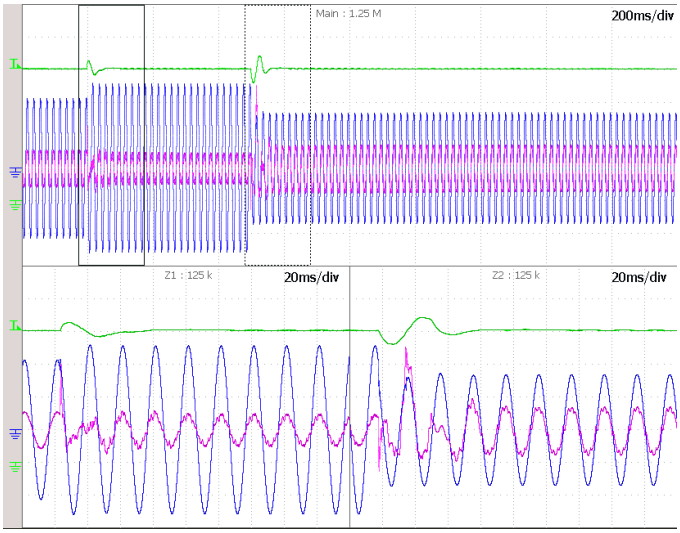

Figure 5.23: One phase current and DC bus voltage responses facing voltage variations in all three phases. Phase-to-neutral voltage (blue: 150 V/div), line current (pink: 10 A/div), DC bus voltage (green: 200 V/div).

construction of the VSC, the DC bus voltage needs to be greater than $\sqrt{6}$ times the phase-to-neutral voltage RMS value. With respect to sags, the limit will be the current rating of the components since the currents will be bigger for the same power value.

The DC bus voltage is steady in these tests because the sag occurs in all the three phases at the same time. However, Fig. 5.24 shows the converter response when there is a sag for an indefinite amount of time in only one phase.

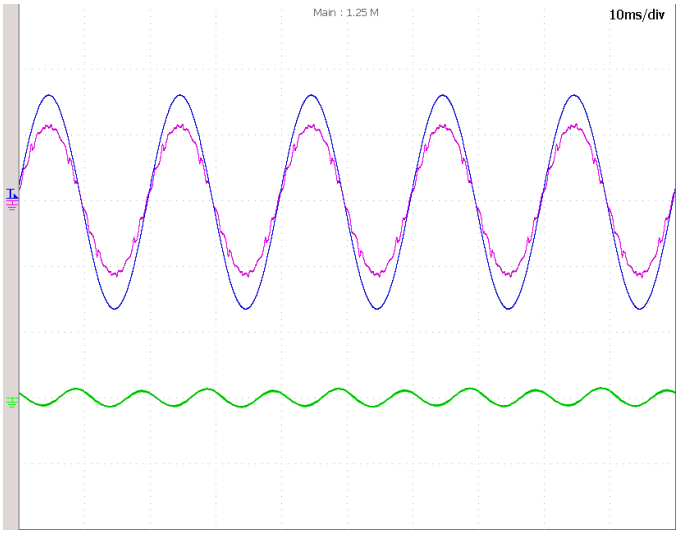

Figure 5.24: One phase current and DC bus voltage in steady state when there is a sag in one phase. Phase-to-neutral voltage (blue: 150 V/div), line current (pink: 10 A/div), DC bus voltage (green: 200 V/div).

As it can be observed, since the system is not balanced any more, the DC bus voltage starts to oscillate around the set point value as predicted by the mathematical model. Exactly as in the single-phase case, the comb filter will reject these harmonic components in only one grid cycle.

5.4.2.6 Distorted Grid Voltage

When the phase-to-neutral voltages present high harmonic content, the system needs to keep producing sinusoidal line currents in phase with the voltages fundamental harmonic. This is possible thanks to the PLL, which continuously gets the voltages fundamental harmonic, and to the resonators, which reject the other ones.

On the left-hand side of Fig. 5.25, the phase-to-neutral voltages are those defined according to the IEC 77A Class 2 pattern, while the right-hand side shows the operation of the converter when voltages are clipped. Figs. 5.26 and 5.27 show, respectively, the voltage and current harmonic content in one of the phases. The currents harmonic contents increase a bit with respect to normal operation, and the DC bus voltage is not affected.

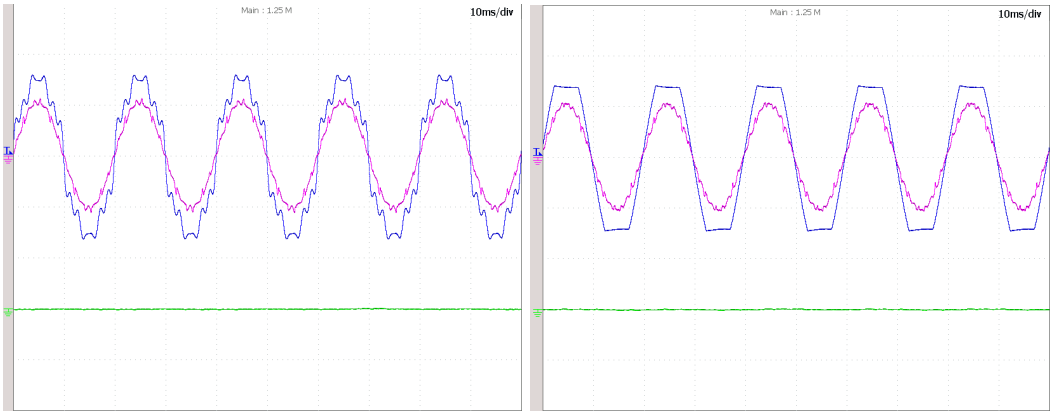

Figure 5.25: Phase-to neutral voltages according to the IEC 77A Class 2 pattern (left) and clipped voltages to 75% of nominal value (right) (blue: 200 V/div), same phase line current (pink: 10 A/div) and DC bus voltage (green, in AC mode: 50 V/div).

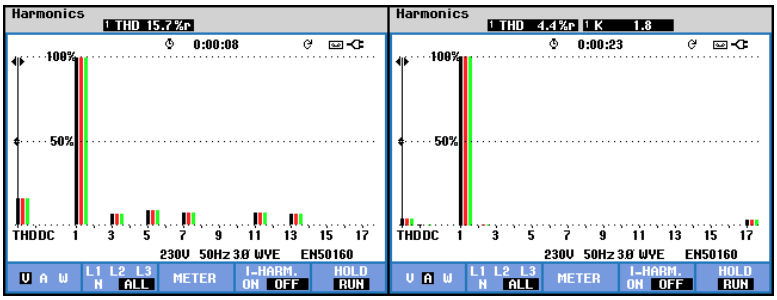

Figure 5.26: IEC 77A Class 2 phase-to-neutral voltages, and line currents harmonic content.

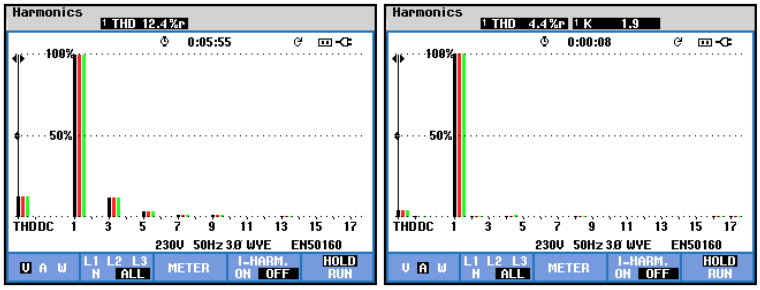

Figure 5.27: Clipped voltage phase-to-neutral voltages and line currents harmonic content.

5.4.2.7 Frequency Disturbances

Fig. 5.28 shows a step variation of the grid frequency from 50 Hz to 52 Hz at $t = 10$ ms. Even if the grid frequency changes suddenly, the PLL of the controller follows the variation retuning all the resonators and the comb filter to the new frequency value.

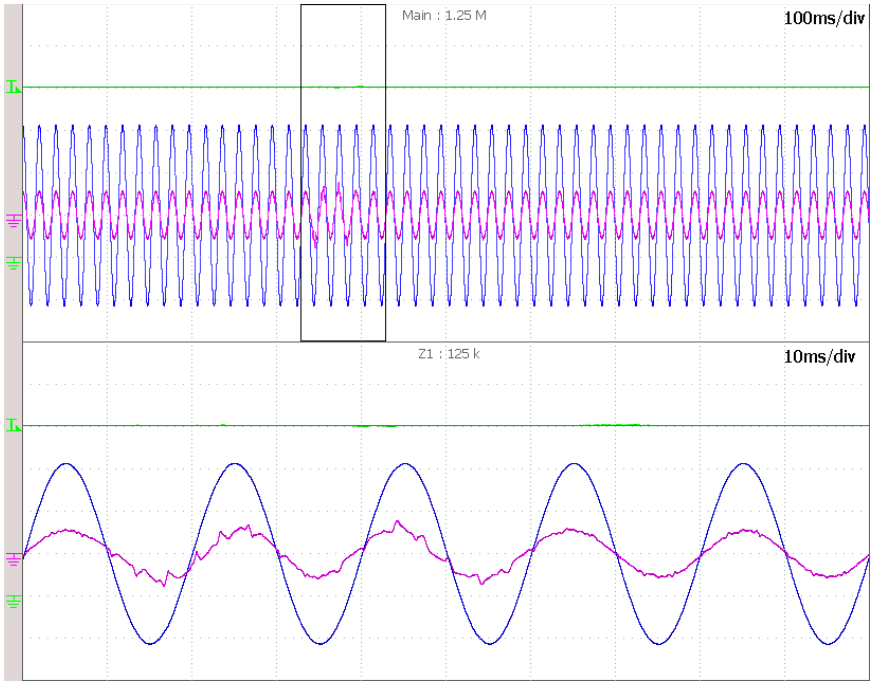

Figure 5.28: Variation of the grid frequency from 50 Hz to 52 Hz at $t = 10$ ms into the zoomed view (bottom). Phase-to-neutral voltage (blue: 150 V/div), line current (pink: 10 A/div), DC bus voltage (green: 200 V/div).

Normally, changes in the grid frequency do not happen suddenly: they change smoothly if there is a mismatch between the power generated and the power consumed. This can be explained since most of the generators in the electrical grid are synchronous machines with a large inertia and cannot change their speed instantaneously, however, a step transient is a harder test condition.

Since the controller PLL can follow changes in the grid frequency value from 40 Hz to 70 Hz, the system can be used in areas with different fundamental frequencies like 50 Hz in Europe, Asia, Africa and Australia or 60 Hz in America.

5.4.2.8 Ringing in Grid Voltage

Ringings are caused by reactive components when a sudden change occurs in the grid, for example, when a power switch opens or closes connecting or disconnecting part of the electrical sector. The frequency of the ringing is determined by the values of inductance and capacitance in the system.

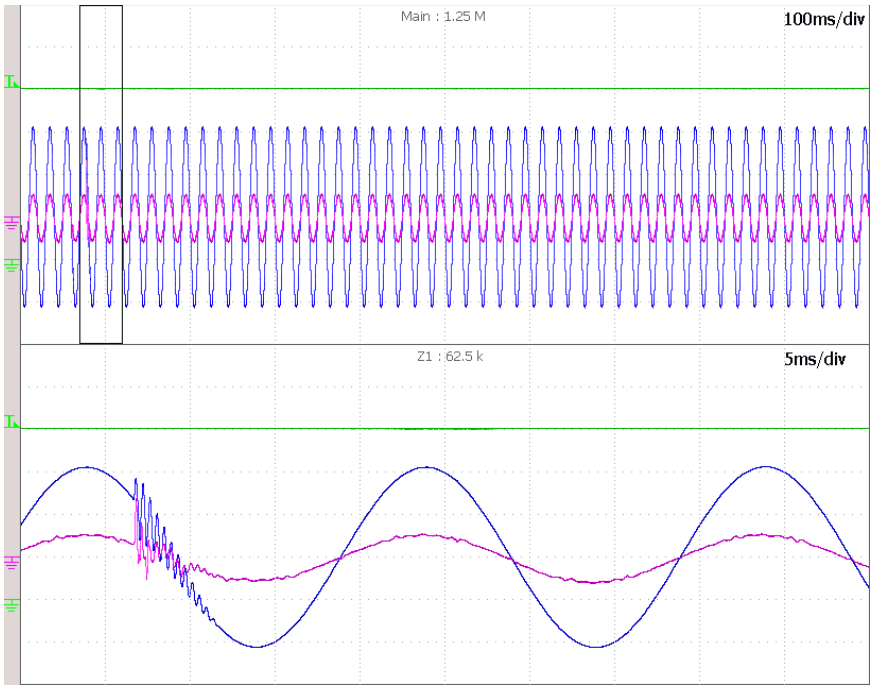

Figure 5.29: Dynamic response when a ringing in one phase-to-neutral voltage occurs. Phase-to-neutral voltage (blue: 150 V/div), line current (pink: 10 A/div), DC bus voltage (green: 200 V/div).

Fig. 5.29 shows the behaviour of the power converter when a ringing in one phase-to-neutral voltage occurs. In this case, the ringing lasts 5 ms, it presents a frequency of 2.4 kHz and the maximum amplitude at the beginning of the disturbance is a 10% of the nominal phase-to-neutral voltage value (the attenuation is linear with time). As it can be observed, currents recovers and the DC bus voltage seems not to be affected by this transient.

5.5 Set-up as an Inverter Connected to the Electrical Grid

5.5.1 Three-Phase Three-Wire VSC

The last experimental results section of this thesis deals with the three-phase three-wire converter operating as an inverter. As mentioned before in this chapter, in order to carry out these tests, a 800 V DC voltage is applied to the DC bus, and the three 1:1 low frequency transformers are connected at the converter input (between the mains and the LCL filter).

Since the voltage sources keep the DC bus charged to a constant value, the voltage control loop is disabled and the current references are commanded directly. First, the steady-state operation of voltages and currents is analysed and then, some power transients are carried out. Note that, for the sake of clarity, only one phase is shown in the waveforms.

Mostly all the tests in this section are performed with the converter connected to the mains. However, in order to test the controller performance under grid disturbances, some of the experimental results have been carried out by connecting the AC source with three 1 kΩ power resistors in parallel (in star connection) in between. This way, the grid voltage is imposed by the AC source and the current delivered to the resistors will be shared between the voltage source and the inverter.

5.5.1.1 Steady-State Operation

Fig. 5.30 presents the converter in steady-state at zero load: no current is being injected from the DC bus to the grid. The current measurements and voltage THD can be found in Fig. 5.32. As it can be observed, the RMS mains voltage value is 240 V, with a frequency of 50 Hz and the THD is 2.5%.

Because the grid currents are commanded directly and the voltage sources connected to the DC bus compensate for any losses, they are virtually zero[4] (an average of only 127 mA RMS measured per phase).

The next test, presented in Fig. 5.31, is the inverter working in steady-state at full-load and unity-power-factor operation, injecting a current of 15 A amplitude per phase to the grid. As it can be seen in the measurements shown in Fig. 5.33, the total power is 7.64 kW (2.55 kW per phase). The currents THD is around 1.5% and the power factor is virtually 1 (0.9993 for phases 1 and 2, and 0.9805 for the third one).

[4]Remember that during rectifier operation at no load, some grid current is needed to compensate for the converter parasitic and switching losses and keep the DC bus voltage constant.

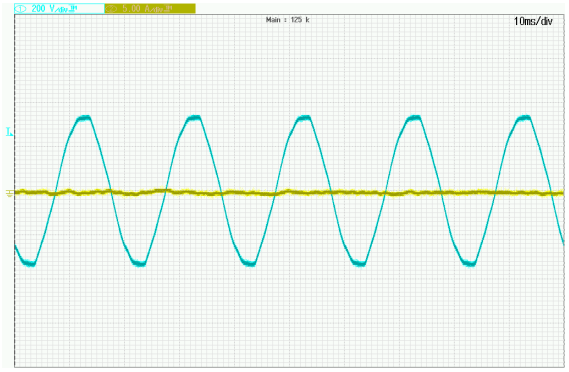

Figure 5.30: Grid-connected three-phase three-wire inverter at zero load (steady-state).

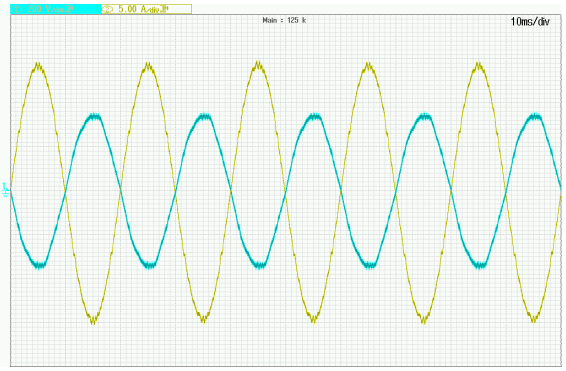

Figure 5.31: Grid-connected three-phase three-wire inverter at full load (steady-state).

HARMONIC ANALYZER
coupling: ac+dc bandwidth: wide

V	phase 1	phase 2	phase 3	
fund	239.57	238.24	240.58	V
rms	239.64	238.57	240.66	V
THD	2.543	2.634	2.475	%
H5	2.005	2.031	1.924	%
H5	4.8024	4.8391	4.6296	V
watts	217.32m	214.62m	378.42m	W
watts.f	217.29m	214.32m	378.16m	W

TRUE RMS VOLTMETER
coupling: ac+dc bandwidth: wide

A	phase 1	phase 2	phase 3	
rms	125.87m	112.31m	145.49m	A
dc	54.677m	30.982m	-87.172m	A
ac	113.37m	107.95m	116.48m	A
peak	399.0m	339.9m	-406.8m	A
cf	3.17	3.03	2.80	
surge	435.7m	395.5m	-468.6m	A
mean	96.39m	99.00m	118.4m	A
ff	1.306	1.134	1.229	
frequency	49.995			Hz

Figure 5.32: Mains voltage THD (left) and current measurements (right). Inverter operation at zero load.

POWER ANALYZER
coupling: ac+dc bandwidth: wide

	phase 1	phase 2	phase 3	
watts	-2.5529k	-2.5465k	-2.5599k	W
VA	2.5546k	2.5484k	2.6109k	VA
VAr	93.285	96.804	513.67	VAr
pf	0.9993	0.9993	0.9805	
rms	247.77	247.24	249.03	V
rms	10.310	10.307	10.484	A
frequency	50.004			Hz
H5	0.000	-0.000	0.000	%
dc watts	-2.2031m	-1.6587m	-25.402m	W
V ph-ph	428.73	429.37	430.63	V

HARMONIC ANALYZER
coupling: ac+dc bandwidth: wide

A	phase 1	phase 2	phase 3	
fund	10.307	10.304	10.283	A
rms	10.309	10.306	10.286	A
THD	1.496	1.587	1.541	%
H5	0.007	0.015	0.021	%
H5	716.43µ	1.5020m	2.1551m	A
watts	-2.5537k	-2.5489k	-2.5617k	W
watts.f	-2.5535k	-2.5487k	-2.5614k	W

Figure 5.33: Power measurements (left) and grid currents THD (right). Inverter operation at full load.

To end this section, Fig. 5.34 presents the inverter in steady-state delivering 5 A active and −8 A reactive current per phase (capacitive operation). The theoretical RMS current value is $\frac{1}{\sqrt{2}}\sqrt{5^2+8^2} \approx 6.6\,\text{A}$. The total active power is approximately

2.55 kW and the reactive power is 4.07 kW. Fig. 5.35 shows the power and currents THD measurements.

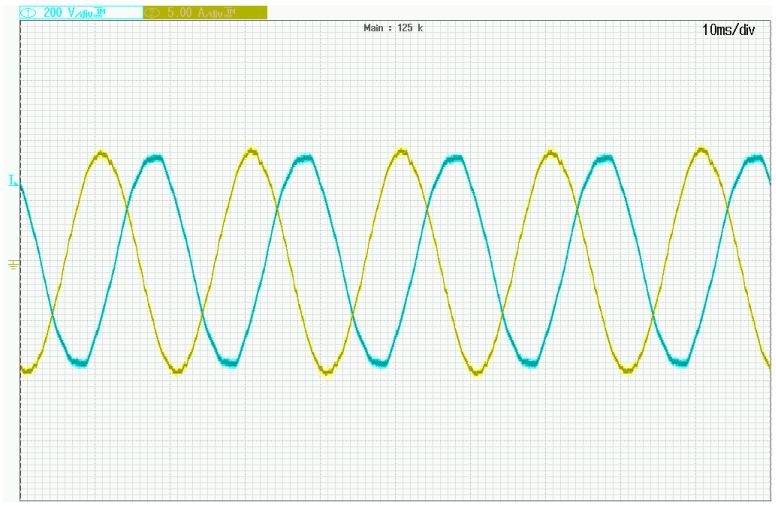

Figure 5.34: Steady-state inverter operation delivering 5 A active and −8 A reactive current.

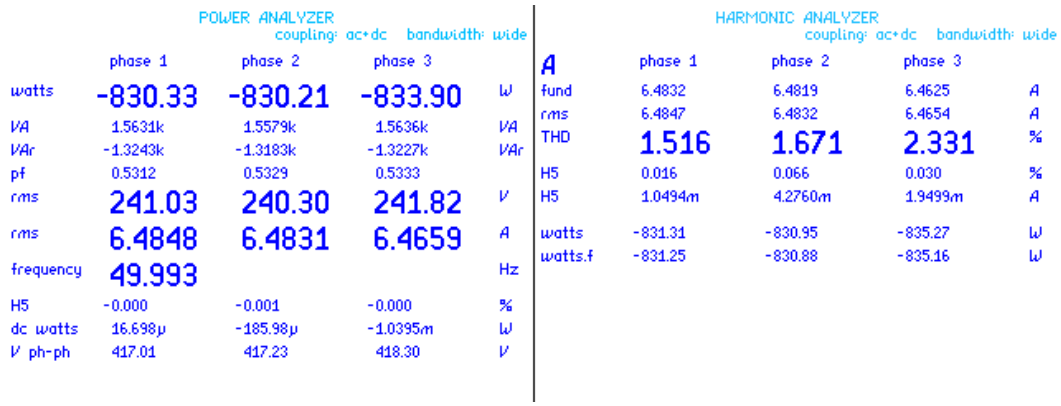

Figure 5.35: Power (left) and currents THD measurements (right). Capacitive steady-state operation.

5.5.1.2 Active and Reactive Power Transients

These tests present the converter performance under several transients involving active and reactive power, and voltage harmonics.

Figs. 5.36 and 5.37 shows a load variation in unity-power-factor operation from $\frac{5}{\sqrt{2}}$ to $\frac{15}{\sqrt{2}}$ A RMS and vice-versa. The settling time in both cases is about 3 grid periods, and even higher frequency harmonics are rejected in the same time window.

These tests are exactly the same as the ones presented in the previous section (working as a rectifier), but the power is flowing into the electrical grid instead.

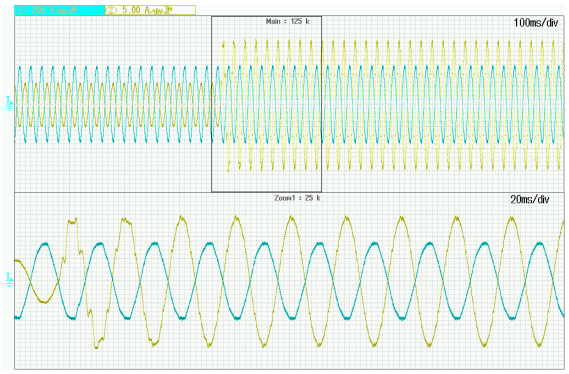

Figure 5.36: Load transient from low to high load. Inverter in unity-power-factor operation.

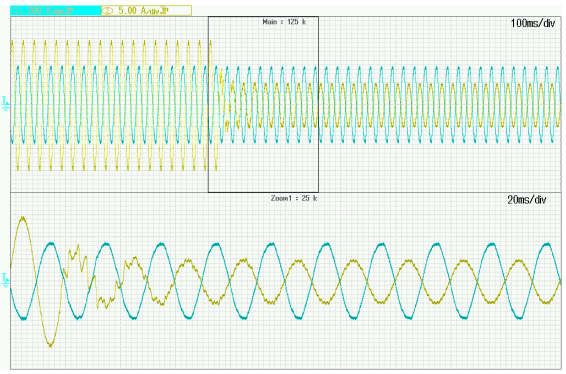

Figure 5.37: Load transient from high to low load. Inverter in unity-power-factor operation.

In Fig. 5.38, a sudden change from inductive to capacitive current is presented. The demanded active current amplitude is 5 A and the reactive power changes from 10 to −10 A. This time, the transient lasts only 2 grid periods.

This shows, not only the possibility of this converter to exchange reactive power with the grid, but also to act fast face to a sudden change in the demand or in the electrical sector.

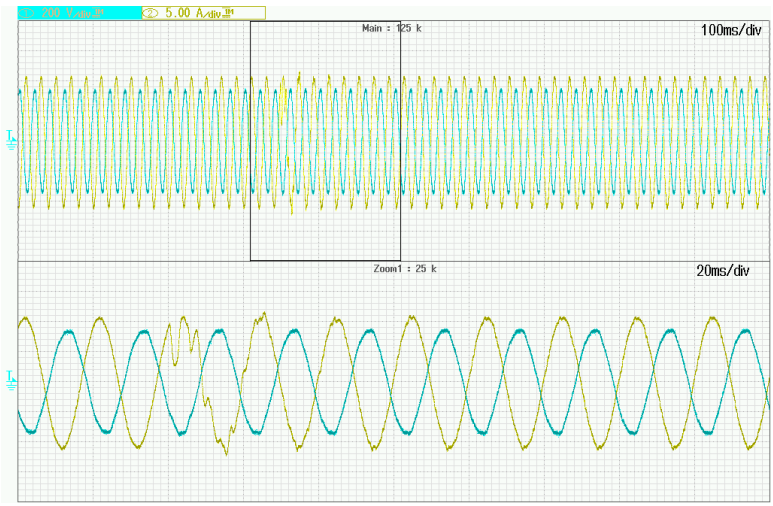

Figure 5.38: Transient from inductive to capacitive current during inverter operation.

And finally, Figs. 5.39 and 5.40 show a load transient when the phase-to-neutral voltages present a high harmonic content following the IEC 77A Class 2 pattern. The current changes from zero to an amplitude of 8 A and the steady-state is reached in 3 grid periods.

Note that in this test, the resonators reset never triggered since the DC bus voltage is kept constant by the DC sources. However, if the impedance of the device

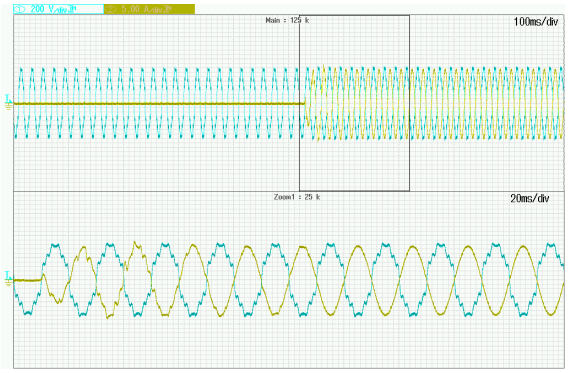

Figure 5.39: Load transient from zero to medium load. Inverter operation with voltage harmonics.

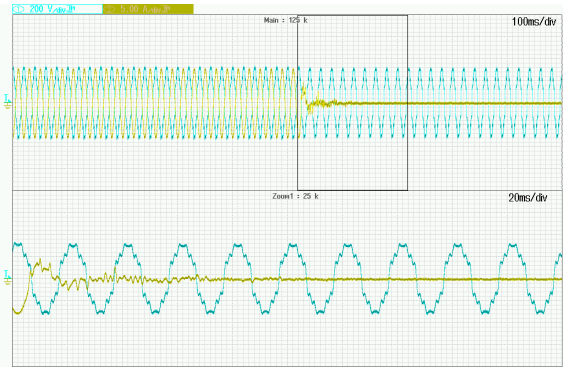

Figure 5.40: Load transient from medium to high load. Inverter operation with voltage harmonics.

connected to the DC bus was higher (like a battery), the voltage could vary in a transient and the resonators reset could be turned on.

"I learned very early the difference between knowing the name of something and knowing something."

Richard Feynman

6

Conclusions and Future Work

6.1 Introduction

In order to put this thesis into a wider context, and thanks to the background of few years working as a design engineer in the power electronics business, one can state that the general trend is, without any doubt, towards the digital world. Due to the growing complexity in products, microprocessors were adopted very fast by companies to carry out monitoring or management tasks, communications or other high level operations which would be very difficult to perform otherwise. Nevertheless, even if digital control was formally started in the mid 20th century, companies still tend to use analogue controllers to operate power converters, and this is due to three main reasons:

- The fact that microprocessors were expensive devices in the early stages, not very powerful to perform real-time control operations and difficult to use.
- There are specific and configurable integrated circuits designed to control the most popular power converters topologies.
- The design of digital controllers require a different knowledge from power electronics, firmware or software engineering.

However, micro-controllers are much cheaper, efficient and powerful nowadays (running very fast, with floating-point units or multiple cores) and there are tools to generate the code automatically, giving capabilities and advantages to digital controllers impossible to obtain in the analogue world. In that regards, this research tries to fill the gap in the design chain by setting a methodology to obtain and implement with ease a digital resonant controller.

6.2 Contributions

The main contribution in this research is in the resonant control field, more specifically in the design procedure and implementation of digital resonators in AFC control. This technique, which has been previously used in mechanical systems, has been introduced as a digital resonant controller, designed and experimentally verified in single- and three-phase voltage source converters.

From the controller perspective, the main contributions are:

- The resonator as a control element is analysed theoretically in continuous and discrete time. In the z-domain, it is important to know that these controllers may present non-minimum phase zeros, which will have implications for the higher level controllers.

- A design methodology has been developed within the AFC control technique framework for infinite-gain and finite-gain resonators, especially for low gains. Their angle can be chosen analytically to maximise the robustness, but the gain tuning constitutes a non-convex optimisation problem that was addressed numerically.
- Finally, an anti wind-up scheme to limit the control action has also been proposed. This system is useful to limit the resonators output in a fixed band to fulfil specifications or to avoid an over integration during big transients.

And from the electronics side:

- Both VSC topologies have been studied mathematically obtaining their models and discretising them, including the LCL filter and taking into account its resonant effects.
- From the models, their dynamics has been analysed getting the perfect control and zero dynamics. This is necessary to judge if the control objectives are feasible or not.
- Furthermore, the power limitations due to the control signal have been found, giving the maximum active and reactive components that the converter can handle from the electrical grid in any direction.

It is important to remark that the controller design is carried out completely in discrete time. That is why the plant to be controlled is discretised, instead of designing a continuous-time controller which will need to be discretised. This is coherent since the control *is* digital and it only sees a discretised version of the real world, and not the real plant in continuous time. However, this is a controversial point due to the existing familiarity and confidence in continuous-time design procedures and tools. The conception of a controller in continuous-time is widely used and the direct design in discrete-time requires a different understanding of the field.

From the practical point of view, a complete experimental plant has been built with all the necessary elements to prove the theoretical results; this was without any doubt, the most challenging and rewarding part. The main contribution is not about the hardware itself, but rather the controller implementation methodology. Once the digital controller is designed and the hardware is ready (i.e., plant tested in open loop and sensors calibrated), the automatic code generation tools carry out the implementation very fast. Therefore, these tools:

- Reduce the global development time.
- Reduce (or eliminate) code errors.

- Can be validated for any domain (like automotive).
- Have the possibility for real-time debug or tuning.

In view of the experimental results, they show the controller robustness facing a wide range of disturbances at either load and grid side (frequency changes, sags, swells, weak grids, high harmonic content, etc.). It is worth mentioning that no active damping methods were used and that all the control is carried out by only measuring two grid currents, two mains voltages and the dc voltage bus.

For all these reasons, this controller ant its fast design methodology are very interesting and could be used in any digital control project, especially in the power electronics industry to develop any kind of active front-end converters, shunt active filters or active power-factor correction devices.

6.3 Future Lines of Research

Several areas of interest could benefit from further research based on this work. One of the most interesting things about the AFC control technique is its usefulness in any system subjected to periodical disturbances. It has been applied successfully to mechanical and electrical systems, but it could also be applied to, for example, thermodynamic systems, active noise control or to reject any kind of vibration.

From the controller perspective, the tuning of resonator gains is a non-convex problem and very difficult to address from an analytical perspective. The HIFOOD numerical method used gives some interesting and valid results, but they are local optimums and very dependent on the initial conditions. More investigation in these kind of methods could give better results, even when the φ_k resonators angles are also parameters to be optimised by the algorithms.

Furthermore, the resonators design could be explored in depth from other perspectives, for example, introducing some specifications in the design giving to the input impedance (or admittance) of the converter an appropriate shape in the frequency domain to contribute to the grid stability.

Also, it would be very interesting to find the relationship between the resonators control loop and a plug-in structure, exactly as in resonant controllers. This could lead to simpler criteria for the system stability analysis. In reality, several techniques with different names (like proportional-resonant or synchronous-frame control[1]) are the same from the mathematical point of view. Therefore, finding the relationship between them could lead to a more general and easier to understand control technique.

[1]Even a particular case of a second order generalised integrator can be seen as a resonator.

Another topic related to he stability of the grid is the constant-power load (CPL) problem. Most of the grid-connected power converters behave as CPL and, since they are increasing in number, they may create stability issues which are difficult to address, but which should be understood in order to prevent or minimise them.

Finally, even if it is not the main topic of this thesis, the automatic code generation is a very powerful tool that saves time in the digital controllers implementation. This procedure is very appealing to the technology industry sector and it would be very interesting to increase their flexibility and efficiency.

A

Modelling Power Converters

A.1 Introduction

There are several techniques that can be used to find the mathematical model of power converters. Many of them are well known techniques, mostly derived from (Middlebrook and Cuk, 1976), and can be applied to a wide range of topologies. Even if they are all equivalent, some of them are more suitable depending on the converter to be modelled.

For instance, regarding the topologies studied in this thesis, two different approaches were applied for the single- and the three-phase three-wire VSC.

A.2 Single-Phase Full-Bridge VSC Modelling

The most intuitive method to model a power converter is to analyse separately every switching state and then, join them by using an auxiliary variable (the control signal). This procedure is ideal if there are few switching states.

As shown in Fig. A.1, there are only two possibilities for the single-phase converter

$$\begin{aligned} L_2\frac{\mathrm{d}i_2}{\mathrm{d}t} &= -v_C - r_2 i_2 + v_g & \qquad L_2\frac{\mathrm{d}i_2}{\mathrm{d}t} &= -v_C - r_2 i_2 + v_g \\ L_1\frac{\mathrm{d}i_1}{\mathrm{d}t} &= v_C - r_1 i_1 - v_{C_0} \quad \text{and} & L_1\frac{\mathrm{d}i_1}{\mathrm{d}t} &= v_C - r_1 i_1 + v_{C_0} \\ C\frac{\mathrm{d}v_C}{\mathrm{d}t} &= i_2 - i_1 & C\frac{\mathrm{d}v_C}{\mathrm{d}t} &= i_2 - i_1 \\ C_0\frac{\mathrm{d}v_{C_0}}{\mathrm{d}t} &= -i_0 + i_1 & C_0\frac{\mathrm{d}v_{C_0}}{\mathrm{d}t} &= -i_0 - i_1, \end{aligned}$$

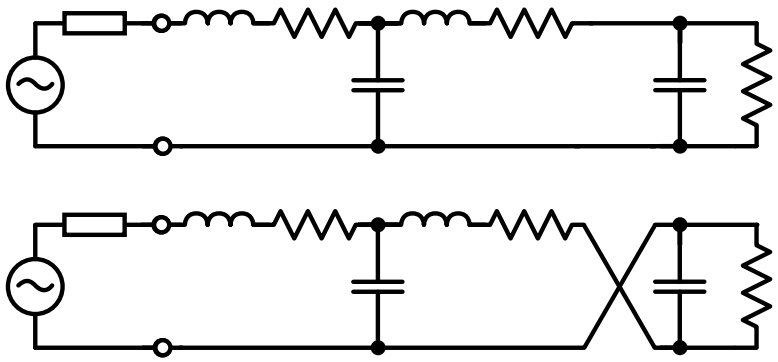

Figure A.1: Possible switching states for the single-phase converter.

It is very easy to show that these two systems can be merged by using the auxiliary control variable $u \in \{-1, 1\}$ to give the non-linear differential equation system 2.1. Under these two assumptions, the equations become linear and make possible its discretization and a direct digital controller design:

- The discrete control variable $u(t)$ switches at a very high frequency with respect to the natural voltage and currents dynamics. If so, the system can be averaged and the control signal can be seen as a continuous-time variable $u(t) \in [-1, 1]$.

- Even if the dc voltage bus v_{C_0} oscillates at twice the mains frequency, its amplitude is small with respect to the average value $\bar{v_{C_0}} = V_{C_0}$. Assuming that this value is simply a constant value V_{C_0}, the differential equation system becomes linear.

A.3 Three-Phase Three-Wire VSC Modelling

In this case, instead of solving every switching state independently, it is easier to replace every switch by dependent current and voltage sources. By doing so, only one analysis is necessary to obtain the differential equations system. For the sake of simplicity and as it is shown in Fig. A.2, only a L input filter is going to be considered, but the result can be easily extrapolated to LCL filters.

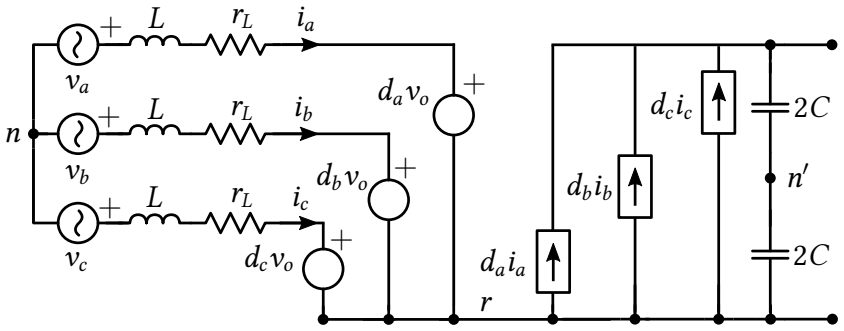

Figure A.2: Equivalent diagram of a three-phase three-wire power converter.

Note that the bus capacitors have been split to show the virtual point n' (each capacitor has a voltage $\frac{v_o}{2}$, so $v_{n'r} = \frac{v_o}{2}$) and that the current flowing to the load is i_o. The differential equations system can be directly written as

$$
\begin{aligned}
L\frac{\mathrm{d}i_a}{\mathrm{d}t} &= -i_a r_L + v_{an} - d_a v_o - v_{rn} \\
L\frac{\mathrm{d}i_b}{\mathrm{d}t} &= -i_b r_L + v_{bn} - d_b v_o - v_{rn} \\
L\frac{\mathrm{d}i_c}{\mathrm{d}t} &= -i_c r_L + v_{cn} - d_c v_o - v_{rn} \\
C\frac{\mathrm{d}v_o}{\mathrm{d}t} &= d_a i_a + d_b i_b + d_c i_c - i_o.
\end{aligned}
$$

These equations are very useful to analyse, for example, what is the relationship with the points n and n'. Adding the currents equations one can write

$$L\left(\frac{\mathrm{d}i_a}{\mathrm{d}t}+\frac{\mathrm{d}i_b}{\mathrm{d}t}+\frac{\mathrm{d}i_b}{\mathrm{d}t}\right)=-(i_a+i_b+i_c)r+(v_{an}+v_{bn}+v_{cn})-(d_a+d_b+d_c)v_o-3v_{rn},$$

supposing balanced voltages and knowing that in a three-wire system the line currents sum zero one obtains finally

$$0=-(d_a+d_b+d_c)v_o-3v_{rn}.$$

The control signals d_a, d_b and d_c belong to the interval $[0,1]$. A simple reparametrization leads to a three new control signals u_a, u_b and u_c belonging to the $[-1,1]$ interval[1].

$$0=-(u_a+u_b+u_c)\frac{v_o}{2}+\frac{3}{2}v_o-3v_{rn}.$$

Therefore, it can be shown that if the three control signals sum zero ($u_a+u_b+u_c=0$), $\frac{v_o}{2}=v_{n'r}=-v_{rn}$, that is, in average, the points n and n' are at the same voltage.

[1]The reparametrization is simply $d_x=\frac{u_x}{2}+\frac{1}{2}$.

B

Code Examples of HIFOOD

B.1 Introduction

In this appendix, two simple examples of how to use de discrete-time version of HIFOO to find a fixed-structure controller in Matlab™ code are presented. In the first case, phases are chosen following the procedure in Chapter 3, being all the gains g_k the elements to be optimized by the algorithm. In the second case, resonator phases φ_k are also left as free parameters to be optimized.

B.2 Tuning Resonator Gains

This is the code for 7 resonators and also for the parallel proportional path. The extended plant structure `Pl` is a MISO system made up of the seven resonators and the plant in series, being the controller a constant vector which represents the resonator (and proportional path) gains to be tuned. Fig. B.1 depicts the extended plant Pl and the controller with all the inputs and outputs.

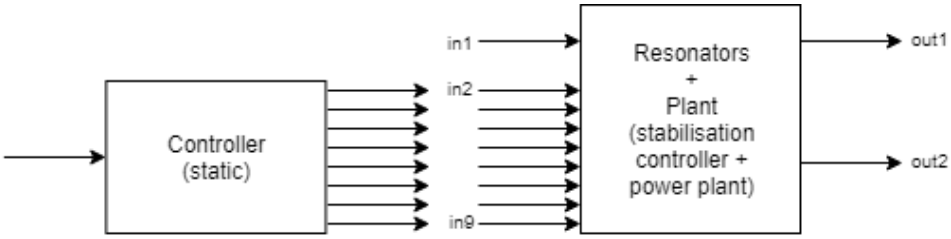

Figure B.1: Extended MISO plant `Pl` and controller.

```
% Pl Plant definition.
% A, B, C, D contains the extended MISO plant where:
%    - res_n represents the nth resonator (with unit gain),
%    - fb1 is the original plant + stabilisation controller.
%    - the proportional phath is added as a unit feedback.
% Finally, the extended plant with an extra (unused) input
% and output is stored in Pl.

[A,B,C,D] = ...
   ssdata(series(parallel(...
                 parallel(...
                 parallel(...
                 parallel(...
                 parallel(...
                 parallel(...
                 parallel(res_1,res_5,[],[],1,1)...
                 ,res_19,[],[],1,1)...
```

```
                  ,res_17,[],[],1,1)...
                  ,res_13,[],[],1,1)...
                  ,res_11,[],[],1,1)...
                  ,res_7,[],[],1,1)...
                  ,1,[],[],1,1),fb1));
Pl = ss(A,[zeros(18,1),B],[zeros(1,18); C],...
        [0,0,0,0,0,0,0,0,0; 0,D],Ts);


% Plant definition of inputs and outputs

Pl.InputGroup.U1  =  1;
Pl.InputGroup.U2  = [2 3 4 5 6 7 8 9];
Pl.OutputGroup.Y1 =  1;
Pl.OutputGroup.Y2 =  2;


% Controller structure

[Ah, Bh, Ch, Dh] = ssdata(ss(0, 0, [0; 0; 0; 0; 0; 0; 0; 0], ...
                                   [1; 1; 1; 1; 1; 1; 1; 0]));
hat = struct('Ahat', Ah, 'Bhat', Bh, 'Chat', Ch, ...
             'Dhat', Dh, 'replicated', false);


% Optimization options

options = struct('cpumax', inf, 'fast', 0, 'prtlevel', 0, ...
                 'structure', hat, 'hinfalg', 'matlab', ...
                 'nrand', 3, 'normtol', 1e-8, ...
                 'evaldist', 1e-8, 'weight', 1, ...
                 'weightNormK', 0, 'augmentHinf', 0, ...
                 'epsilon', 0.0001);


% Initial conditions for the resonators gains

g1  = 0; g5  = 0; g7  = 0; g11 = 0;
g13 = 0; g17 = 0; g19 = 0; gp  = 0;


% Calling the HIFOOD main function

Ctrl = hifood(Pl,1,ss(0, 0, [0; 0; 0; 0; 0; 0; 0; 0], ...
                      [g1; g5; g7; g11; g13; g17; g19; gp]), ...
                      'p', options);
```

HIFOOD has several optimizing options. The parameter `'s'` minimises locally the spectral abscissa ($max(real(eigenvalues))$) of the closed loop plant and the parameter `'p'` minimises locally the pseudo-spectral abscissa of the closed loop plant (for robust stability margin).

```
% Saving the found controller in "d"
[~,~,~,d] = ssdata(Ctrl);
```

B.3 Tuning Resonator Gains and Phases

If the angles φ_k are also free parameters to be tuned, the resonators need to be included into the controller structure to be optimized instead into the plant like in the previous example. This is the code for two resonators and the parallel proportional path. Observe that the controller structure is not a vector of constants any more:

```
[Ah, Bh, Ch, Dh] = ssdata(ss(zeros(3), [1; 1; 0], ...
                             [1 0 0; 0 1 0; 0 0 0], [1; 1; 0]));
```

```
% Initial conditions for the resonators parameters
a1 = 0; a2 = 0; a3 = 0;
b1 = 0; b2 = 0;
c1 = 0; c2 = 0;
```

```
% Calling the HIFOOD algorithm
contr = ss(zeros(3), [b1; b2;  0], [c1 0 0; 0 c2 0; 0 0 0], ...
                     [a1; a2; a3]);
Ctrl  = hifood(Pl, 3, contr, 'p', options);
[~,b,c,d] = ssdata(Ctrl);
```

Note that there are seven parameters to be optimized. This is due to the nonlinear relationship between the transfer function coefficients and the φ_k angles. The expressions which relate the optimized values to the resonators parameters are

```
g1   = a1*sqrt(((b1*c1/a1+cos(w1*Ts))/sin(w1*Ts))^2+1);
phi1 = atan2(b1*c1/a1+cos(w1*Ts),sin(w1*Ts));
g2   = a2*sqrt(((b2*c2/a2+cos(w2*Ts))/sin(w2*Ts))^2+1);
phi2 = atan2(b2*c2/a2+cos(w2*Ts),sin(w2*Ts));
g3   = a3;
```

It is important to highlight that this is only one possibility of many different ways to define this problem.

Bibliography

Acharya, B. and John, V. (2010). Common mode dc bus filter for active front-end converter. *Power India Joint International Conference on Power Electronics, Drives and Energy Systems (PEDES)*, (pp. 1–6).

Apkarian, P. and Noll, D. (2006). Nonsmooth h-infinity synthesis. *IEEE Transactions on Automatic Control*, 51(1), 71–86.

Arzelier, D., Deaconu, G., Gumussoy, S., and Henrion, D. (2011). H2 for HIFOO. *IFAC World Congress on Automatic Control*.

Åström, K., Hagander, P., and Sternby, J. (1984). Zeros of sampled systems. *Automatica*, 20(1), 31–38.

Avago Technologies (2016a). ACPL-790B-000E precision isolation amplifier. Data sheet available online at: https://docs.broadcom.com/docs/pub-005417.

Avago Technologies (2016b). HCPL-316J gate driver octocoupler. Data sheet available online at: https://docs.broadcom.com/docs/AV02-0717EN.

Bayard, D. (2000). A general theory of linear time-invariant adaptive feedforward systems with harmonic regressors. *IEEE Transactions on Automatic Control*, 45(11), 1983–1996.

Blaabjerg, F., Chen, Z., and Kjaer, S. (2004). Power electronics as efficient interface in dispersed power generation systems. *IEEE Transactions on Power Electronics*, 19(5), 1184–1194.

Bodson, M. (2005). Rejection of periodic disturbances of unknown and time-varying frequency. *International Journal of Adaptive Control and Signal Processing*, 19(2-3), 67–88.

Bodson, M., Sacks, A., and Khosla, P. (1992). Harmonic generation in adaptive feedforward cancellation schemes. *IEEE Conference on Decision and Control*, (pp. 1261–1266).

Bodson, M., Sacks, A., and Khosla, P. (1994). Harmonic generation in adaptive feedforward cancellation schemes. *IEEE Transactions on Automatic Control*, 39(9), 1939–1944.

Bollen, M. H. (2000). *Understanding Power Quality Problems: Voltage Sags and Interruptions*, volume 3. IEEE press New York.

Brito, M., Limongi, L., Cavalcanti, M., Neves, F., and Azevedo, G. (2014). A step-dynamic voltage regulator based on cascaded reduced-power series transformers. *Electric Power Systems Research*, 108, 245–253.

Bruinsma, N. and Steinbuch, M. (1990). A fast algorithm to compute the h∞-norm of a transfer function matrix. *Systems & Control Letters*, 14(4), 287–293.

Byl, M. F., Ludwick, S. J., and Trumper, D. L. (2005). A loop shaping perspective for tuning controllers with adaptive feedforward cancellation. *Precision Engineering*, 29(1), 27–40.

Chinchilla, M., Arnalte, S., Burgos, J. C., and Rodríguez, J. (2006). Power limits of grid-connected modern wind energy systems. *Renewable energy*, 31(9), 1455–1470.

Costa, R., Griñó, R., and Fossas-Colet, E. (2004). Odd-harmonic digital repetitive control of a single-phase current active filter. *IEEE Transactions on Power Electronics*, 19(4), 1060–1068.

Costa-Castelló, R., Griñó, R., Cardoner, R., and Fossas, E. (2009). High-performance control of a single-phase shunt active filter. *IEEE Trans on Ctrl. Syst. Tech.*, 17(6), 1318–1329.

Costa-Castelló, R., Nebot, J., and Griñó, R. (2005). Demonstration of the internal model principle by digital repetitive control of an educational laboratory plant. *IEEE Transactions on Education*, 48(1), 73–80.

Dahono, P. (2002). A control method to damp oscillation in the input LC filter. *IEEE Power Elect. Specialists Conf.*, 4, 1630–1635.

Dannehl, J., Fuchs, F., Hansen, S., and Thø gersen, P. (2010). Investigation of active damping approaches for PI-based current control of grid-connected pulse width modulation converters with LCL filters. *Industry Applications, IEEE Transactions on*, 46(4), 1509–1517.

Enslin, J. (2004). Interconnection of distributed power to the distribution network. *IEEE Power Systems Conference and Exposition*, (pp. 726–731).

Enslin, J. and Heskes, P. (2004). Harmonic interaction between a large number of distributed power inverters and the distribution network. *IEEE Transactions on Power Electronics*, 19(6), 1586–1593.

E.ON (April, 2008). *Requirements for Offshore Grid Connections in the E.ON Netz Network*.

Escobar, G., Hernández-Gómez, M., Martínez, P. R., and Martínez-Montejano, M. F. (2007). A Repetitive-Based Controller for a Power Factor Precompensator. *IEEE Transactions on Circuits and Systems*, 54(9), 1968–1976.

Escobar, G. and Valdez, A. A. (2007). Repetitive-Based Controller for a UPS Inverter to Compensate Unbalance and Harmonic Distortion. *IEEE Transactions on Industrial Electronics*, 54(1), 504–510.

Francis, B. A. and Wonham, W. M. (1976). The internal model principle of control theory. *Automatica*, 12(5), 457–465.

Freijedo, F. D., Yepes, A. G., Member, S., López, O., Fernández-comesa na, P., and Doval-gandoy, J. (2011). An Optimized Implementation of Phase Locked Loops for Grid Applications. *IEEE Transactions on Instrumentation and Measurement*, 60(9), 3110–3119.

Garcia, D., Karimi, A., and Longchamp, R. (2007). Robust proportional integral derivative controller tuning with specifications on the infinity-norm of sensitivity functions. *IET Control Theory & Applications*, 1(1), 263–272.

Golestan, S., Ramezani, M., Guerrero, J., Freijedo, F., and Monfared, M. (2014). Moving average filter based phase-locked loops: Performance analysis and design guidelines. *IEEE Transactions on Power Electronics*, 29(6), 2750–2763.

Griñó, R., Cardoner, R., Costa-Castelló, R., and Fossas, E. (2007). Digital repetitive control of a three-phase four-wire shunt active filter. *IEEE Transactions on Industrial Electronics*, 54(3), 1495–1503.

Gumussoy, S., Henrion, D., Millstone, M., and Overton, M. L. (2009). Multiobjective Robust Control with HIFOO 2.0. *IFAC Proceedings Volumes*, 42(6), 144–149.

Hillerström, G. and Walgama, K. (1996). Repetitive control theory and applications. a survey. *Proceedings of the 13th IFAC World Congress*.

Information Technology Industry Council (2000). ITI (CBEMA) curve.

Kempf, C., Messner, W., Tomizuka, M., and Horowitz, R. (1993). Comparison of four discrete-time repetitive control algorithms. *IEEE Control Systems Magazine*, 13(6), 48–54.

Lee, H. S. (1997). Implementation of adaptive feedforward cancellation algorithms for pre-embossed rigid magnetic (PERM) disks. *IEEE Transactions on Magnetics*, 33(3), 2419–2423.

LEM (2016). LA-100-P current transducer. Data sheet available online at: http://www.lem.com/docs/products/la_100-p_e_.pdf.

Liserre, M., Blaabjerg, F., and Hansen, S. (2005). Design and control of an LCL-filter-based three-phase active rectifier. *IEEE Transactions on Industrial Applications*, 41(5), 1281–1291.

Liserre, M., Teodorescu, R., and Blaabjerg, F. (2006). Stability of photovoltaic and wind turbine grid-connected inverters for a large set of grid impedance values. *IEEE Transactions on Power Electronics*, 21(1), 263–272.

Malo, S. and Griñó, R. (2007). Diseño de un controlador para el rechazo selectivo de armónicos de tensión en un inversor CC-CA. *Actas del Seminario Anual de Automática, Electrónica Industrial e Instrumentación*, (pp. 49–53).

Malo, S. and Griñó, R. (2008). Adaptive feed-forward cancellation control of a full-bridge dc-ac voltage inverter. *Proc. of the 17th IFAC World Congress*, (pp. 4571–4576).

Manayathara, T. J., Tsao, T.-C., and Bentsman, J. (1996). Rejection of unknown periodic load disturbances in continuous steel casting process using learning repetitive control approach. *IEEE Transactions on Control Systems Technology*, 4(3), 259–265.

Messner, W. and Bodson, M. (2007). Design of adaptive feedforward algorithms using internal model equivalence. *International Journal of Adaptive Control and Signal Processing*, 9(2), 199–212.

Middlebrook, R. and Cuk, S. (1976). A general unified approach to modelling switching-converter power stages. *IEEE Power Electronics Specialists Conference*, (pp. 18–34).

Ministerio de Industria de España (2006). *Requisitos de respuesta frente a huecos de tensión de las instalaciones eólicas*. Technical report.

Orellana, M. and Griñó, R. (2012). On the Stability of Discrete-Time Active Damping Methods for VSI Converters with a LCL Input Filter. *38th IEEE Industrial Electronics Conference (IECON)*, (pp. 2378–2383).

Orellana, M. and Griñó, R. (2013). Some considerations about discrete-time AFC controllers. *IEEE 52nd Annual Conference on Decision and Control (CDC)*, (pp. 6904–6909).

Proakis, J. G. and Manolakis, D. G. (1988). *Introduction to digital signal processing*. Prentice Hall Professional Technical Reference.

Rech, C., Grundling, H., and Pinheiro, J. (2000). Comparison of discrete control techniques for UPS applications. *IEEE Industry Applications Conference*, 4, 2531–2537.

Routimo, M. and Tuusa, H. (2007). LCL type supply filter for active power filter-comparison of an active and a passive method for resonance damping. *IEEE Power Electronics Specialists Conference (PESC)*, (pp. 2939–2945).

Teodorescu, R., Blaabjerg, F., Liserre, M., and Dell'Aquila, A. (2003). A stable three-phase LCL-filter based active rectifier without damping. *38th Industry Applications Conference (IAS) Annual Meeting*, 3, 1552–1557.

Teodorescu, R., Blaabjerg, F., Liserre, M., and Loh, P. (2006). Proportional-resonant controllers and filters for grid-connected voltage-source converters. *IEEE Proc. Electric Power Applications*, 153(5), 750–762.

Teodorescu, R., Liserre, M., and Rodriguez, P. (2011). *Grid converters for photovoltaic and wind power systems*, volume 29. John Wiley & Sons.

Texas Instruments (2008). C28x FPU fastRTS library v1.0 (literature number sprc664). Available online at: http://www-s.ti.com/sc/techlit/sprc664.zip.

Texas Instruments (2010). TMS320F28335 controlCARD information files. Available online at: http://www.ti.com/lit/zip/sprr102.

Texas Instruments (2016). TMS320F28335 digital signal processor. Data sheet available online at: http://www.ti.com/lit/gpn/tms320f28335.

Twining, E. and Holmes, D. (2003). Grid current regulation of a three-phase voltage source inverter with an lcl input filter. *IEEE Transactions on Power Electronics*, 18(3), 888–895.

Wang, T., Ye, Z., Sinha, G., and Yuan, X. (2003). Output filter design for a grid-interconnected three-phase inverter. *IEEE 34th Power Electronics Specialist Conference*, 2, 779–784 vol.2.

Ward, D. J. (2001). Power quality and the security of electricity supply. *Proceedings of the IEEE*, 89(12), 1830–1836.

Wessels, C., Dannehl, J., and Fuchs, F. (2008). Active damping of LCL-filter resonance based on virtual resistor for PWM rectifiers - stability analysis with different filter parameters. *IEEE Power Electronics Specialists Conference (PESC)*, (pp. 3532–3538).

White, D. and Woodson, H. (1959). *Electromechanical Energy Conversion*. John Wiley and Sons, Inc.

Wu, E. and Lehn, P. (2005). Digital current control of a voltage source converter with active damping of LCL resonance. *Applied Power Electronics Conference and Exposition, 2005. APEC 2005. Twentieth Annual IEEE*, 3(5), 1642–1649.

Wu, X., Panda, S., and Xu, J. (2010). Design of a plug-in repetitive control scheme for eliminating supply-side current harmonics of three-phase PWM boost rectifiers under generalized supply voltage conditions. *IEEE Transactions on Power Electronics*, 25(7), 1800–1810.

Yang, Y., Zhou, K., and Cheng, M. (2013). Phase compensation resonant controller for pwm converters. *IEEE Transactions on Industrial Informatics*, 9(2), 957–964.

Yepes, A. G., Freijedo, F. D., Doval-Gandoy, J., López, O., Malvar, J., and Fernandez-Comesana, P. (2010). Effects of discretization methods on the performance of resonant controllers. *IEEE Transactions on Power Electronics*, 25(7), 1692–1712.

Yepes, A. G., Freijedo, F. D., Lopez, O., and Doval-Gandoy, J. (2011a). Analysis and design of resonant current controllers for voltage-source converters by means of nyquist diagrams and sensitivity function. *IEEE Transactions on Industrial Electronics*, 58(11), 5231–5250.

Yepes, A. G., Freijedo, F. D., López, O., and Doval-Gandoy, J. (2011b). High-performance digital resonant controllers implemented with two integrators. *IEEE Transactions on Power Electronics*, 26(2), 563–576.

Yepes, A. G., Vidal, A., López, O., and Doval-Gandoy, J. (2014). Evaluation of techniques for cross-coupling decoupling between orthogonal axes in double synchronous reference frame current control. *IEEE Transactions on Industrial Electronics*, 61(7), 3527–3531.

Zhang, X. (2003). *Parameter-Dependent Lyapunov Functions and Stability Analysis of Linear Parameter-Dependent Dynamical Systems*. PhD thesis, Georgia Institute of Technology.

Zhou, K. and Wang, D. (2001). Digital repetitive learning controller for three-phase CVCF PWM inverter. *IEEE Transactions on Industrial Electronics*, 48(4), 820–830.

Zhou, K. and Wang, D. (2003). Digital repetitive controlled three-phase PWM rectifier. *IEEE Transactions on Industrial Electronics*, 18(1), 309–316.

Zmood, D. (2003). Stationary frame current regulation of PWM inverters with zero steady-state error. *Transactions on IEEE Power Electronics*, 18(3), 814–822.